Magnetic Resonance based Electrical Properties Tomography (EPT) Using Multi-channel Transmission for Imaging Human Brain and Animal Cancer Models

A DISSERTATION
SUBMITTED TO THE FACULTY OF THE
UNIVERSITY OF MINNESOTA
BY

Yicun Wang

IN PARTIAL FULFILLMENT OF THE REQUIERMENTS
FOR THE DEGREE OF
DOCTOR OF PHILOSOPHY

Advisor: Bin He
Co-advisor: Pierre-Francois Van de Moortele

May, 2018

Acknowledgments

I am deeply indebted to my advisor, Prof. Bin He. Without his guidance and support throughout my Ph.D., none of this dissertation work could have been possible. His vision and enthusiasm, as well as his critical thinking and high standard for research have left profound impacts on me and my future career. I feel extraordinarily fortunate to be trained by him.

I would like to extend my sincere gratitude to my co-advisor, Prof. Pierre-François Van de Moortele, for his patience and tremendous help. His comprehensive training to me and his invaluable feedbacks to my work are essential to the accomplishment of my dissertation. I appreciate all of it from the bottom of my heart.

I gratefully acknowledge my committee members, Prof. Michael Garwood and Prof. Mehmet Akçakaya, for their inspiring discussions and constructive feedbacks to my research. This dissertation has become more complete thanks to their input.

I thank Dr. Jiaen Liu and Dr. Xiaotong Zhang for their help especially at the beginning of my dissertation projects. To me, they were great teachers and colleagues in the lab, and fantastic older brothers and friends after work. I miss the days when they were around in Minnesota. I wish them all the best in their future careers.

I appreciate Dr. Qi Shao for his hard work on handling tumor models in the animal project. His help was a great relief to my workload so I could concentrate more on the other important aspects of the project. I am also grateful to our collaborators, Profs. John Bischof, Emilian Racila, Gregor Adriany and Michael Nelson for their input to various parts of this work.

I gratefully appreciate the generous support from the Center for Magnetic Resonance Research (CMRR) at the University of Minnesota. I acknowledge Profs. Kamil Ugurbil, Wei Chen, Patrick Bolan, Greg Metzger, Xiaoping Wu for their advice, as well as CMRR staff Andrea Grant, John Strupp, Lance DelaBarre, and Russell Lagore for their help.

I acknowledge the BME DGS Prof. Victor Barocas, graduate advisor Rachel Jorgenson and other BME staff. It has been great to be a member of the BME family.

Special thanks to my colleges and friends for their useful discussions and accompany: Kai Yu, Long Yu, Ting Yang, Chris Cline, Clara Zhang, Abbas Sohrabpour, Brad Edelman, Steve Meng, Haiteng Jiang, and others from Dr. He's lab; Jinjin Zhang, Sean Moen, Emily Ma, Byeong-Yeul Lee and others from CMRR.

Finally, my deepest thanks go to my family, especially to my parents and my lover Jiaoyue Liu for their unconditional love and support. This dissertation is dedicated to them.

Abstract

Electrical properties (EPs) of biological tissues are determined by tissue constituents, and therefore may provide novel biomarkers for characterization of diseased tissues such as cancer. In addition, accurate quantification of tissue EPs is essential for understanding the biological effects of electromagnetic field involved in MRI exams and neuromodulation. Magnetic Resonance based Electrical Properties Tomography (EPT) is a technology that noninvasively maps EPs at radiofrequency (RF) by fitting magnetic field measurements (B_1 maps) acquired with MRI to Maxwell's equations. However, current application of EPT is critically limited by assumptions made about B_1 phase, tissue homogeneity and symmetry of RF coil.

The overarching goal of this dissertation is to develop novel MREPT technologies at 7 T to robustly retrieve accurate EP values using a plurality of transmit B_1 measurements without those strong assumptions. These technologies are based on inverse problems integrating a priori information and image sparsity, with targeted applications being *in vivo* imaging of human brain and rodent tumor models.

First of all, a seed selection strategy for state-of-the-art multi-channel gradient based EPT (gEPT) method is proposed which achieves full automation of the EP reconstruction process. Brain imaging results from twelve healthy human subjects are reported using the proposed method. To drop the requirement for receive B_1, the "CONtrast Conformed Electrical Properties Tomography" (CONCEPT) technology for human brain imaging is proposed based on a partial differential equation with joint L_1 and L_2 norm regularization. The central large-scale inverse problem is solved efficiently using

Alternating Direction Method of Multipliers (ADMM) developed in-house. Results from electromagnetic simulations and a phantom experiment demonstrate improved accuracy and robustness of CONCEPT compared to existing techniques. For animal model imaging, the "Boundary Informed Electrical Properties Tomography" (BIEPT) technology is designed based on a constrained inverse problem that exploits EP boundary condition and image sparsity. The imaging platform and BIEPT reconstruction method are evaluated using simulations, phantom experiments and a large cohort of rodent cancer models. The reconstructed EPs of tumor are compared to multiple conventional MR contrasts as well as histopathology slides, demonstrating their potential value for cancer diagnosis and staging.

Table of Contents

List of Tables

List of Figures

List of Abbreviations

ADC	Apparent Diffusion Coefficient
ADMM	Alternating Direction Method of Multipliers
AFI	Actual Flip-angle Imaging
BIEPT	Boundary Informed Electrical Properties Tomography
BSS	Bloch-Siegert Shift
CONCEPT	CONtrast Conformed Electrical Properties Tomography
CP	Circularly polarized
CSF	Cerebrospinal fluid
DCE-MRI	Dynamic Contrast Enhancement Magnetic Resonance Imaging
EIT	Electrical Impedance Tomography
EM	Electromagnetic
EPT	Electrical Properties Tomography
EPs	Electrical properties
FA	Flip angle
FDTD	Finite-difference time-domain
FID	Free induction decay
FOV	Field of view
gEPT	Gradient-based Electrical Properties Tomography
GLCM	Grey-level co-occurrence matrix
GM	Gray matter
GRE	Gradient echo
H&E	Hematoxylin and Eosin
IACUC	Institutional Animal Care and Use Committee
IRB	Institutional Review Board
ISMRM	International Society for Magnetic Resonance in Medicine
MAT-MI	Magneto-Acoustic Tomography with Magnetic Induction
MPRAGE	Magnetization Prepared Rapid Acquisition Gradient Echo

MREIT	Magnetic Resonance Electrical Impedance Tomography
MRI	Magnetic Resonance Imaging
PDE	Partial differential equation
pTx	Parallel transmission
PVP	Polyvinylpyrrolidone
RF	Radiofrequency
ROI	Region of interest
SAR	Specific absorption rate
SNR	Signal-to-noise ratio
SSFP	Steady state free precession
Std	Standard deviation
STE	Stimulated echo
T1-w	T1-weighted
T2-w	T2-weighted
TE	Echo time
TGV	Total generalized variation
TNF	Tumor necrosis factor
TPA	Trnasceive phase assumption
TR	Repetition time
TSE	Turbo Spin Echo
TV	Total variation
UHF	Ultra-high Field
WM	White matter

Chapter 1 - Introduction

Electrical properties (EPs), comprised of electrical conductivity σ and permittivity ε, are intrinsic properties quantifying a tissue's ability to conduct, dissipate, and deposit electrical energy. As the operating frequency of the applied electrical field varies, different components of the multi-scale tissue structure resonate, depicted by a characteristic curve as a function of frequency. EPs in the lower frequency band (<1 MHz) reflect tissue macroscopic structures, such as extracellular volume, cellularity, and cellular membrane integrity, while those in the microwave band (~1-100 GHz) correspond to the microscopic level such as overall ion concentration, water and macromolecule content, etc. In between is the radiofrequency (RF) band, in which EPs are influenced by mixed effects of the above factors (Schwan and Foster, 1980). EPs can potentially be used for diagnostic purposes such as cancer and stroke. They are also critical parameters in electromagnetic simulations to understand the interaction of human body with electromagnetic fields, for heating safety considerations in MRI scans via estimation of local specific absorption rate (SAR), and for improved outcome in neuromodulation methods such as deep brain stimulation (DBS) and transcranial magnetic stimulation (TMS).

Several non-invasive imaging modalities have been proposed to study tissue EPs across a wide spectrum, such as electrical impedance tomography (EIT) (Metherall et al., 1996), magnetic resonance electrical impedance tomography (MREIT) (Woo and Seo,

2008), magneto-acoustic tomography with magnetic induction (MAT-MI) (Xu and He, 2005), and microwave imaging (Fear et al., 2002). Nevertheless, it remains highly challenging to retrieve quantitative EP maps at high spatial resolution, due to the limited signal to noise ratio (SNR) of electromagnetic measurement in biological environments, as well as the ill-posed nature of image reconstruction problems derived from Maxwell's equations.

Alternatively, EPs can be derived from high spatial resolution RF magnetic field (B_1 field) measurements obtained with MRI (Haacke et al., 1991; Zhang et al., 2014a; Katscher and van den Berg, 2017; Liu et al., 2017b). This technique, dubbed magnetic resonance-based electrical properties tomography (MREPT or EPT), represents a promising modality for quantitative EP mapping as it substantially reduces the severity of ill-posedness faced by the previous modalities. The feasibility of MREPT was initially demonstrated using birdcage RF coils with a single transmit channel (Wen, 2003; Katscher et al., 2009). With assumptions of equality of the RF transmit and receive phase distributions (known as transceive phase assumption or TPA), as well as local homogeneity of tissue EPs, it has been shown that conductivity and permittivity distributions can be calculated by a pixel-wise fitting to the curvature of B_1 field. Despite the simplicity of this EPT approach, several of its limitations by nature thwart its further development and application. First of all, the TPA breaks down at ultra-high-field (UHF) MRI systems, due to the pronounced electromagnetic wave behavior at an elevated operating frequency (Van de Moortele et al., 2005; Van Lier et al., 2014). Violation of TPA induces error in the estimation of RF phase which propagates to EPs, especially on

the periphery of the imaged object. As a result, single-transmit EPT does not benefit from the improved SNR at UHF, and it is not suitable for accurate local SAR estimation which is an important safety constraint and a critical application of EPs at UHF (Collins et al., 1998, 2004). On the other hand, a single B_1 measurement is not sufficient to robustly characterize the transition area of tissue EPs unless further strong assumptions are made about the imaged object and the experimental setup. Erroneous oscillation on the tissue transition area induced by this suboptimal modeling degrades the image quality and hampers proper interpretation of the quantitative results.

Multi-channel RF coil arrays can potentially be used to address the aforementioned limitations of single channel EPT at UHF (Zhang et al., 2013b; Sodickson et al., 2013; Liu et al., 2015). A multi-channel RF coil array consists of several transmit elements that can be controlled independently. This type of RF coils are ubiquitous at UHF because the phase and amplitude of RF pulse played by each transmit element can be carefully designed, through static B_1 shimming or parallel transmission (pTx), so that a desirable B_1 pattern can be achieved that homogeneously excites a region of interest of arbitrary shape with high RF efficiency (Katscher et al., 2003; Van de Moortele et al., 2007). For the purpose of EPT reconstruction, different B_1 maps acquired from such coil elements correspond to the same underlying EP distribution of the imaged object. Therefore, they can be concatenated to further decrease the condition number of the inverse problem, or to accommodate additional variables modeling the spatial variation of tissue EPs.

Nevertheless, a generic multichannel based EPT method has not yet been achieved, mainly because of two hurdles. Firstly, a subjective choice of seed points needs to be

made, which may bias the reconstruction results (Liu et al., 2017a, 2015). The EPs of the chosen seeds are assigned based on *ex vivo* measurement results which do not necessarily coincide with *in vivo* values, considering the different physiology especially blood infiltration. Secondly, both transmit B_1 and receive B_1 are required for measurement, which prolongs scan time (Liu et al., 2015; Zhang et al., 2013a, 2013b). Receive B_1 maps are weighted by proton density which is nontrivial to be eliminated. Current practice estimates proton density based on assumption of left-right symmetry of both RF coil structure and imaged object, which limits EPT to imaging of healthy, well-positioned human brain using transceiver coil arrays.

The overarching goal of this dissertation is to develop novel EPT methods based on only multiple transmit B_1 maps without subjective assignment of seed points. Such methods can be used with RF coils with a high-count receive element array which can, in turn, offer substantial gains in SNR. They also hold potentials to image unsymmetrical body organs and diseased brain.

This dissertation is outlined as follows:

Chapter 2 provides a brief review of the background knowledge associated with MREPT. This chapter can be divided into two parts. The first part is on electrical properties in general, including its definition, biomedical implications and *in vivo* imaging methods. The second part is dedicated to MREPT technology, consisting of B_1 mapping in MRI, EP reconstruction algorithms and their emerging biomedical applications. Portions of this chapter have been published in a co-authored paper in *IEEE Transactions on Biomedical Engineering* (Liu et al., 2017b).

Chapter 3 presents an automated seed selection method for gradient-based electrical properties tomography and *in vivo* imaging results of the human brain. This work has been accepted for presentation at the 26th annual meeting of ISMRM (Wang et al., 2018).

Chapter 4 describes CONtrast Conformed Electrical Properties Tomography (CONCEPT) for human brain imaging. This work has been presented at the 25th annual meeting of ISMRM (Wang et al., 2017), and has been submitted for publication in *IEEE Transactions on Medical Imaging*.

Chapter 5 presents Boundary Informed Electrical Properties Tomography (BIEPT) and its *in vivo* imaging results of small animal tumor models. This study has been submitted for publication in *Magnetic Resonance in Medicine*.

Chapter 6 summarized the key theoretical developments and scientific findings of this dissertation. An outlook is also provided for future research on EPT using multiple RF transmissions.

Chapter 2 - Background

2.1 Electrical Properties of Biological Tissues

2.1.1 Definition

Biological tissues have both conductive and dielectric properties. An applied electric field $\vec{E}$ causes the free ions in the tissue to move, causing conduction current density $\vec{J}$; In the meanwhile, the electric field polarizes the macro-molecules of the tissue to create electric dipole moments, or displacement current density $\vec{D}$. For tissue in a radio-frequency (RF) time-harmonic electromagnetic field where the electric anisotropy is negligible, Ampere's law reads:

$$\nabla \times \vec{H} = j\omega\vec{D} + \vec{J} = j\omega\varepsilon\vec{E} + \sigma\vec{E} = j\omega(\varepsilon_r\varepsilon_0 - j\frac{\sigma}{\omega})\vec{E} \tag{2.1}$$

where $\vec{H}$ is spatial magnetic field intensity, ω is the operating angular frequency, $\varepsilon_0 = 8.854 \times 10^{-12}\ F/m$ is the permittivity of free space, ε_r is relative permittivity and σ is conductivity. The electrical properties of biological tissues are defined as a complex number ε_c:

$$\varepsilon_c = \varepsilon_r\varepsilon_0 - j\frac{\sigma}{\omega} \tag{2.2}$$

The electrical properties of tissue are determined by the interaction of electromagnetic field with its constituents at the cellular and molecular level, thus they are functions of the RF wavelength (or operating frequency) and closely related to local physiological conditions. For example, the relative permittivity of adipose tissue is on the

level of 10^6 at 100 Hz while goes down to only 20 at 300 MHz. It is notable that at 300 MHz, the relative permittivity of malignant breast tumor is around 60, due to its higher water content compared to its neighboring adipose tissue. In addition, a significant elevation of conductivity value from 0.12 S/m to 0.82 S/m has been reported in cancerous breast tissue at 300 MHz (Joines et al., 1994), which potentially results from increase of ion concentration due to cellular inflammation or necrosis.

2.1.2 Applications in Biomedical Research and Clinical Practice

The electrical properties of biological tissue are determined by its constituents, thus closely related to local physiological and pathological conditions. This unique characteristic lends *in vivo* electrical properties mapping modalities great potential in both biomedical research and clinical practice. Amongst all the applications of tissue EPs, quantitative modelling of the brain and diagnosis of breast cancer have shown most promising results, and will be introduced as follows.

Neurological diseases, such as epilepsy and Parkinson's disease, severely compromise the life quality and life expectance of the patients. Numerous studies have shown that symptoms of these diseases could be mitigated dramatically by properly delivering electrical or magnetic stimulations to modulate the neural activity. Successful cases have been reported using Deep Brain Stimulation (DBS) (Perlmutter and Mink, 2006) and Transcranial Magnetic Stimulation (TMS) (Corthout et al., 2001). However, failing to precisely control the exerted electromagnetic stimulation may lead to degradation of therapeutic effects and other severe side effects. Precision

neuromodulation requires subject-specific 3D electrical properties distributions in physical units, i.e. Siemens/meter for conductivity and Faraday/meter for permittivity, which could be provided by quantitative brain EP mapping techniques. Such brain models could also be used to improve the performance of many other techniques, such as Brain-Computer Interface (BCI) and electroencephalography (EEG) source localization (He et al., 2018).

Breast cancer is the most common and the second most lethal cancer among females in the US ("CDC - Cancer Among Women," 2017). X-ray Mammography is currently the daily screening modality for breast cancer, in which the breasts of the patient are pulled away from the body, compressed firmly between two glass plates, and two projection views (top and side) are taken. The compression is uncomfortable, and causes normal dense tissues to lump and resemble tumors on the image, leading to unnecessary invasive biopsy and avoidable patient anxiety (Fass, 2008; Karellas and Vedantham, 2008). On the other hand, this 2D projection based technique is insensitive to tumors hidden deep in the breast, and it is difficult to determine the size and position of the tumor. As an ionized radiation based technique, it is also unsuitable for therapy evaluation which requires repeated scans. In contrast, EP imaging of the breast at RF does not involve ionized radiation, and it is a tomographic technique such that the hidden tumor can be clearly imaged. The EP contrast between tumor and normal breast tissues varies by frequency, but a difference can be observed across a wide spectrum from 100 MHz to 20 GHz (Lazebnik et al., 2007; Sha et al., 2002). For example, it has been reported that the contrast in electrical properties between malignant tumor and its surrounding adipose

tissue is 233% and 577% for permittivity and conductivity at 300 MHz, respectively (Joines et al., 1994), which lends EP mapping techniques great potentials to identify tumorous tissues with high sensitivity and specificity.

2.2 *In Vivo* Electrical Properties Imaging Technologies

Maxwell's equations dictate that propagation and steady state distribution of electromagnetic (EM) wave are dependent on both EM source and medium. It is possible to retrieve the electromagnetic properties of the medium at various frequencies given measurements of the EM distributions at corresponding frequencies.

A number of efforts have been made towards minimally invasive and accurate EP mapping *in vivo*. Electrical impedance tomography (EIT) injects low frequency current through and detects voltage from electrodes mounted on the sample, providing EP distributions with low spatial resolution due to limited number of electrodes and the inversion of an ill-conditioned matrix (Metherall et al., 1996). Microwave imaging retrieves EPs in a similar way based on the scattering matrix from an antenna array (Fear et al., 2002). Magnetic resonance electrical impedance tomography (MREIT) detects the induced magnetic field change due to a probing current by measuring the phase drift of processing protons in a MRI scanner (Woo and Seo, 2008). This technique is able to provide spatial resolution on the scale of MRI images, yet safety concerns would arise in pursuit of higher SNR. Magneto-acoustic tomography with magnetic induction (MATMI) is a noninvasive imaging modality with high spatial resolution, based on indirect measurement of electrical field via ultrasound waves generated by Lorentz force (Xu and

He, 2005). Magnetic Resonance based Electrical Properties Tomography (MREPT) is a recently introduced technique that is promising to provide high-resolution EP distributions *in vivo* by solving Maxwell's equations involving RF magnetic field perturbation. No additional hardware or procedure to existing MRI technique is required for this technique, rendering it applicable to clinical applications in a short period of time.

2.3 Magnetic Resonance Imaging and B_1 Mapping

Magnetic Resonance Imaging (MRI) is a non-invasive imaging modality that employs magnetic spins inside an organism, mainly water protons, to provide tomographic images. The resonance, interaction and motion of magnetic spins are susceptible to their ambient environment as well as a rich variety of physiological and pathological effects in the body, giving MRI versatility in characterizing tissue structures and functions. In the context of precision medicine, MRI is capable of accurately quantifying bio-physical and bio-chemical parameters, such as magnetic relaxation, magnetic susceptibility, flow velocity, diffusion coefficient, chemical content, etc. MRI is also a safe biomedical imaging platform which does not involve ionized radiation or hazardous intervention to bodily functions, making it suitable for repetitive examinations. Because of these unique merits, MRI has been playing an indispensable role in both medical care and biomedical research since the 1980s.

In MRI, a strong static magnetic field (B_0) is utilized to produce a magnetization in the imaged object. This magnetization is detectable after excitation with an electromagnetic field at the proton resonance frequency, or Larmor frequency, of the

interested isochromat. Larmor frequency is proportional to B_0, and falls into RF range (128 MHz at 3 Tesla and 298 MHz at 7 Tesla for water protons). The transmit sensitivity, or B_1^+ field, is defined by

$$B_1^+ := \mu_0 \frac{H_x + iH_y}{2} \tag{2.3}$$

where $\mu_0 = 4\pi \times 10^{-7}\ H/m$ is the magnetic constant, and H is time-harmonic magnetic field strength established by a RF coil. By definition, B_1^+ is the clockwise polarization of the H field in the transverse (xy) plane. Its counterpart, B_1^-, is defined as

$$B_1^- := \mu_0 \frac{(H_x - iH_y)^*}{2} \tag{2.4}$$

which determines the spatial receive sensitivity of the RF coil to the magnetization (Hoult, 2000).

Due to electromagnetic wave behavior at RF, B_1^+ and B_1^- are spatially heterogeneous, especially at high and ultra-high fields where the Larmor frequency is higher and the corresponding RF wavelength is shorter. Measurement of B_1^+ and B_1^- are important topics in MRI for the quality assurance of RF coils and calibration of quantitative MRI. In addition, in the context of multi-transmission MRI system, pilot B_1^+ maps are acquired to be used in B_1^+ shimming or parallel transmission (pTx) for the purpose of achieving a homogenous excitation across the region of interest (ROI) (Katscher et al., 2003; Van de Moortele et al., 2007). On the other hand, B_1^- maps from a high-count RF receive element array can be employed for spatial encoding for imaging acceleration (Pruessmann et al., 1999; Griswold et al., 2002).

Since accurate B_1^+ mapping is a prerequisite for the multi-transmission based EPT reconstruction, it is introduced in more details as follows. The central process for B_1^+ mapping, or simply B_1 mapping, is to manipulate the spin system of interest to acquire two or more MRI images in carefully designed regime and parameters, so that the shared confounding factors affecting MRI signals can be eliminated by post-processing. These factors include T1, T2, proton density and B_0 heterogeneity. B_1 mapping is usually done by imaging the flip angle (FA) of the magnetization, since the latter is proportional to the time integral of RF pulse and directly determines MR signal amplitude.

A conventional approach for B_1 mapping is the double angle method (DAM), in which two images are acquired with two nominal FAs α_1 and $\alpha_2 = 2\alpha_1$, and their ratio ideally results in $\cos\alpha_1$ (Insko and Bolinger, 1993). This method is simple and straightforward, yet a long scan time is needed for full relaxation of the spin system. Its variant, saturated DAM (SDAM), utilizes RF pulse preparation and spiral readout that significantly accelerate the imaging process, at the cost of high SAR (Cunningham et al., 2006).

In contrast, another popular method, Actual Flip-angle Imaging (AFI), employs identical RF pulses but varies the repetition time (TR) in a Gradient Echo (GRE) sequence (Yarnykh, 2007). The flip angle map can be retrieved from the ratio of the two signals through a nonlinear relationship. AFI is time-efficient and insensitive to tissue properties, but its accuracy is compromised for both small FA ($< 10^\circ$) and large FA ($> 70^\circ$).

Other B_1 mapping technologies involve more intricate MR physics to disentangle flip angle from tissue-related contrasts. Two examples are Bloch-Siegert Shift (BSS) (Sacolick et al., 2010; Duan et al., 2013; Weingärtner et al., 2016) and Dual Refocusing Echo Acquisition Mode (DREAM) (Nehrke and Börnert, 2012). Bloch-Siegert shift is the effect that the resonance frequency of a nucleus shifts when an off-resonance RF field is applied. It has been shown that the phase difference between two signals resulted from two RF pulses of a specific profile with frequency shifted by $\pm\omega_{RF}$ is dependent on the quadratic of peak B_1. As a method based on signal phase detection, B_1 mapping by Bloch-Siegert shift is insensitive to tissue contrasts affecting signal magnitude, i.e. proton density, T1, T2 and T2*. It also shows robustness against susceptibility and chemical shift effects. DREAM, on the other hand, employs multiple on-resonance RF pulses to produce stimulated echoes. The flip angle is calculated from the ratio of the stimulated echo (STE) and the free induction decay (FID). It is a very fast B_1 mapping technique with whole brain coverage in a few seconds, and its dependence on susceptibility, chemical shift effects, T1 and T2 are relatively weak.

The four B_1 mapping methods introduced above, SDAM, AFI, BSS and DREAM, were implemented in the human brain and compared to electromagnetic simulation in a study by Brink et al. (Brink et al., 2014). In this study, the authors report that the residual structure of the ventricles in the measured B_1 maps is not entirely measurement bias due to MR-related mechanisms, but also raised from the strong contrast in electrical conductivity between cerebrospinal fluid and its surrounding white matter. This study

sheds light on the idea of detecting tissue electrical properties using B_1 maps, the foundation of Magnetic Resonance based Electrical Properties Tomography.

2.4 Magnetic Resonance based Electrical Properties Tomography

Magnetic Resonance based Electrical Properties Tomography (MREPT or EPT) is a non-invasive approach to retrieve tissue electrical conductivity and permittivity by fitting the measured radiofrequency magnetic field (B_1 field) to time-harmonic Maxwell's equations (Haacke et al., 1991; Wen, 2003; Katscher et al., 2009; Zhang et al., 2010). The reconstructed electrical properties provide fundamentally differential information compared to MR relaxometry, holding promise for additional sensitivity and specificity in clinical diagnoses, such as cancer identification and characterization (Shin et al., 2015; Tha et al., 2018). Recent studies also shed light on the associations of EPs with other valuable biomarkers, such as sodium concentration, protein, and water content, that are more challenging for direct quantification (Liao et al., 2015; Mandija et al., 2017). In addition, subject-specific EP distribution is an essential ingredient for realistic local SAR estimation, especially for ultra-high-field ($\geq$ 7 T) applications where electromagnetic wave behavior becomes prominent (Vaughan et al., 2001; Zhang et al., 2013b). Improvements in the reliability of local SAR estimation would in return unleash the full power of ultra-high-field MRI that is otherwise limited by conservative safety constraints.

The bandwidth of RF pulse is typically several kilohertz, which is a small fraction of the central frequency (several hundred megahertz). In addition, EPs of biological tissue are approximately constant across this narrow band. Therefore, the excitatory RF field

can be treated as a time-harmonic field. Concatenating Ampere's Law and Faraday's Law of Maxwell's equations (Wen, 2003) yields:

$$-\nabla^2\vec{H} = \omega^2\mu\varepsilon_c\vec{H} + \nabla\varepsilon_c \times \frac{\nabla \times \vec{H}}{\varepsilon_c} \tag{2.5}$$

μ is the magnetic permeability, which varies by only several parts per million (ppm) with respect to the vacuum permeability μ_0, thus it is assumed that $\mu = \mu_0$ in the imaging area. According to Equ. 2.5, electrical properties ε_c could be reconstructed given that the time-harmonic magnetic field $\vec{H}$ has been accurately measured.

2.4.1 Local EPT Methods

Conventional MREPT approaches assume that electrical properties are locally homogeneous. With transmit (B_1^+) and receive (B_1^-) field corresponding to the positively and negatively polarized components that can be detected directly from MRI signal, we have the Helmholtz equation:

$$\varepsilon_c \approx -\frac{\nabla^2 B_1^+}{\omega^2\mu_0\, B_1^+} \approx -\frac{\nabla^2 B_1^{-*}}{\omega^2\mu_0\, B_1^{-*}} \tag{2.6}$$

Based on the local homogeneity assumption, Haacke et al. first studied a layered model in the early 1990s (Haacke et al., 1991). Wen explicitly derived Equ. 2.6 and made an important observation that the phase of transmit RF field approximately equals to half of the phase of a spin-echo image acquired with a quadrature volume coil (Wen, 2003). This observation is known as "transceiver phase approximation" (TPA), which turns out to be central in the conventional EPT methods. With these two assumptions, Wen successfully images EP contrast in both phantoms and biological tissues. Following these

two pilot studies, systematic research of Helmholtz-based single-channel EPT started from 2009 (Katscher et al., 2009; Voigt et al., 2011). Recently, efforts have been made to address boundary artifacts coming from the Helmholtz equation using structure-informed regularization (Ropella and Noll, 2016), and to improve phase estimation using multiple receive elements (Shin et al., 2015).

TPA is a valid assumption at low B_0 fields due to good symmetry of B_1^+ and B_1^-. However, at ultra-high fields where the wavelength of the RF pulse is close to the size of the imaging object, the phase distribution varies rapidly and TPA introduces significant errors (Van Lier et al., 2012). Therefore, several studies have been performed to avoid the TPA and to reconstruct the absolute phase distribution together with EPs using a multi-channel RF coil array (Sodickson et al., 2012; Zhang et al., 2013a; Liu et al., 2013).

Conventional EPT techniques suffer from severe artifacts on the boundary of tissue where the local homogeneity assumption is no longer valid. Zhang et al. take EPs and their gradient terms as independent unknowns which are simultaneously retrieved using dual excitations of linear-polarization modes in a quadrature coil, demonstrating improved boundary fidelity (Zhang et al., 2010). However, this algorithm is based on the Cartesian components of the RF magnetic field that are not directly measurable from MRI. Later, the concept is extended to MR-measurable B_1^+ and receive B_1^- fields, which are related using Gauss's Law for Magnetism (Zhang et al., 2013b). Improved reconstruction results are obtained in comparison with the Helmhotlz-based methods, yet the spatial EP gradient information is discarded, which contains valuable information.

2.4.2 Global EPT Methods

Global EPT approaches attempt to alleviate the boundary artifact by incorporating spatial EP variation term into reconstruction. Convection-reaction EPT (cr-EPT) and its conductivity-only variant take the reciprocal of EPs as unknowns to linearize the reconstruction problem, from which 2D slices of EPs can be reconstructed in a single iteration (Hafalir et al., 2014; Gurler and Ider, 2017). Nevertheless, the empirical assumptions made about B_1 magnitude and phase, as well as EPs of the imaged target itself may introduce reconstruction errors.

Another category of EP mapping technologies is built upon forward modeling and electromagnetic simulations. In Contrast Source Inversion (CSI), the incident field of an empty coil is simulated, and the contrast source distribution is iteratively updated to minimize the discrepancies between the scattering field and the observed field (Balidemaj et al., 2015a). A similar idea can be implemented in spatial frequency space which retrieves EPs without iterations (Schmidt and Webb, 2016). In addition, Global Maxwell Tomography (GMT) performs a full-wave simulation with a current guess of EP distribution, which gets updated iteratively to match the measured field (Serralles et al., 2016). These simulation-based algorithms utilize the integral form of Maxwell's equations that naturally incorporates spatial variation of EPs. However, highly accurate electromagnetic simulations need to be performed and carefully registered to experimentally acquired data in order to preserve the delicate EP contrast, which is challenging for implementation in realistic scenarios. To the best of our knowledge, there has been no experimental validation of these approaches.

2.4.3 A Hybrid Method: Multi-channel Gradient-based EPT (gEPT)

Using a multi-channel transceiver coil array, Liu et al. explicitly calculate the EP gradient locally and perform spatial integration globally from a user-assigned seed point to retrieve EP distributions (Liu et al., 2015). By defining EP gradients related to the transmit and receive RF fields $g^+ = \frac{\partial ln\varepsilon_c}{\partial x} + i\frac{\partial ln\varepsilon_c}{\partial y}, g^- = \frac{\partial ln\varepsilon_c}{\partial x} - i\frac{\partial ln\varepsilon_c}{\partial y}$, the master equation can be written as:

$$\begin{aligned} \nabla^2 B_1^+ &= -\omega^2\mu_0 B_1^+\varepsilon_c + \nabla B_1^+ \cdot [g^+, -ig^+, g_z] \\ \nabla^2 B_1^{-*} &= -\omega^2\mu_0 B_1^{-*}\varepsilon_c + \nabla B_1^{-*} \cdot [g^-, -ig^-, g_z] \end{aligned} \tag{2.7}$$

which are solved at each pixel. Derivation of Equ. 2.7 and its corresponding pixel-wise inverse problems are described in details in Chapter 3.

Note that $|B_1^-|$ is not directly measurable from MRI – it is weighted by the proton density ρ of the imaged target. An assumption of left-right symmetry in RF coil structure as well as the imaged object is made, so that

$$\rho \approx \rho_{est} = \frac{\sum_J \left|\rho B_{1,j}^-(-x,y)\right|}{\sum_K \left|B_{1,k}^+(x,y)\right|} \tag{2.8}$$

where k denotes the transmit channels and j the receive channels. ρ_{est} is then used to cancel out the proton density weighting in each receive channel.

gEPT achieves excellent characterization of tissue transition area in simulations and *in vivo* experiments. However, it is limited to imaging of symmetric, healthy human brain using a specially designed transceiver coil array. Furthermore, a subjective choice of seed points as ground truth may bias the reconstructed EPs.

2.5 Biomedical Applications of MREPT

2.5.1 Cancer Diagnosis, Staging and Grading

Tumorigenesis is accompanied by significant local changes at molecular, cellular and tissue levels. For example, sodium concentration and water content are elevated due to aggressive proliferation; nucleus takes a much larger volume of the cell body and cytoplasm becomes much denser; cellular density substantially increases with extracellular matrix impaired to facilitate cancer invasion. These abnormalities also develop as tumor grows into different stages. EPs, as fundamental physical properties of biological tissues, correlate with the tumor features and represent responsible and responsive indicators for cancer diagnosis, staging, and grading.

It is noteworthy that a huge variation of tissue EPs exists across the body, such that contrast between normal and cancerous tissue is dependent not only on tumor itself but also the properties of its surrounding tissues (Joines et al., 1994). This heterogeneity of contrast plays a fundamental role when determining the sensitivity and specificity of EPT to pinpoint cancer in different organs.

Utilizing different implementations of the polynomial fitting method of turbo spin echo or fast spin echo phase maps, several pilot studies have demonstrated significant conductivity elevation in malignant lesions compared to normal breast tissues and benign cysts (Katscher et al., 2013, 2012a; Shin et al., 2015). A retrospective study involving 65 female patients with invasive breast cancer further revealed the correlation between reconstructed conductivity and prognostic information such as tumor type and status

(Kim et al., 2016). The clinical applicability of EPT is still pending establishment, potentially through large-scale prospective studies including various subtypes, sizes, and stages of breast lesions.

EPT can also be applied to examine other organs for cancer characterization. In the pelvis, feasibility of conductivity measurement in cervix tumor has been demonstrated in 20 patients (Balidemaj et al., 2016, 2015b). In the brain, conductivity of glioma has been reported to deviate from surrounding healthy tissue (van Lier et al., 2011; Voigt et al., 2011b). This deviation varies with tumor type and positively correlates with tumor grade, which is important reference information for therapy design, and is reported to be consistent with probe measurements of excised specimen (Tha et al., 2015, 2014).

Recently, tumor-bearing rodent models have been used in several EPT studies. Animal models have unique advantages of better availability and flexibility, opening possibility for more thorough, well-controlled investigations to correlate EPs with cancer pathological features. An animal tumor study in the field utilized combined B_1 magnitude and transceiver phase from a quadrature coil at 3 T (Bulumulla et al., 2014). Both conductivity and permittivity of implanted adenocarcinoma on three rats are reported to be consistent with probe measurements. In another study, Liu et al. successfully demonstrated the conductivity difference between implanted tumor and the surrounding muscle with high sensitivity (Liu et al., 2017a). This study utilizes a dedicated 8-channel microstrip transceiver array coil developed for 7 T MRI and the gradient-based EPT reconstruction algorithm (Liu et al., 2015). Future studies are expected to take on animal

models bearing more resemblance to human cancer and to monitor tumor development along time course.

2.5.2 Other Diagnostic Applications

A case study of an ischemic stroke patient at 7 T reported that conductivity in the infarction is elevated by a factor of more than two (van Lier et al., 2012). Another study involves two cases of hemorrhagic and ischemic strokes patients in subacute stage (Gurler et al., 2016), using a more recent phase-only EPT reconstruction algorithm that alleviates tissue boundary artifacts (Gurler and Ider, 2017). They report increased conductivity in ischemic lesions and edema, but not hematoma itself, hypothetically due to formation of blood clot.

Taking *a prior* knowledge from quantitative magnetic susceptibility maps for EPT reconstruction, another study investigates conductivity of deep brain nuclei (Katscher et al., 2016). The reconstructed conductivity and susceptibility are reported to be uncorrelated, suggesting that EPs can provide an additional dimension of information about these important brain structures.

For body imaging, the major challenges fall into the experimental part to obtain reliable B_1 magnitude and phase distributions that are minimally affected by confounding factors, such as B_0 inhomogeneity and motion artifacts. Most previous studies assumed homogeneity of B_1 magnitude in a relatively small ROI and applied phase only conductivity imaging to various organs in the body. Steady state free precession (SSFP)

sequence is favorable in these applications due to its insensitivity to B_0 effects and fast speed.

Except for the cervix tumor imaging discussed above, there are three more instances where EPT has been utilized to retrieve the conductivity of different body organs, showing the broad spectrum of the potential applications: (1) The liver of 10 healthy subjects is examined using SSFP during inspiration and expiration, leading to conductivity measurements that are consistent with published values (Stehning et al., 2012). (2) Two isolated perfused pig heart models, one of which with induced severe ischemia, are scanned using gated SSFP, reporting conductivity values of normal tissue close to previous literature and roughly 60% decrease in infarcted area (Voigt et al., 2012b). (3) Five healthy volunteers are recruited for a lung scan, and the expected conductivity difference between inspiration hold and expiration hold is observed (Katscher and Bornert, 2016). An Ultrashort-TE (UTE) sequence is used in this study so as to address the fast signal decay in the lung due to short T2 and severe B_0 inhomogeneity.

2.5.3 Subject-specific Estimation of Local Specific Absorption Rate

Specific Absorption Rate (SAR) is the rate at which heat is absorbed by human body due to RF electromagnetic field radiation during MRI exams. Whole-body global SAR is defined as

$$Global\ SAR = \frac{1}{V}\int \frac{\sigma|\vec{E}|^2}{2\rho_m} d\vec{r}$$

where V is volume, σ is conductivity and ρ_m is mass density. When examing small masses of tissue, the spatial distribution of SAR becomes increasingly heterogeneous at ultra-high-field MRI, due to the pronounced wave behavior of electromagnetic field operating at higher frequency, creating local hot spots in the body that present as a major safety concern. Therefore, it is important to evaluate local SAR in addition to global SAR to ensure safety of subjects

$$Local\ SAR = \frac{\sigma|\vec{E}|^2}{2\rho_m}$$

Current international guideline (IEC 60601-2-33:2010) imposes maximum SAR values for both global SAR and local SAR (over mass of 10g), over time periods of 6-minute and 10-second.

Locations and amplitudes of these hot spots are dependent on the RF coil design, RF power delivered to the coil as well as the body EPs. Current practice of SAR estimation is implemented through electromagnetic feld simulation involving the RF coil and standard numerical human body models, such as the virtual family models (Christ et al., 2010). During MRI scans, a conservative cap is imposed to the maximum RF power to be delivered based on the simulation result.

For the numerical model used in the simulation, EPs are assigned to different tissues based on *ex vivo* measurement results using invasive probes (C. Gabriel et al., 1996; S Gabriel et al., 1996). However, organs are intrinsically heterogeneous in composition and structure; their EPs also vary with age (Peyman et al., 2001, 2007) and short-term biological effects such as blood supply (Semenov et al., 2017). A recent study of *in vivo* conductivity imaging of muscle in 20 cervical cancer patients reports a 14% systematic

deviation from the tabulated EP values and significant inter-subject variability (Balidemaj et al., 2016). In addition, discrepancies between subject anatomy and the standard body model, positioning of the body with respect to the RF coil, and RF loading effects may further increase the unreliablility of SAR estimation. Therefore, it is desirable to image the subject body EPs *in vivo* using EPT for improved accuracy in subject-specic local SAR estimation.

EPT-based local SAR determination using quadrature excitation was first studied at 1.5 T with a phantom (Katscher et al., 2009) and later in human subjects (Voigt et al., 2012a). The concept was extended to non-quadrature multi-transmit coil array at 3 T (Katscher et al., 2012b; Buchenau et al., 2013) by quantitatively estimating absolute transmit B_1 phase using MR-measurable multi-channel B_1 data instead of relying on the TPA. The theory was further generalized to inhomogeneous Helmholtz equation, deriving absolute transmit and receive phases of each coil element by Gauss's Law and the extracted proton density (Zhang et al., 2013b). It has been repeatedly shown that after determination of electric fields of the single transmit array elements, the prediction of local SAR for arbitrary B_1-shim settings is possible (Buchenau et al., 2013; Zhang et al., 2014b).

Chapter 3 - Automated Seeds Selection for Gradient-based EPT and Its *In Vivo* Validation

3.1 Introduction

Gradient-based EPT (gEPT) is a recently proposed technology that utilizes both transmit B_1 and receive B_1 maps measured from a multi-channel RF transceiver array to retrieve tissue EPs. gEPT preserves correct EP contrast on tissue boundaries by explicitly reconstructing the spatial variation or "gradient" of tissue EPs, followed by its integration from a user-assigned seed point (Liu et al., 2015). The EPs of the seed point are assigned according to *ex vivo* measurement of biological tissues from Gabriel et al. 1996 (S. Gabriel et al., 1996). However, systematic reconstruction bias exists owing to the subjective choice of seed points (Fig. 3.1), presenting a critical challenge to its repeatability and clinical applications. Additionally, there is a potential discrepancy between *ex vivo* measured EPs assigned to the seed point and their actual values *in vivo* due to blood filtration and oxygen levels (Semenov et al., 2017), which introduces a global bias to the reconstructed EPs.

In this chapter, we propose a method to automatically select multiple distributed seed points for gEPT. EP values of these seed points are calculated from B_1 maps measured *in vivo* instead of referring to the tabulated EP values acquired *ex vivo*. Imaging results from twelve healthy human subjects are presented and analyzed using statistical methods.

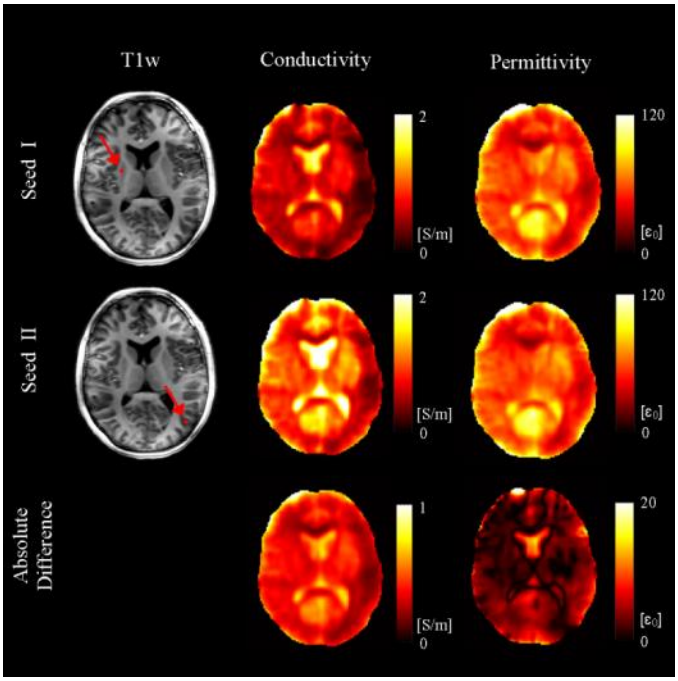

Figure 3.1 Discrepancies in gEPT reconstruction results due to different choices of seed point. Location of the seed point is labeled using a red dot pointed by red arrow on T1 weighted (T1w) image. Seed I locates in the Globus Pallidus and seed II locates in the cortex. EP values of gray matter at 298 MHz (σ = 0.69 S/m and ε_r = 60.1ε_0) were assigned in both cases. Significant difference in EPs can be observed from these two cases, which is also spatially dependent.

3.2 Theory

In this section, starting from Maxwell's equations, a pixel-wise inverse problem is derived that links multiple relative B_1 distributions to EP gradient. The theory is developed from previous works (Zhang et al., 2013b; Sodickson et al., 2013; Liu et al., 2015), and the matrix form of the pixel-wise inverse problem is presented here for the first time.

Consider time-harmonic electromagnetic field at angular frequency ω in Cartesian coordinate system. By combining Ampère's law and Faraday's law to eliminate the electric field, we have

$$\nabla^2\vec{B} = -\omega^2\mu_0\varepsilon_c\vec{B} - \nabla\varepsilon_c \times \frac{\nabla \times \vec{B}}{\varepsilon_c} \tag{3.1}$$

assuming that magnetic susceptibility $\mu \approx \mu_0$ in biological tissues. Equ. 3.1 is a vector formula about $\vec{B} = (B_x, B_y, B_z)$ in phasor terms, and it is equivalent to the following equation systems:

$$\begin{aligned}
\nabla^2 B_x &= -\omega^2\mu_0\varepsilon_c B_x - \left(\frac{\partial B_y}{\partial x} - \frac{\partial B_x}{\partial y}\right)\frac{\partial ln\varepsilon_c}{\partial y} + \left(\frac{\partial B_x}{\partial z} - \frac{\partial B_z}{\partial x}\right)\frac{\partial ln\varepsilon_c}{\partial z} \\
\nabla^2 B_y &= -\omega^2\mu_0\varepsilon_c B_y + \left(\frac{\partial B_y}{\partial x} - \frac{\partial B_x}{\partial y}\right)\frac{\partial ln\varepsilon_c}{\partial x} - \left(\frac{\partial B_z}{\partial y} - \frac{\partial B_y}{\partial z}\right)\frac{\partial ln\varepsilon_c}{\partial z} \\
\nabla^2 B_z &= -\omega^2\mu_0\varepsilon_c B_z - \left(\frac{\partial B_x}{\partial z} - \frac{\partial B_z}{\partial x}\right)\frac{\partial ln\varepsilon_c}{\partial x} + \left(\frac{\partial B_z}{\partial y} - \frac{\partial B_y}{\partial z}\right)\frac{\partial ln\varepsilon_c}{\partial y}
\end{aligned} \tag{3.2}$$

$\vec{B}$ is not directly measurable by MRI, but it is possible to measure its positively polarized component in the rotating frame $B_1^+ = (B_x + iB_y)/2$ (Hoult, 2000). Using linear combination, Equ. 3.2 is transformed to

$$\nabla^2 B_1^+ = -\omega^2\mu_0\varepsilon_c B_1^+ + \frac{i}{2}\left(\frac{\partial B_y}{\partial x} - \frac{\partial B_x}{\partial y}\right)g_+ + \left(\frac{\partial B_1^+}{\partial z} - \frac{1}{2}\frac{\partial B_z}{\partial x} - \frac{i}{2}\frac{\partial B_z}{\partial y}\right)g_z \tag{3.3}$$

where $g_+ := \frac{\partial ln\varepsilon_c}{\partial x} + i\frac{\partial ln\varepsilon_c}{\partial y}, g_z := \frac{\partial ln\varepsilon_c}{\partial z}$. Utilizing Gauss' Law for Magnetism, we have

$$\frac{i}{2}\left(\frac{\partial B_y}{\partial x} - \frac{\partial B_x}{\partial y}\right) = \left(\frac{\partial B_1^+}{\partial x} - i\frac{\partial B_1^+}{\partial y} - \frac{1}{2}\left(\frac{\partial B_x}{\partial x} + \frac{\partial B_y}{\partial y}\right)\right) = \frac{\partial B_1^+}{\partial x} - i\frac{\partial B_1^+}{\partial y} + \frac{1}{2}\frac{\partial B_z}{\partial z} \tag{3.4}$$

For an MRI coil comprised of long striplines, B_z is negligible in the middle part of the coil elements compared to the transverse components (Liu et al., 2015). Taking this into consideration, the following equation can be derived based on B_1^+ field

$$\nabla^2 B_1^+ \approx -\omega^2 \mu_0 \varepsilon_c B_1^+ + \left(\frac{\partial B_1^+}{\partial x} - i\frac{\partial B_1^+}{\partial y}\right) g_+ + \frac{\partial B_1^+}{\partial z} g_z \tag{3.5}$$

This equation holds for any transmit field B_{1p}^+ from a single coil element indexed by p. However, the absolute phase of B_{1p}^+, i.e. absolute transmit phase, is intractable, since the phase of MRI signal has mixed contributions from transmit field, receive field, chemical shift, magnetic susceptibility, eddy current effects, etc. Taking the phase difference between two transmit channels p and r, the common terms can be eliminated, resulting in a relative transmit phase distribution φ_{pr}^+. The relationship between absolute and relative B_1^+ can be expressed as

$$B_{1p}^+ = \left|B_{1p}^+\right| e^{i\varphi_p^+} = \left|B_{1p}^+\right| e^{i(\varphi_{pr}^+ + \varphi_r^+)} = B_{1pr}^+ e^{i\varphi_r^+} \tag{3.6}$$

B_{1pr}^+ is measurable, whereas φ_r^+ is the unknown absolute transmit phase of the reference channel r. Combining Equ. 3.5 with Equ. 3.6, we have

$$\begin{aligned} & e^{i\varphi_r^+}\nabla^2 B_{1pr}^+ + 2\nabla e^{i\varphi_r^+} \cdot \nabla B_{1pr}^+ + B_{1pr}^+ \nabla^2 e^{i\varphi_r^+} \\ & \quad = -\omega^2 \mu_0 \varepsilon_c B_{1pr}^+ e^{i\varphi_r^+} \\ & \quad + \left(e^{i\varphi_r^+}\frac{\partial B_{1pr}^+}{\partial x} + B_{1pr}^+ \frac{\partial e^{i\varphi_r^+}}{\partial x} - ie^{i\varphi_r^+}\frac{\partial B_{1pr}^+}{\partial y} - iB_{1pr}^+ \frac{\partial e^{i\varphi_r^+}}{\partial y}\right) g_+ \\ & \quad + \left(e^{i\varphi_r^+}\frac{\partial B_{1pr}^+}{\partial z} + B_{1pr}^+ \frac{\partial e^{i\varphi_r^+}}{\partial z}\right) g_z \end{aligned} \tag{3.7}$$

Cancelling out $e^{i\varphi_r^+}$ from both sides of the equation

$$\nabla^2 B_{1pr}^+ + 2i\nabla B_{1pr}^+ \cdot \nabla\varphi_r^+ + B_{1pr}^+(i\nabla^2\varphi_r^+ - \|\nabla\varphi_r^+\|^2)$$
$$= -\omega^2\mu_0\varepsilon_c B_{1pr}^+$$
$$+\left(\frac{\partial B_{1pr}^+}{\partial x} - i\frac{\partial B_{1pr}^+}{\partial y} + iB_{1pr}^+\frac{\partial\varphi_r^+}{\partial x} + B_{1pr}^+\frac{\partial\varphi_r^+}{\partial y}\right)g_w \quad (3.8)$$
$$+\left(\frac{\partial B_{1pr}^+}{\partial z} + iB_{1pr}^+\frac{\partial\varphi_r^+}{\partial z}\right)g_z$$

For each spatial location, we have the following matrix form

$$\left[B_{1pr}^+, \nabla B_{1pr}^+\right]$$
$$\cdot\begin{bmatrix} \omega^2\mu_0\varepsilon_c + i\nabla^2\varphi_r^+ - \|\nabla\varphi_r^+\|^2 - i\left(\frac{\partial\varphi_r^+}{\partial x} - i\frac{\partial\varphi_r^+}{\partial y}\right)g_+ - i\frac{\partial\varphi_r^+}{\partial z}g_z \\ 2i\frac{\partial\varphi_r^+}{\partial x} - g_+ \\ 2i\frac{\partial\varphi_r^+}{\partial y} + ig_+ \\ 2i\frac{\partial\varphi_r^+}{\partial z} - g_z \end{bmatrix} = -\nabla^2 B_{1pr}^+ \quad (3.9)$$

Concatenating all n transmit channels that share the same set of unknown φ_r^+ and ε_c-related variables, we have a linear system of equations $Ax = b$ for each image pixel containing 4 unknowns and n equations. Despite its formulation as an inverse problem, one important distinction of Equ. 3.9 from conventional inverse problem is that A matrix is not deterministic, but rather calculated from B_{1pr}^+ measurement. This linear system of equations is solved in a sense of least-squares, which gives

$$g_+ = real(g_+) + i\cdot imag(g_+) = -real\left(2i\frac{\partial\varphi_r^+}{\partial x} - g_+\right) - i\cdot real\left(2i\frac{\partial\varphi_r^+}{\partial y} + ig_+\right)$$

A similar derivation can be conducted for $B_1^{-*} = (B_x - iB_y)/2$, yielding $g_- \coloneqq \frac{\partial ln\varepsilon_c}{\partial x} - i\frac{\partial ln\varepsilon_c}{\partial y}$. Combing g_+ and g_- yields $\frac{\partial ln\varepsilon_c}{\partial x}$ and $\frac{\partial ln\varepsilon_c}{\partial y}$, which can be used for 2D integration given a few seed points with known EP values.

3.3 Methods

3.3.1 Experiment

All human experiment procedures were approved by the University of Minnesota Institutional Review Board (IRB) in accordance with federally approved guidelines.

Twelve human subjects were recruited for a brain scan using Siemens 7 T MRI using a 16-channel microstrip coil array (Adriany et al., 2008). Relative complex B_1^+ from each channel was acquired by a series of gradient echo (GRE) in small-flip-angle regime, with calibration using actual flip-angle imaging (AFI) of all channels transmitting in a static B_1^+ shim setting (Van de Moortele et al., 2007; Yarnykh, 2007). Proton density weighted relative complex B_1^- was acquired using a long TR (TR = 8 s) GRE. Both B_1 maps were acquired as axial slices in a resolution of 1.5 × 1.5 × 3.0 mm^3.

T1-weighted images were acquired by taking the ratio of image sets from a 3D magnetization prepared rapid acquisition gradient echo (3D-MPRAGE) sequence (TI = 1.5 s, TR = 3.5 s, TE = 2.26 ms, flip angle = 6°) and a 3D small-flip angle gradient echo (GRE) sequence (TR = 327 ms, TE = 2.26 ms, flip angle = 4°) in resolution of 1.5 × 1.5 × 3.0 mm^3. Taking the ratio of images cancels out undesirable weightings such as transmit and receive B_1 profile, T2*, and proton density (Van de Moortele et al., 2009).

3.3.2 Image Reconstruction

Proton density weighting ρ in the measured B_1^- was estimated and removed using $\rho \approx \frac{\sum_j \left|\rho B_{1,j}^-\right|}{\sum_k |B_{1,k}^+|}$, where k and j denote transmit and receive channels, respectively. Relative B_1^+ and B_1^- were smoothed using a $5 \times 5 \times 3$ Gaussian low-pass filter with standard deviation of $1.2 \times 1.2 \times 0.8$, and their spatial gradient and Laplacian were taken with $5 \times 5 \times 3$ Savitzky-Golay (SG) filters. Relative B_1^+ from all 16 channels were concatenated to produce a linear equation system based on Equ. 3.9, which was solved pixel by pixel to yield absolute B_1^+ phase gradient $\frac{\partial \varphi^+}{\partial x}$ and $\frac{\partial \varphi^+}{\partial y}$, as well as $g_+ = \frac{\partial ln\varepsilon_c}{\partial x} + i\frac{\partial ln\varepsilon_c}{\partial y}$, as described in the Theory section. Similarly, relative B_1^- from all 16 channels were concatenated to yield $\frac{\partial \varphi^-}{\partial x}$, $\frac{\partial \varphi^-}{\partial y}$, and $g_- = \frac{\partial ln\varepsilon_c}{\partial x} - i\frac{\partial ln\varepsilon_c}{\partial y}$. Local EP values were calculated by Helmholtz equation assuming piece-wise homogeneity $\varepsilon_{c,local} = \frac{-\nabla^2 B_1^+}{\omega^2 \mu_0 B_1^+}$ with measured $|B_1^+|$ and calculated $\frac{\partial \varphi^+}{\partial x}$ and $\frac{\partial \varphi^+}{\partial y}$ in the previous step. Brain voxels with local EP values falling in the range of $0 \le \sigma \le 3\ \mathrm{S/m}$ and $0 \le \varepsilon \le 100\varepsilon_0$ were sorted in ascending order based on the spatial gradient strength of local conductivity. The top N voxels with the smallest local conductivity gradient magnitude were chosen as seed points, since they are expected to be less effected by the large oscillations near tissue boundaries. EPs calculated from the Helmholtz equation were assigned to these seeds. All seeds were weighted equally during the integration of the EP gradient.

3.4 Results

Local conductivity calculated by the Helmholtz equation and its gradient strength are shown in Fig. 3.2. From the local conductivity map, one can identify cerebral-spinal fluid in cerebral ventricles by its high conductivity values compared to other brain compartments, yet severe boundary artifacts hamper a clear separation of gray matter and white matter. On the other hand, the local conductivity gradient successfully detects tissue boundaries which can be used for further selection of seed points.

Fig. 3.3 shows reconstructed EPs using 2, 10, 20, 50, 100 and 500 seeds. Both conductivity and permittivity deviate significantly from the tabulated values when the number of seeds is smaller than 20. The reconstruction results stabilize when more than 20 seeds were chosen, and the stability remains up to as large as 500 seeds. This feature is also observed in the box plots of aggregated results across all subjects (Fig. 3.4). Inter-subject variation is considerably large when a small number of seeds were chosen, but it decreases as the seed number increases. Paired t-test shows no statistically significance between the results using 50 and 100 seeds for both conductivity and permittivity of all three brain compartments.

Fig. 3.4 also shows that the reconstructed EPs converge to values that are not equal to the tabulated *ex vivo* results. Quantitative results using 100 seeds are presented in Table 3.1. We observe that permittivity retrieved by EPT is closer to *ex vivo* probed numbers, with < 15% difference in all three brain compartments. However, significant discrepancies are found in conductivity values obtained using these two methods, with *in*

vivo values being higher in gray matter and white matter, and lower in cerebral-spinal fluid.

In Fig. 3.5, reconstructed EPs in each brain compartment of each subject are plotted using box plots, from which one can observe considerable intra-subject variation as well.

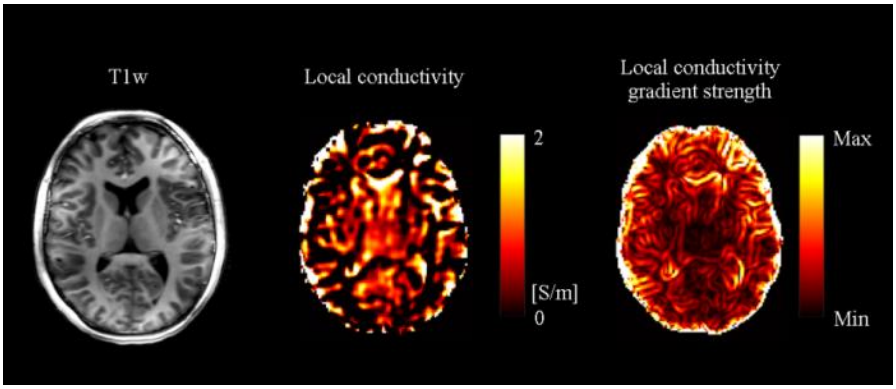

Figure 3.2 T1w image, calculated local conductivity distribution and its gradient strength.

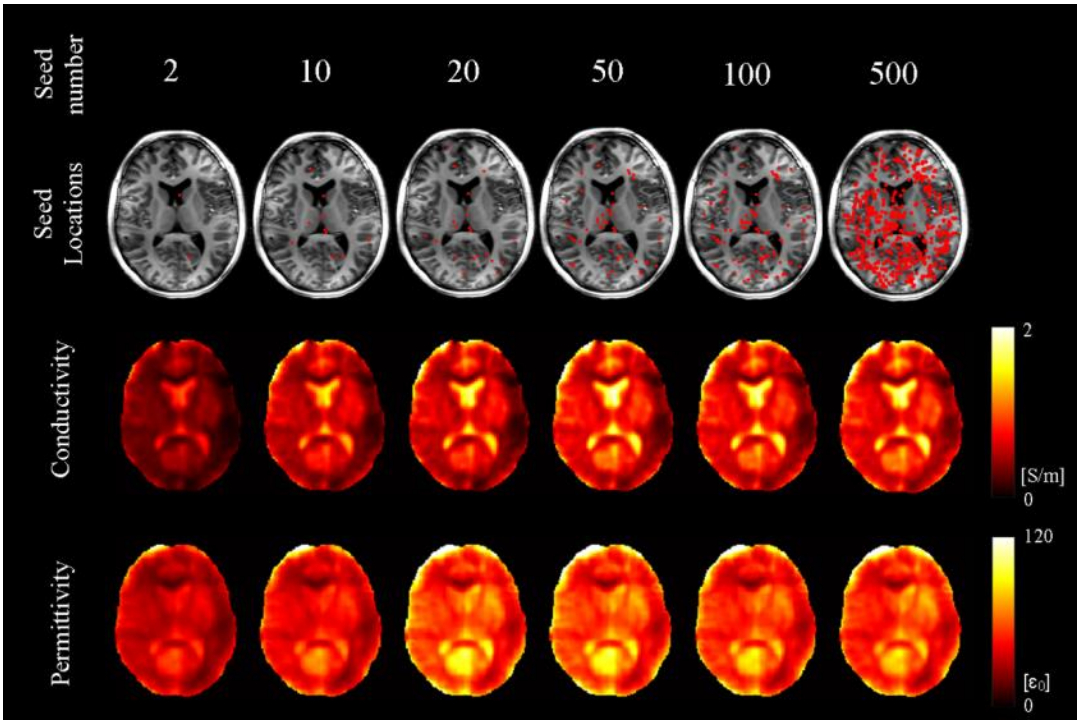

Figure 3.3 Reconstructed conductivity and permittivity using EP gradient and different numbers of automatically selected seeds. The reconstruction results become stable for seed number >20.

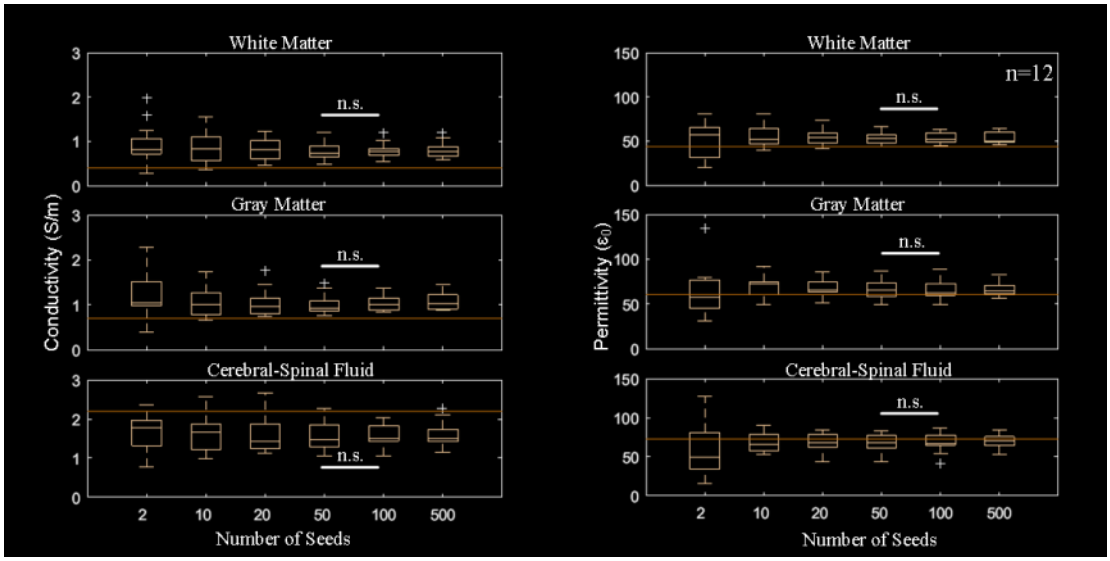

Figure 3.4 Box plots of mean reconstructed EP values of three brain compartments in 12 healthy human subjects showing effects of seed number. Orange line labels *ex vivo* EP values of the corresponding brain tissue at 298 MHz from Gabriel et al. 1996 (S Gabriel et al., 1996). Paired t-test was performed for all brain tissues with 50 and 100 seeds. n.s. not significant.

		Target	Reconstructed
WM	σ	0.41	0.76 ± 0.16
	ε	43.8	50.3 ± 3.9
GM	σ	0.69	1.01 ± 0.16
	ε	60.1	60.9 ± 7.1
CSF	σ	2.22	1.53 ± 0.29
	ε	72.8	63.3 ± 10.8

σ in S/m and ε in ε_0

Table 3.1 Reconstructed EPs of the healthy human brain compartments from 12 subjects. WM, white matter; GM, gray matter; CSF, cerebral-spinal fluid. Reconstructed EPs are shown as mean ± standard deviation.

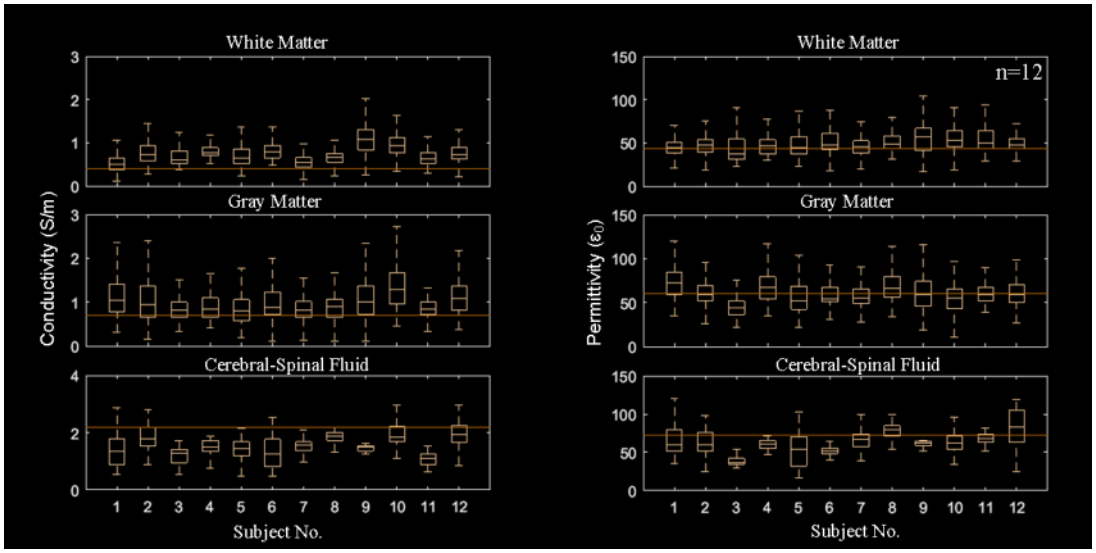

Figure 3.5 Box plots of reconstructed EP values of brain compartments in each individual human subject. Orange line labels *ex vivo* EP values of the corresponding brain tissue at 298 MHz from Gabriel et al. 1996 (S Gabriel et al., 1996).

3.5 Conclusion and Discussions

A novel strategy to automatically choose integration seeds for gEPT brain imaging has been proposed, and imaging results from 12 subjects have been reported. The reconstructed conductivity and permittivity converge to stable values when larger than 20 seeds are used. Enhanced robustness and less variability are observed compared to the subjective single-seed gEPT method. This technology holds promise to facilitate an objective and fully-automated EPT approach for *in vivo* imaging of human brain.

In this study, the EPs of the seeds were calculated by local Helmholtz equation, and then used to inform gEPT reconstruction. A large number of seeds help to stabilize the results due to the reduced weighting on erroneously chosen seeds. To further reduce reconstruction bias by the symmetry assumption made by gEPT, it is desirable to test this algorithm with only g_+ data derived from B_1^+ (Wang et al., 2017).

We observe consistent EP values of brain tissues in our cohort of 12 human subjects, which are close yet not equal to the *ex vivo* values reported in the widely referenced work by Gabriel et al (S. Gabriel et al., 1996). This discrepancy is potentially due to the *in vivo* nature of EPT versus *ex vivo* probe measurements. For *in vivo* imaging case, blood infiltration in gray matter and white matter might account for the increase in conductivity, whilst having minimal effects on permittivity (Semenov et al., 2017). Another source of discrepancy is the fitting of the *ex vivo* data to the mathematical model (Cole-Cole dispersion model). Retrieval of EPs at specific frequencies using this model only gives approximation to the actual measurement results, which subject to fitting and interpolation errors.

In consistency with *ex vivo* measurement results, considerable intra-subject variation of each brain compartment can be observed for *in vivo* imaging results, potentially induced by the natural heterogeneity of tissues due to differences in constituents and blood infiltration. Inter-subject variability exists as well, which has been attributed to age and the physical condition of body (Peyman et al., 2009).

Considering the different physiology of *in vivo* versus *ex vivo* cases, natural heterogeneity of tissues, as well as the inter-subject variation due to body condition, it is expected that *in vivo* subject-specific EPs obtained by EPT can contribute to additional accuracy in EM modeling and management, which could be very important especially for EM safety applications, such as estimation of local SAR in MRI exams.

Future studies may utilize large animal models to be able to measure EPs *in vivo* using gEPT, *in vivo* using probe and *ex vivo* using probe, to narrow down the sources of the measurement discrepancy. It would also be desirable to determine how much effect this discrepancy would make when evaluating local SAR.

Chapter 4 - CONtrast Conformed Electrical Properties Tomography (CONCEPT) for Human Brain Imaging

4.1 Introduction

The mathematical problem of inferring tissue EPs from MRI measurable, circularly-polarized magnetic field B_1 manifests as a nonlinear partial differential equation (Liu et al., 2017b; Katscher and van den Berg, 2017). In order to decrease the condition number and to obtain numerical stability, conventional EPT methods make the assumption that tissue EPs are piece-wise homogeneous, leading to a simplified reconstruction method known as "Helmholtz equation". This assumption eliminates the EP spatial variation term, and one B_1 distribution obtained with a quadrature volume coil suffices for a successful EP reconstruction. Actual EPs in the human body, however, are spatially heterogeneous, yielding boundary artifact and noise amplification that significantly thwart proper interpretations of Helmholtz-equation based EP reconstruction.

Recently, efforts have been made to address boundary artifacts coming from the Helmholtz equation. One potential solution is to utilize structural MR images to inform EP reconstruction on piecewise areas of relatively uniform contrast. This can be done by using a spatially weighted reconstruction kernel or adding regularization terms based on edge information (Ropella and Noll, 2016). However, structural MRI contrasts and EP contrast do not rely on the same mechanism, therefore, spatial boundaries defined by

their respective spatial variations do not necessarily coincide, which may bias the EP reconstruction process. Moreover, signal intensity in structural MRI is highly dependent on which MR sequences and parameters are used, creating additional sources of potential inconsistency that may propagate to EPs.

Alternatively, a multi-channel RF coil array can be used to effectively address the boundary artifact issue and B_1 field assumptions by leveraging a plurality of B_1 measurements (Katscher et al., 2012b; Zhang et al., 2013a; Sodickson et al., 2013). Gradient-based EPT (gEPT) solves a pixel-wise inverse problem using both transmit B_1 and receive B_1, or B_1^+ and B_1^-, to retrieve EP gradient, followed by its spatial integration based on a user-assigned seed point (Liu et al., 2015). This method successfully retrieves both conductivity and permittivity in high quality with improved robustness against noise. Nevertheless, two caveats need to be taken into consideration which may cause errors in the reconstruction results: i) symmetry assumption about RF coil structure and imaged target; ii) subjective assignment of integration seeds, i.e. tissue voxels with presumptive EP values.

In this chapter, a novel EPT approach, dubbed CONtrast Conformed Electrical Properties Tomography (CONCEPT), is reported that is based on a linear inverse problem regularized by intermediate EP gradient information, using only B_1^+ maps with relative phase information from a multi-channel RF coil array. Compared to gEPT, it is not based on symmetry assumptions, nor does it require subjective assignment of integration seed points. Numerical simulations of a digital phantom and a realistic human head model have been performed to illustrate the concept of the proposed approach and

to evaluate its performance under various noise levels. A phantom experiment has been performed at 7 T to demonstrate its applicability in realistic settings. CONCEPT extends the generality of gEPT and holds promise for clinical applications using a generic multi-transmit RF coil.

4.2 Theory

In this section, we first derive the central physical equation from the governing electromagnetic theory that relates the measurable relative B_1^+ to EPs. We then introduce a discriminated regularization strategy using the intermediate EP gradient values, which represents the core of CONCEPT. Lastly, we describe an algorithm based on Alternating Direction Method of Multipliers (ADMM) to rapidly solve the central optimization problem derived from the previous steps. The reconstruction flowchart is shown in Fig. 4.1.

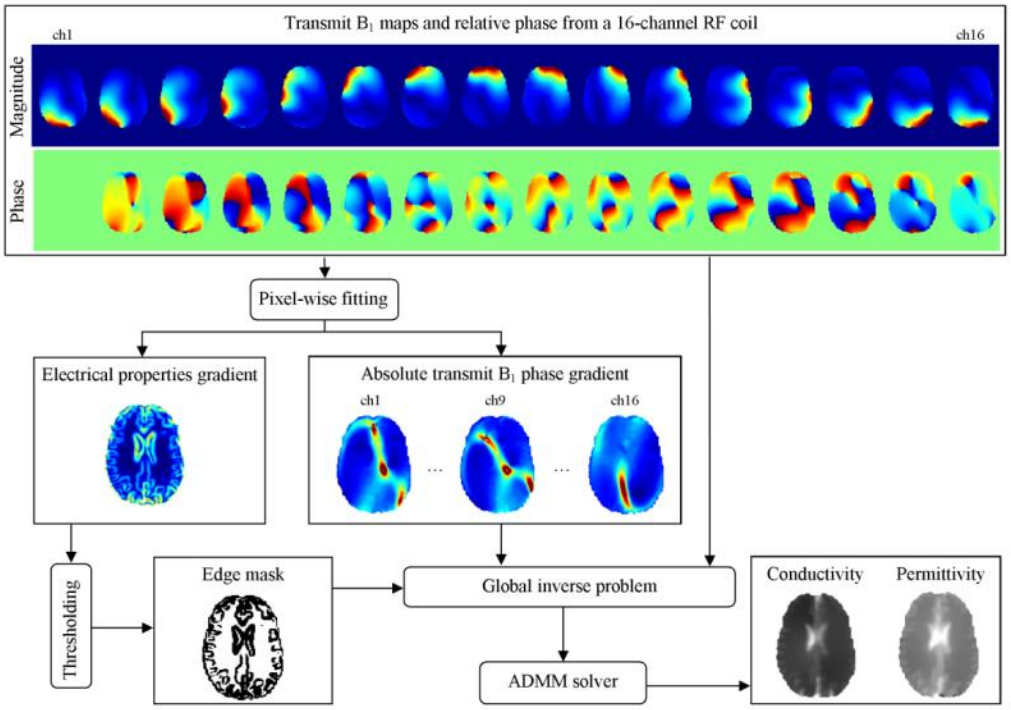

Figure 4.1 Reconstruction flowchart of CONCEPT.

4.2.1 Derivation of the Data Fidelity Term

We start from solving Equ. 3.5 to retrieve the spatial gradient of absolute B_1^+ phase $\nabla\varphi^+$, as well as $g_w = g_+$ and g_z, given that at least four channels are employed (Liu et al., 2015). The retrieved $\nabla\varphi^+$ can be re-introduced back into Equ. 3.5 and reformed into a linear partial differential equation (PDE) in 2D with respect to the scaled complex admittance $\gamma_c = \frac{1}{\omega\varepsilon_c}$

$$(\nabla^2 B_1^+ - \frac{\partial B_1^+}{\partial z} g_z)\gamma_c + \left(\frac{\partial B_1^+}{\partial x} - i\frac{\partial B_1^+}{\partial y}\right) \cdot \left(\frac{\partial \gamma_c}{\partial x} + i\frac{\partial \gamma_c}{\partial y}\right) = -\omega\mu_0 B_1^+ \qquad (4.1)$$

with unknown terms written in red. The spatial gradient term of γ_c can be discretized using central difference method

$$\frac{\partial \gamma_c}{\partial x} + i\frac{\partial \gamma_c}{\partial y} = \frac{\gamma_c(x+1,y) - \gamma_c(x-1,y)}{2dx} + i\frac{\gamma_c(x,y+1) - \gamma_c(x,y-1)}{2dy} \tag{4.2}$$

where (x, y) is spatial location indices, dx and dy are step size along x and y directions, respectively. As such, Equ. 4.1 can be written as a linear inverse problem for each transmit channel k

$$A_k \Upsilon = b_k \tag{4.3}$$

where $\Upsilon \in \mathbb{C}^N$ contains γ_c values of all N pixels in a region of support Ω, $A_k \in \mathbb{C}^{N\times N}$ is a sparse matrix with five nonzero elements in each row, and $b_k \in \mathbb{C}^N$ is a vector of scaled B_1^+. The inverse problems derived from K different transmit channels can be concatenated as

$$A\Upsilon = b \tag{4.4}$$

where $A = [A_1; A_2; \dots; A_K]$, $b = [b_1; b_2; \dots; b_K]$. We utilize L_2-norm of the residue, $\|A\Upsilon - b\|_2^2$, as a metric of data fidelity to the B_1^+ measurements, which is optimized by the pseudo-inverse of Equ. 4.4

$$\Upsilon_{PDE} = (A^H A)^{-1} A^H b \tag{4.5}$$

This solution is referred to as "PDE" in this paper.

4.2.2 Discriminated Regularization

Direct inversion of Equ. 4.4 results in spatially pervasive reconstruction errors due to PDE nature of the problem, intensified by noise effects and inaccuracies in B_1^+

measurements. Furthermore, numerical errors due to the finite difference model of the problem also deteriorate image quality. Therefore, we propose to use the intermediate variable g_w as prior information to determine the EP transition area and guide image reconstruction. To start, we hard-threshold $|g_w|$ to generate two binary masks

$$\begin{cases} W = (|g_w| \geq \kappa) \cap \Omega \\ \bar{W} = (|g_w| < \kappa) \cap \Omega \end{cases} \tag{4.6}$$

where κ is an empirical threshold so that approximately 30% of the pixels in Ω are identified as transition area. In the homogeneous area $\bar{W} = 1$, the L_2-norm of γ gradient is minimized to simultaneously suppress large spatial variation and error propagation. In the transition area W, the L_1-norm of γ gradient is minimized to promote edge sparsity. Therefore, the central reconstruction is formulated as

$$\min_{\Upsilon} \frac{1}{2}\|A\Upsilon - b\|_2^2 + \lambda_1\|W\Psi\Upsilon\|_1 + \lambda_2\|\bar{W}\Psi\Upsilon\|_2^2 \tag{4.7}$$

where Ψ is the finite difference operator calculating $\nabla\gamma$ in the region of support. Since the regularization is informed by intermediate EP contrast instead of structural MRI, this technology is named as "CONtrast Conformed Electrical Properties Tomography", or CONCEPT.

4.2.3 Solving the Central Problem Using Alternating Direction Method of Multipliers

Equ. 4.7 is a large-scale optimization problem involving simultaneous minimization of L_1-norm and L_2-norm. Conventional gradient-based methods, such as gradient descent or conjugate gradient method, are inefficient for solving this type of problem due to the non-smoothness of L_1-norm and the requirement of evaluating function gradient in each

iteration. Alternatively, we propose to use Alternating Direction Method of Multipliers (ADMM) to solve Equ. 4.7. ADMM is based on the philosophy of "divide and conquer" in algorithm design: it splits the original complicated problem into a series of simpler sub-problems, which are sequentially addressed until a consensus is reached (Boyd et al., 2011). ADMM has received increasing attention due to its high efficiency for large-scale image reconstruction problems, especially those with sparsity and low-rank constraints (Zhao et al., 2015; Akçakaya et al., 2014; Asslländer et al., 2018).

In our implementation, we first combine the two L_2-norm terms in Equ. 4.7

$$\min_{\Upsilon} \frac{1}{2}\|E\Upsilon - c\|_2^2 + \lambda_1\|W\Psi\Upsilon\|_1 \tag{4.8}$$

where $E = [A; \lambda_2\bar{W}\Psi]$ and $c = [b; \mathbf{0}]$. Introducing an auxiliary variable z so that Equ. 4.8 is equivalent to

$$\min_{\Upsilon}\frac{1}{2}\|E\Upsilon - c\|_2^2 + \lambda_1\|z\|_1 \quad s.t. \;\; W\Psi\Upsilon - z = 0 \tag{4.9}$$

The augmented Lagrangian can be formed as

$$\begin{aligned} L_\rho(\Upsilon, z, u) = \frac{1}{2}\|E\Upsilon - c\|_2^2 + \lambda_1\|z\|_1 + Re\left(\rho u^H(W\Psi\Upsilon - z)\right) \\ + \frac{\rho}{2}\|W\Psi\Upsilon - z\|_2^2 \end{aligned} \tag{4.10}$$

where u is the multiplier and $\rho > 0$ is the augmented Lagrangian parameter. We can express ADMM updates as

$$\begin{aligned} \Upsilon^{k+1} &= arg\min_{\Upsilon} L_\rho(\Upsilon, z^k, u^k) \\ &= arg\min_{\Upsilon}\frac{1}{2}\|E\Upsilon - c\|_2^2 + Re\left(\rho(u^k)^H(W\Psi\Upsilon - z^k)\right) + \frac{\rho}{2}\|W\Psi\Upsilon - z^k\|_2^2 \end{aligned}$$

$$= arg\min_{\Upsilon} \frac{1}{2}\|E\Upsilon - c\|_2^2 + \frac{\rho}{2}\|W\Psi\Upsilon - z^k + u^k\|_2^2$$

$$= (E^H E + \rho\Psi^H W^H W\Psi)^{-1}\Big(E^H c + \rho W\Psi(z^k - u^k)\Big)$$

$$z^{k+1} = arg\min_{z} L_\rho(\Upsilon^{k+1}, z, u^k)$$

$$= arg\min_{z} \lambda_1\|z\|_1 + Re\Big(\rho(u^k)^H(W\Psi\Upsilon^{k+1} - z)\Big) + \frac{\rho}{2}\|W\Psi\Upsilon^{k+1} - z\|_2^2$$

$$= arg\min_{z} \lambda_1\|z\|_1 + \frac{\rho}{2}\|z - W\Psi\Upsilon^{k+1} - u^k\|_2^2$$

$$= S_{\lambda_1/\rho}(W\Psi\Upsilon^{k+1} + u^k)$$

$$u^{k+1} = u^k + W\Psi\Upsilon^{k+1} - z^{k+1}$$

where $S_\tau(a)$ denotes the soft-thresholding function of a with τ. z^0 and u^0 are initialized with zero vectors. Note that the algorithm does not require initialization of Υ, since Υ^1 is calculated from z^0 and u^0 in the first iteration. The stopping criterion is

$$\frac{\left\|\Upsilon^{k+1} - \Upsilon^{k}\right\|_2}{\|\Upsilon^{k+1}\|_2} \leq \text{tolerance}, \qquad \text{or} \quad k > k_{max} \tag{4.11}$$

We observed that the algorithm typically converges within 15 iterations using $tolerance = 10^{-4}$.

4.3 Methods

4.3.1 Numerical Simulations

Electromagnetic simulations were performed in Finite-Difference Time-Domain (FDTD) based software (Sim4Life version 3.4, ZMT, Zurich, Switzerland). The 16-channel microstrip coils array used in the experiment was numerically modeled and

loaded with a cylindrical phantom containing tube anomalies, or a realistic head model (Duke Model, Virtual Family), as shown in Fig. 4.2. The digital phantom was 160 mm tall, with a long axis of 210 mm and a short axis of 168 mm, and was assigned the mean electrical properties of brain at 298 MHz (0.55 S/m and $52\,\varepsilon_0$). Five sets of tube anomalies with diameters of 5 mm, 10 mm and 20 mm were evenly distributed in azimuthal direction, spanning the physiologically relevant EPs range of 0.2-2.5 S/m and $40\varepsilon_0$-$100\varepsilon_0$. For the head model, EPs of various tissues were assigned based on Gabriel et al (S. Gabriel et al., 1996). The imaged object was positioned in the center of the coil, mimicking actual experimental setup.

Spatially anisotropic discretization of the models was performed by the software based on their geometry and EP distributions to achieve the optimal performance. A maximal spatial step of 1.5 mm was prescribed inside the phantom/head model to ensure high precision. The 16 channels of the coil were excited sequentially with a normalized input power of 1 W. The simulated complex B_1^+ field was exported to MATLAB and re-gridded to a homogenous $1.5 \times 1.5 \times 1.5$ mm^3 grid using cubic splines. Relative B_1^+ field was calculated taking each channel as reference. Complex white Gaussian noise was added to B_1^+ to adjust SNR to desired levels.

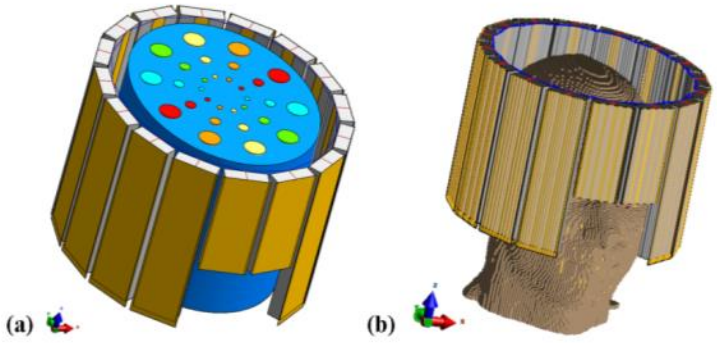

Figure 4.2 Simulation setup. The 16-channel microstrip RF coils array is loaded with a numerical phantom (a) and Duke head model (b). The latter is shown as voxels after discretization.

4.3.2 Phantom Experiment

An agar phantom was constructed to validate the performance of CONCEPT in realistic settings. The "background" or main body of the phantom contained deionized water, agar, NaCl, $NiCl_2 \cdot 6H_2O$ with a mass ratio of 1000:15:1.12:0.5. EPs of the phantom at 298 MHz were measured using a dielectric probe (85070E, Keysight Technologies) as 0.294 S/m and $78.6\varepsilon_0$. The main body was poured into a cylindrical jar with 120-mm diameter and 150-mm height. The contrast solutions were prepared based on deionized water, with NaCl to adjust conductivity and polyvinylpyrrolidone (PVP) to adjust permittivity (Ianniello et al., 2018). Three solutions with different EPs were prepared and measured using the probe. Solutions were filled into a 25-mm-diameter tube and a 5-mm-diamter straw, and inserted into the phantom background. The whole phantom was allowed to stand for 24 hours in room temperature to solidify.

Experiments were performed on a 16-channel Siemens 7T system equipped with 16x1 kW power amplifiers (CPC, Hauppauge, NY) with their transmit power and phase remotely controlled by a phase/gain control unit, interfaced with locally developed MATLAB-based software toolbox. A 16-channel RF coils array, consisting of microstrip elements aligned with the main magnetic field direction, was used to obtain multiple relative B_1^+ patterns. The coils array was connected to the MRI system through a custom 16-channel T/R switch box. Each coil element was tuned and matched at the operating frequency (297.2 MHz) when loaded with object under detection. B_1^+ magnitude map from each channel was acquired using a hybrid method of multi-slice gradient-echo (GRE) and 3D actual flip-angle imaging (AFI) method (Yarnykh, 2007; Van de Moortele et al., 2007, 2005). For the former, each coil element was excited sequentially in small-flip-angle regime (< 15°), with TR = 76 ms, TE = 3.3 ms and 8 averages; For the latter, two shimmed B_1^+ patterns resembling CP+ mode and CP2+ mode, respectively, were imaged with nominal flip angle = 55°, TR = 20/120 ms and TE = 3.2 ms. Hybrid B_1^+ reconstruction of each transmit channel was initially performed for the two shimmed patterns separately, then combined with weights of the flip angle map, so as to circumvent inaccuracies due to RF nulling spots present in the CP+ and CP2+ B_1^+ maps. The relative B_1^+ maps were acquired with in-plane resolution of 1.5 × 1.5 mm^2 over a stack of 12 contiguous slices of 3 mm thickness.

4.3.3 Image Reconstruction

Simulated noisy data and experimental data were de-noised using a low-pass Gaussian filter with a kernel size of $5 \times 5 \times 3$ voxels and standard deviation of $1.2 \times 1.2 \times 0.8$ voxels. The spatial gradient and Laplacian of B_1^+ were generated based on second order polynomial fitting using a $5 \times 5 \times 3$ Savitzky-Golay filter (Lee et al., 2015). Image reconstruction was performed using MATLAB codes developed in-house, running on a desktop with a 3.4 GHz GPU and 32 GB RAM.

4.4 Results

4.4.1 Digital Phantom Simulation

Reconstruction results using Helmholtz equation, PDE, gEPT and CONCEPT are compared in Fig. 4.3. For Helmholtz equation, accurate reconstruction is limited to large homogenous areas, such as the inside of large tubes as well as the background. Severe oscillations can be observed at the interface of different contrast components. In particular, reconstruction results of small structures (5 mm and 10 mm tubes) are dominated by boundary artifact. For PDE, boundary artifact is significantly mitigated, thanks to the inclusion of the EP variation term. Nevertheless, checkboard-like artifacts still appear due to the use of finite difference as an approximation of spatial derivative (white arrow). This artifact is more pronounced in the tubes with large EP values because of higher contrast to the background. In addition, erroneously reconstructed values can be identified near the phantom boundary close to individual RF coil elements (green arrows).

This artifact arises from inaccurate estimation of local high-order spatial derivatives of B_1^+ due to its rapid attenuation near each coil element. As shown in the profiles in Fig. 4.3b, without constraints, such artifacts can bleed into the contrast tubes and bias reconstruction results. For gEPT, one seed point in the center of the phantom was used to implement the algorithm (red asterisk). High-frequency checkboard artifact exists in both EP maps, on top of low-frequency bias induced by violation of the "symmetry assumption". The EP profiles demonstrate spatially dependent bias in the reconstruction result, which tends to be smaller near the seed point and accumulates going outward radially. For CONCEPT, reconstructed EP values and profiles are close to those of the target. The checkboard artifact and spatial bias are minimized thanks to the informed regularization.

Reconstructed EP images using CONCEPT at various SNR levels are shown in Fig. 4.4a. The obtained EP values inside the large tubes are fitted against the target values in Fig. 4.4b. Accurate conductivity and permittivity can be obtained for SNR = 200 and 100 within the ranges of interest, with reconstruction errors being ≤ 0.15 S/m for conductivity and $\leq 5.0\varepsilon_0$ for permittivity. The smallest tubes can also be well differentiated from the background and from each other. At SNR = 50, the fitting results show global overestimation in both contrasts, even though not prominent on the reconstructed images. Notably, overestimation is pronounced for the tube with the largest EPs, a phenomenon that has been reported in previous studies (Voigt et al., 2011; Marques et al., 2014; Hafalir et al., 2014). Potential explanations for this overshoot are discussed in the appendix.

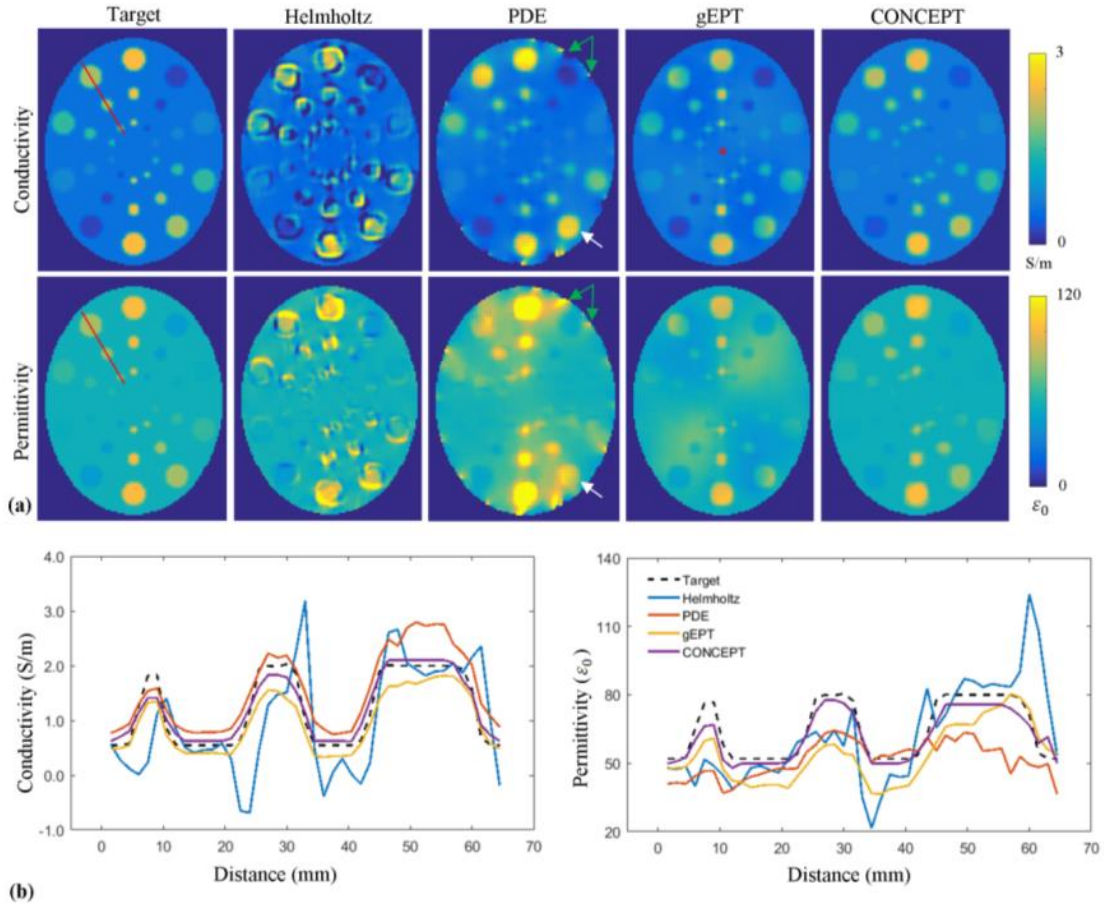

Figure 4.3 Comparison of different reconstruction methods using simulated phantom data. (a) Reconstructed conductivity and permittivity using Helmholtz equation, PDE, gEPT and CONCEPT are compared with target maps. Red asterisk labels position of the seed point used by gEPT. Both transmit and receive B_1 were employed for gEPT. Other methods do not require seeds or receive B_1. White and green arrows denote checkboard artifact and B_1 peak related artifact, respectively. (b) Reconstructed EP profiles along the red line on the target maps in (a).

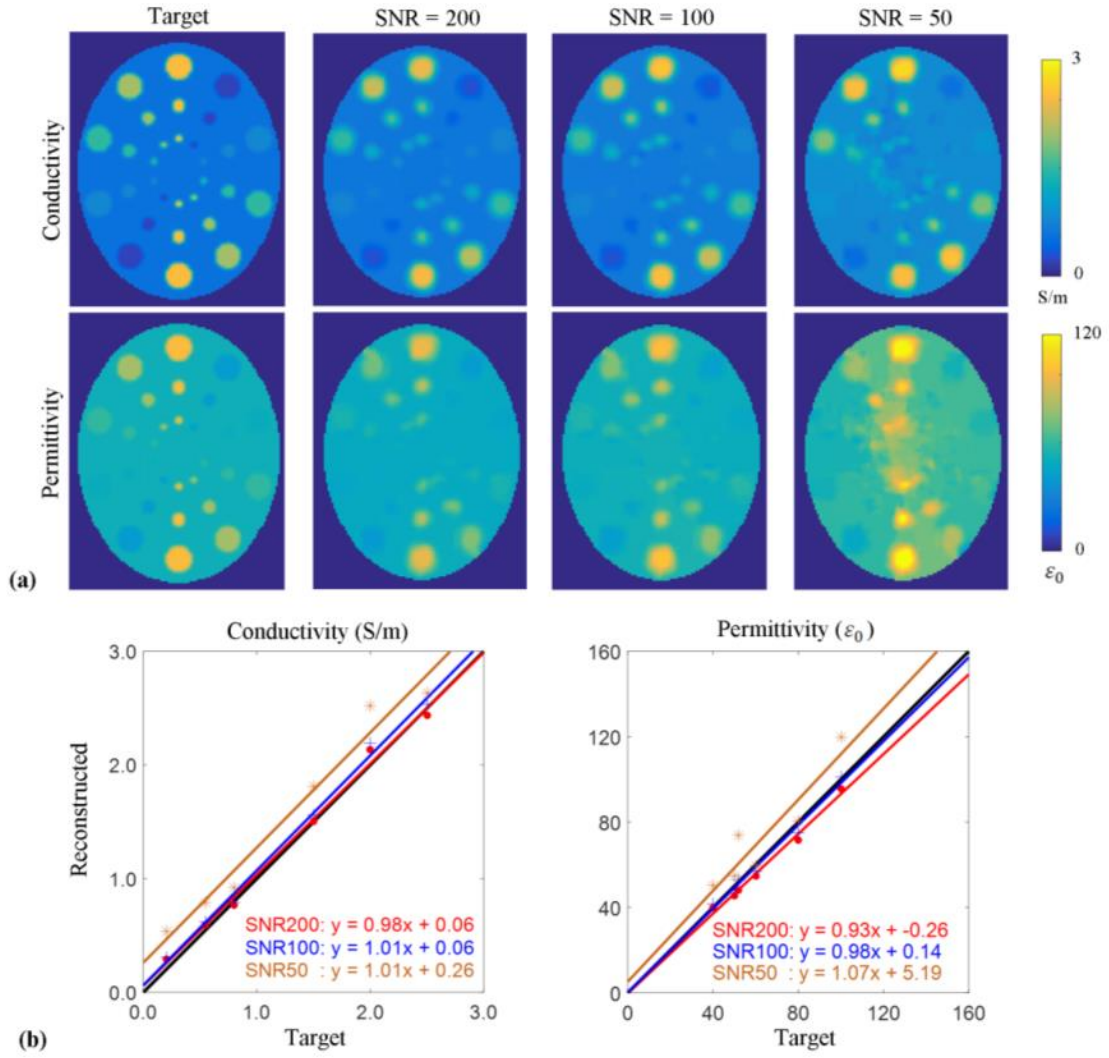

Figure 4.4 CONCEPT reconstruction results at SNR = 200, 100 and 50. (a) Reconstructed conductivity and permittivity maps. (b) Linear fitting results of the retrieved values inside the largest tubes against the target values.

4.4.2 Digital Brain Simulation

Three axial slices of the reconstructed brain model with a spatial gap of 12 mm are shown in Fig. 4.4. Note that the low-pass filter was not applied to the noise-less B_1^+ data, but only to the noisy B_1^+ (SNR = 50). For both SNR levels, all three slices show

successful reconstruction of the contrasts amongst major brain tissues, e.g. white matter (WM), gray matter (GM) and cerebrospinal fluid (CSF). The reconstructed values of these three tissues are summarized in Table 4.1. Consistent with the digital phantom results, we observe overestimation in the permittivity of CSF, even for the noiseless case. This is potentially due to the increased complexity of the real-3D Duke model compared to the 2D-projected phantom model. The magnitude of this overestimation is smaller for the noisy reconstruction because of the smoothing effects of the low-pass filter.

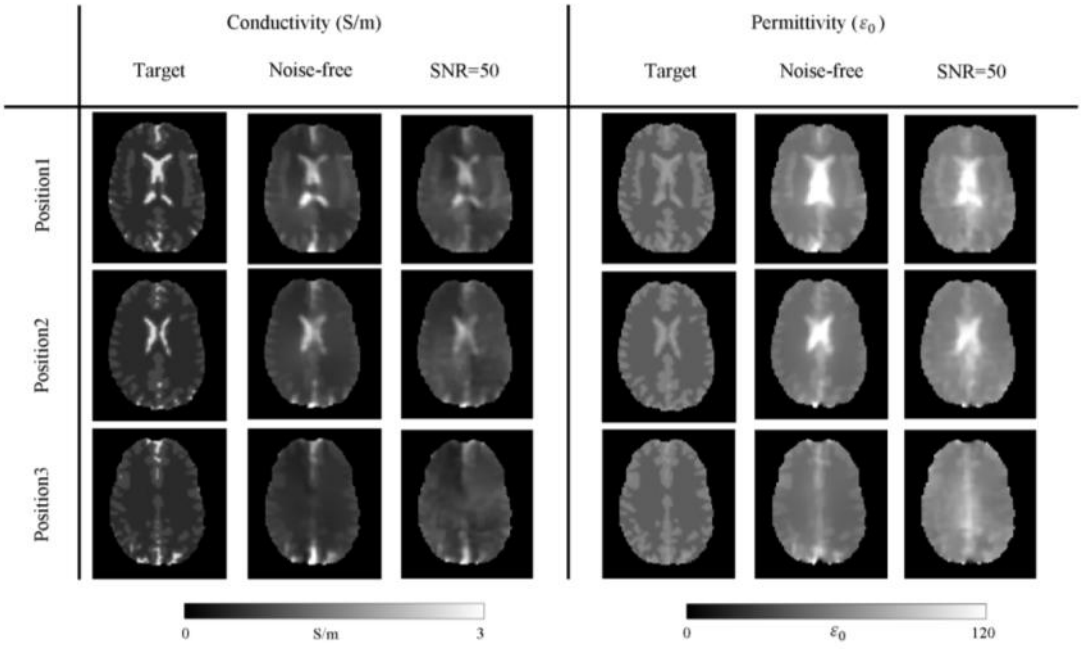

Figure 4.5 Reconstructed EPs of a simulated 3D Duke head model. Shown are the target maps and reconstruction results using noise-free B_1 data as well as noisy B_1 with SNR = 50. The three axial slices are separated by 12 mm.

		Target	Noise-free	SNR = 50
WM	σ	0.41	0.58 ± 0.10	0.62 ± 0.12
	ε	43.8	47.2 ± 4.3	52.0 ± 4.8
GM	σ	0.69	0.63 ± 0.30	0.68 ± 0.33
	ε	60.1	56.1 ± 9.5	58.9 ± 9.2
CSF	σ	2.22	1.70 ± 0.34	1.57 ± 0.29
	ε	72.8	105.2 ± 9.6	100.8 ± 7.0

σ in S/m and ε in ε_0

Table 4.1 Reconstructed EPs of the duke head model.

4.4.3 Phantom Experiment

A structural image of the phantom and B_1 images from a single channel are shown in Fig. 4.6. Local spotty artifacts can be seen in the hybrid B_1 map when using a single shim pattern (Fig. 4.6c white arrows). These artifacts occur at the locations of RF nulls due to complex destructive interference of B_1^+ between channels (Van de Moortele et al., 2005). By contrast, B_1 image obtained merging two shim patterns is free of such errors, bearing high resemblance to the B_1 pattern measured by AFI (Fig. 4.6b).

Based on the combined hybrid B_1 images, reconstructed EPs of the phantom are shown in Fig. 4.7. As an intermediate quantity, the spatial variation or gradient strength of EPs across the phantom can be robustly retrieved, enabling a clean separation of EP contrast boundary (Fig. 4.7a). Importantly, compared to the Helmholtz based reconstruction, CONCEPT gives accurate conductivity reconstruction results not only in

homogenous areas but also around contrast boundaries. In addition, all three 5-mm small tubes are visible from the reconstructed map. Similar to the simulations, there is overshot in the reconstructed permittivity of the tubes with high EP values (tube III). Reconstruction errors of the other tubes are relatively smaller.

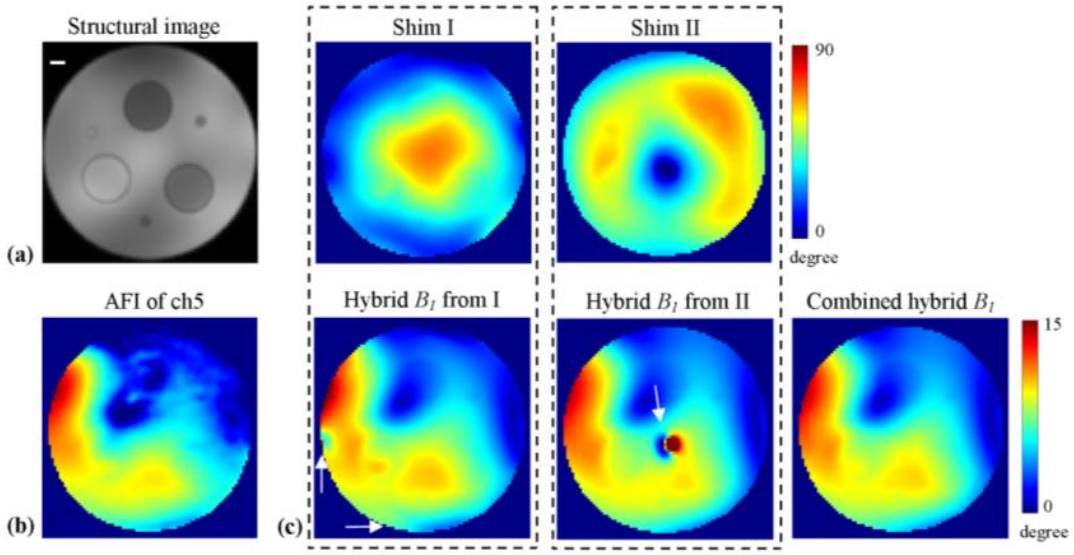

Figure 4.6 Hybrid transmit B_1 mapping based on dual shims. (a) An axial slice of the agar phantom used in the experiment. Scale bar is 10mm. (b) Transmit B_1 magnitude from channel 5 (ch5) measured using AFI. (c) Hybrid B_1 mapping results of ch5 based on CP-like shim (I), CP2+-like shim (II) and combined. The shimmed B_1 patterns were measured using AFI. White arrows point to locations with inaccurate calculated B_1 due to RF nulls in the corresponding shimmed B_1 pattern.

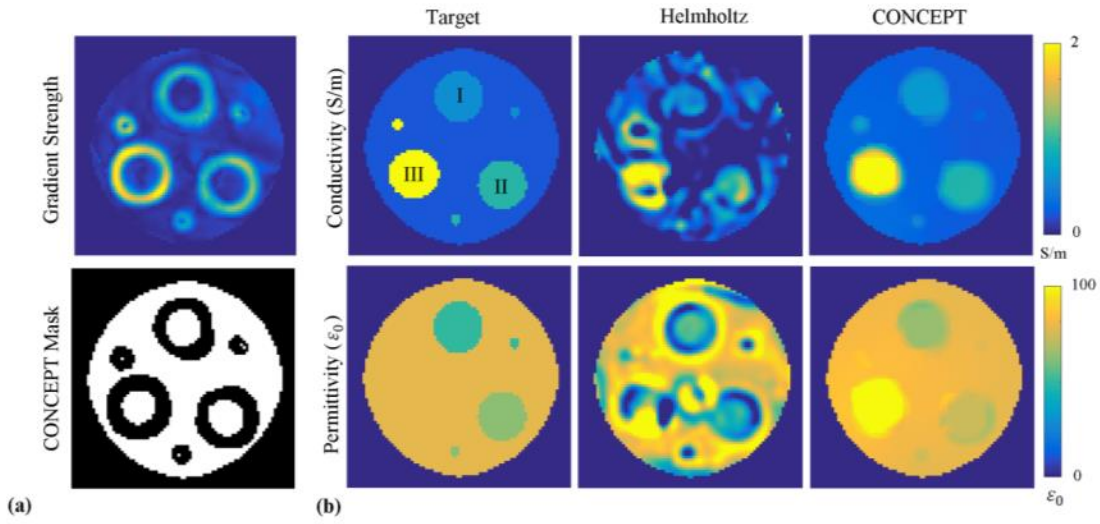

Figure 4.7 Phantom reconstruction results. (a) Intermediate gradient strength distribution and CONCEPT mask generated by hard-thresholding. (b) Comparison of the reconstruction results using Helmholtz equation and CONCEPT.

		Target	Reconstructed
Tube I	σ	0.65	0.70 ± 0.05
	ε	50.2	65.0 ± 1.6
Tube II	σ	1.02	0.98 ± 0.02
	ε	62.7	73.6 ± 0.7
Tube III	σ	2.14	2.14 ± 0.07
	ε	78.8	124.0 ± 4.3

σ in S/m and ε in ε_0

Table 4.2 Reconstructed EPs of the agar phantom.

4.5 Conclusion and Discussions

In this study, we propose a novel approach, dubbed "CONCEPT", to retrieve EPs from MRI using multiple RF transmission. CONCEPT leverages on the intermediate EP gradient information for edge detection and discriminated regularization. The resultant large-scale, mixed L_1 and L_2 norm image reconstruction problem is solved efficiently using ADMM. A systematic investigation using numerical simulations and phantom experiments at 7 T MRI demonstrate its capability to retrieve accurate EP values in large homogeneous areas ($\geq$ 20 mm), as well as to detect small structures down to 5 mm, and to faithfully reflect the EP transition zone. For conductivity reconstruction, CONCEPT is robust against noise contamination and 3D model complexity. For permittivity imaging, an over-estimation is observed especially for areas with high EP values, which is consistent with previous findings.

The mere Helmholtz-based approaches of MREPT suffer from boundary artifact, spatial bias, and noise amplification effects, due to a substantial simplification of the governing physical equations and to the use of high-order spatial differentiation operators. These adverse effects can be partially mitigated using numerical regularization with prior information such as contrast edges detected by structural MRI (Ropella and Noll, 2016). Nevertheless, spurious EP contrast may be introduced, since it is fundamentally different from magnetic relaxation contrasts and does not necessarily spatially coincide with structural MRI. In comparison, CONCEPT exploits EP gradient information directly derived from B_1^+, thus it is in principle immune to other sources of contrast such as MR relaxation effects.

CONCEPT requires at least four transmit channels to solve the central reconstruction problem. Compare to state-of-the-art gEPT, CONCEPT has the following merits. Firstly, the reconstruction process does not require assignment of integration seed, which is unavailable in realistic settings. Secondly, B_1^- is no longer needed, leading to a shorter scan time and improved patient compliance. Last but not least, the imaging setup, including both the subject brain and RF coil, does not need to be symmetric, opening the potential to image diseased brain and irregularly shaped body organs using customized RF coil. In fact, since B_1^- and B_1^+ are completely disentangled in CONCEPT, one is no longer limited to transceiver RF coil arrays. Instead, separate transmit and receive coil arrays, that are more ubiquitous than customized transceiver arrays, can be utilized. In addition, such coil type generally has a higher count of receive elements with dedicated high-performance electronics in a close proximity to the imaged target, which significantly improves SNR for MR data acquisition. Additional transmit elements could also be used to obtain a larger number of different B_1^+ patterns to improve the conditioning of the inverse problem.

In its current form, CONCEPT is based on multiple B_1^+ maps, yet its counterpart using multiple B_1^- maps can be derived in a similar way. The major advantage of using multiple B_1^- lies in its high temporal efficiency, since data acquisition can be accomplished in a single acquisition (Marques et al., 2014). However, B_1^- maps are typically weighted by proton density which cannot be removed in a straightforward way. Computing the ratio of B_1^- maps between different channels cancels out the shared proton density weighting, yet the resultant relative B_1^- magnitude cannot be directly utilized by

CONCEPT. Alternatively, proton density can be taken as unknown variables and reconstructed simultaneously with EPs (Liu et al., 2016).

The central equation of CONCEPT (Equ. 4.7) contains two regularization terms, i.e. L_1-norm and L_2-norm of spatial gradient of Υ. The effective areas of these two norms are controlled by a binary mask W that is derived from hard-thresholding the intermediate EP gradient. More advanced regularization strategies may be employed to further improve image quality. Firstly, W could be designed as a continuous function of EP gradient, such as linear or logarithm, to better characterize EP distribution of imaged object and gain robustness against measurement noise. Secondly, the L_1-norm of spatial gradient of Υ, known as total variation (TV), could be replaced by total generalized variation (TGV) containing higher orders of spatial derivative. TGV does not imply the piecewise constant assumption, thus it is capable of alleviating the "staircase" artifact and capturing contrast changes that are naturally continuous (Knoll et al., 2011). Lastly, low-rank constraints could be imposed to better represent different types of tissue, as has been shown in other parametric MRI technologies (Zhao et al., 2015). These features can be added to CONCEPT and solved using ADMM without significant modifications to the current algorithm structure. However, caution needs to be used as a much higher dimension of regularization parameters need to be explored to obtain the optimal imaging outcome.

CONCEPT is based on 3rd order spatial differentiation of B_1^+, since it requires the spatial derivative of $\nabla\varphi^+$ which is calculated from an equation involving $\nabla^2 B_1^+$ (Liu et al., 2015). This makes the algorithm more sensitive to noise contaminations and to motion,

which can only be partially mitigated by regularization. Data pre-processing using intensive low-pass filters can alleviate the adverse effects, yet at a price of resolution loss which can be deleterious when targeting small structures. To image complex structures or human subjects using CONCEPT, improvements in SNR are warranted. This could be achieved by implementation of recently introduced B_1 mapping methods such as DREAM (Nehrke and Börnert, 2012) or Bloch-Siegert shift (Sacolick et al., 2010). In addition, transmit channels could be aggregated to generate a smaller number of "virtual channels" that have better spatial coverage than a single transmit element. The gained SNR can also be traded for shorter scan time or higher resolution as desired.

4.6 Appendix

In this appendix, we propose and analyze potential reasons why the reconstructed permittivity map has more severe distortion and overshot.

Firstly, as pointed by Marques et al. (Marques et al., 2014), given that the real and imaginary part of ε_c can be reconstructed at the same SNR level, a change in permittivity of $10\varepsilon_0$ is commeasurable to a change in conductivity of 0.17 S/m at 7 T. In human brain, the normal physiological range of permittivity is $40\,\varepsilon_0$ - $70\,\varepsilon_0$, corresponding to a conductivity range of 0.68 S/m - 1.19 S/m, which is much narrower than the actual physiological range of conductivity 0.41 S/m - 2.22 S/m. Therefore, permittivity is relatively more susceptible to disturbances such as noise or B_1 inaccuracy.

Secondly, the overestimation in permittivity may originate from conversion of the reconstructed γ_c to conductivity and permittivity. As shown in Fig. 4.8, for pixels with

larger conductivity values, the same value of the real part of γ_c corresponds to two very different permittivity values. The accuracy of reconstructed permittivity is thus highly dependent on the imaginary part of γ_c, which is unfortunately insensitive to permittivity change in this range. For example, two data points shown in Fig. 4.8 have the same conductivity value of 2.2 S/m and the same real part of γ_c. Despite their significant difference in permittivity ($142\varepsilon_0$), there is only 21% difference in the imaginary part of γ_c compared to its dynamic range. Therefore, solving for γ_c instead of ε_c can result in unreasonably larger value of permittivity.

Lastly, reconstruction error on contrast boundary may perfuse to the whole image due to the nature of partial differential equation. Spatially constrained regularization may mitigate this effect but it cannot be eliminated.

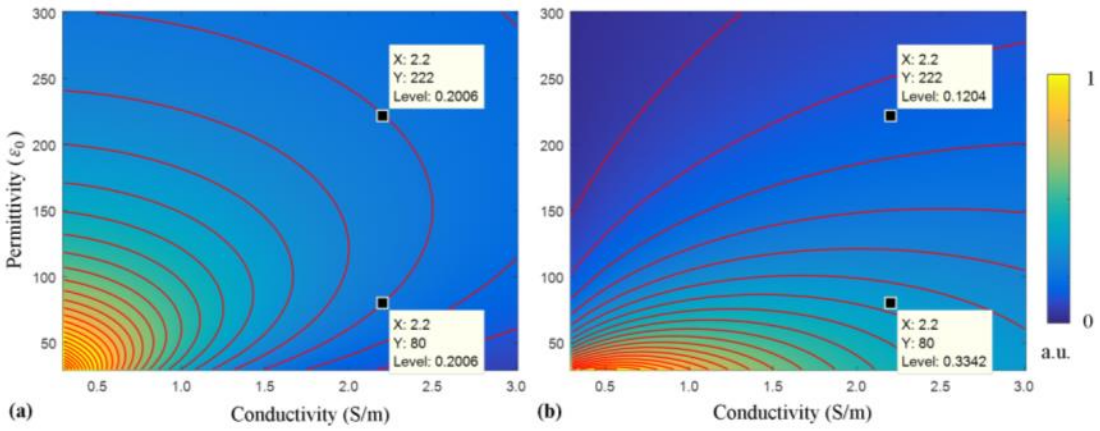

Figure 4.8 Projection maps from conductivity and permittivity to complex admittance. Shown are the normalized real (a) and imaginary (b) parts of admittance as functions of conductivity and permittivity, contoured by red lines with a step size of 0.05.

Chapter 5 - Boundary Informed Electrical Properties Tomography (BIEPT) for Imaging Small Animal Tumor Models

5.1 Introduction

Tumor heterogeneity has various implications for cancer diagnosis, prognosis, patient stratification and treatment assessment. Malignant tumor cells undergo a branched evolution leading to genomic heterogeneity (Meacham and Morrison, 2013). After generations of aggressive proliferation in a chaotic environment, distinct tumor sub-regions or "habitats" emerge with various patterns in metabolism, cellularity, and vasculature (Gatenby et al., 2013; Swanton, 2012). The genomic and phenotypic heterogeneity of a tumor encodes its aggressiveness and outlook, which is also readily revealed by a variety of biomedical imaging modalities and has led to the emergence of radiomics (Aerts et al., 2014; Gillies et al., 2015). Identifying tumor habitats using non-invasive 3-dimensional (3D) imaging techniques holds promise not only to guide biopsy, but also to potentially provide an alternative to invasive diagnostic approaches altogether (O'Connor et al., 2017). Moreover, imaging and quantifying tumor heterogeneity has demonstrated its superiority to tumor size metrics for the early detection of treatment response in personalized targeted therapy (O'Connor et al., 2015).

Conductivity imaging of cancer based on MREPT has been attempted in the human brain, breast, and cervix, showing results consistent with the literature (Shin et al., 2015;

Tha et al., 2018; Balidemaj et al., 2016). However, the reconstruction methods used in these studies are based on the Helmholtz equation that describes electromagnetic wave propagation in a homogeneous medium. Consequently, tumor heterogeneity cannot be appropriately identified, and may instead induce reconstruction artifacts in the resulting EP values and distributions that may significantly jeopardize quantitative measurements (Duan et al., 2016). Moreover, permittivity values are intractable from these studies due to the assumptions made about B_1 in the reconstruction formalism.

A general approach to accurately image EP heterogeneity at high spatial resolution, once developed, is expected to provide valuable information about the underlying tumor pathology. Establishment of the correlation between this new contrast and the tumor hallmarks would pave the way for improved sensitivity and specificity in cancer diagnosis, grading, and monitoring of treatment response. A preliminary framework has been reported by our group for *in vivo* imaging of rat cancer xenografts, which goes beyond the Helmholtz equation and takes into consideration the spatial variation of EPs in the reconstruction model (Liu et al., 2017a). However, this approach requires collecting data during two consecutive MRI scanning sessions with physically flipped experimental setup executed with high precision, which is prone to operational error and consumes precious scan time. Its reconstruction was limited to a small region of interest (ROI) and not based on any external reference seed points for quantitative EP calculation, hindering the ultimate resolution, SNR, and data interpretability across the 3D volume.

In this study, we introduce a boundary informed EPT (BIEPT) approach to quantitatively map tumor EPs *in vivo* with high spatial resolution, using a multi-channel

RF coil array at 7 Tesla. BIEPT demonstrates that EP distributions inside an ROI can be reliably retrieved using the Dirichlet boundary condition and MRI data from only one experimental setup. As such, we minimize opportunities for operational error and shorten the total scan time by half, approaching the ultimate resolution and accuracy prescribed under the current MRI acquisition framework in a feasible time period. The proposed technology was systematically validated using numerical simulations and phantom experiments. EP maps were obtained from two different cancer models with validation from dielectric probe measurements and whole-mount histopathological slides. Based on the results, we report the following discoveries: (I) EP changes are strongly correlated to local pathological features, such as necrosis; (II) EP contrast can be identified for structures as small as 3 mm in size; (III) electrical conductivity and permittivity exhibit differential spatial patterns and temporal evolutions, suggesting that they may help to distinguish unique physio-pathological characteristics between sub-clusters in a tumor; (IV) focal and global EPs elevation can be detected before size reduction in the tumors treated with local chemotherapy.

5.2 Theory

In chapter 3, starting from Maxwell's equations, the essential steps are laid out that eventually lead to a pixel-wise inverse problem linking MRI-measurable multi-channel relative B_1 to the spatial derivative of EPs. Here, a numerical optimization problem is proposed that retrieves tumor internal EP distributions from their Wirtinger derivatives,

with prior information of boundary EPs and use of an L_1-norm edge sparsity constraint. The reconstruction flowchart is shown in Fig. 5.1.

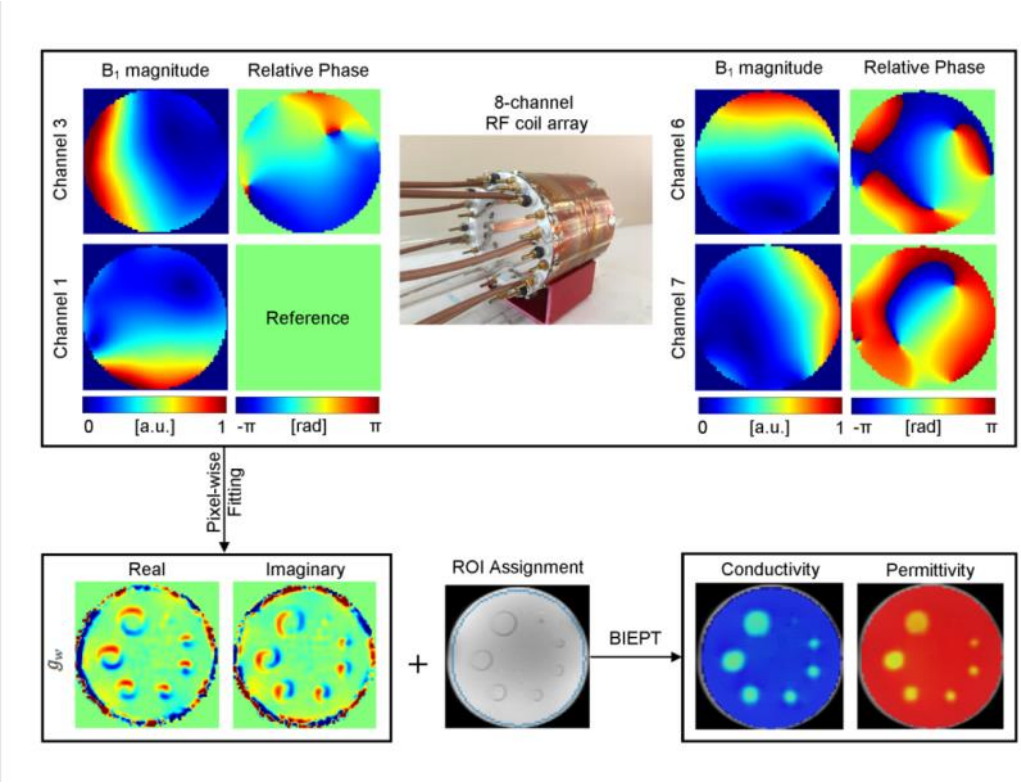

Figure 5.1 BIEPT reconstruction flowchart. Single channel relative B_1 maps are acquired from an 8-channel RF coil array as input to the reconstruction algorithm. Shown are normalized relative B_1 maps from 4 out of the 8 channels for demonstration. Pixel-wise fitting to Maxwell's equations is carried out to retrieve the Wirtinger derivative of EPs. A region of interest (ROI) is assigned, in which boundary informed spatial integration is performed to retrieve the EP distributions. a.u., arbitrary unit.

After solving Equ. 3.5, $g_w = g_+ = (\frac{\partial}{\partial x} + i\frac{\partial}{\partial y}) \ln \varepsilon_c$ can be obtained which is the Wirtinger derivative (Freitag and Busam, 2006) of $\ln \varepsilon_c$ defined on the complex plane $\mathbb{C} \equiv \mathbb{R}^2 = \{(x, y), x \in \mathbb{R}, y \in \mathbb{R}\}$. In this study, we seek the numerical integral of the Wirtinger derivative defined on a simply connected two-dimensional domain with

Dirichlet boundary condition. The central reconstruction problem inside such an ROI Ω is expressed as an equality-constrained convex optimization problem:

$$\begin{aligned} &minimize_{\theta} \ \left\|\left(D_x + iD_y\right)\cdot\theta - \ g_w\right\|^2 + \lambda\|\Delta\theta\|_1 \\ &subject\ to \ \ \theta_{(x_0,y_0)} = \theta_0 \qquad \forall(x_0,y_0)\in\Omega_0 \end{aligned} \tag{5.1}$$

where θ is a vectorized form of $ln\,\varepsilon_c$ inside Ω; D_x and D_y are the spatial derivative operators along x and y directions, respectively; Δ is the spatial Laplacian operator; λ is a regularization parameter determined by L-curve method (Hansen et al., 1999); Ω_0 is a subarea of Ω with known EPs θ_0. Image sparsity is promoted by including the $\|\Delta\theta\|_1$ term that smooths homogeneous patches while preserving sharp edges.

In order to provide a EPs reference area Ω_0 for in vivo imaging of rat tumor xenograft, water-based ultrasound transmission gel was applied over the skin surface on top of the tumor. The gel EPs were measured using a dielectric probe, which reported consistent results (σ = 0.28 S/m, ε_r = $77\varepsilon_0$) during a 4-hour time window at room temperature (22 ℃) and across a temperature range of 22-58 ℃ (Fig. 5.2). The gel also serves as a high-permittivity dielectric pad that boosts local SNR (Yang et al., 2006) and helps to alleviate susceptibility induced magnetic field alteration on the surface of tissue.

For ROI boundary pixels that fall into rat muscle tissue, the following relaxed boundary constraint is used to regularize reconstruction results

$$\|\theta - \ \theta_{tissue}\|^2 \le \delta_0 \tag{5.2}$$

which allows unknown muscle pixels to fluctuate around the average muscle EP values θ_{tissue}, calculated from σ = 0.9 S/m and ε_r = $64\varepsilon_0$, based on our previous study (Liu et

al., 2017a) and further confirmed by probe measurement results from the animal cohort in this study (n = 8, σ: 0.89 $\pm$0.06 S/m, ε_r: 63.6ε_0 $\pm$2.3ε_0).

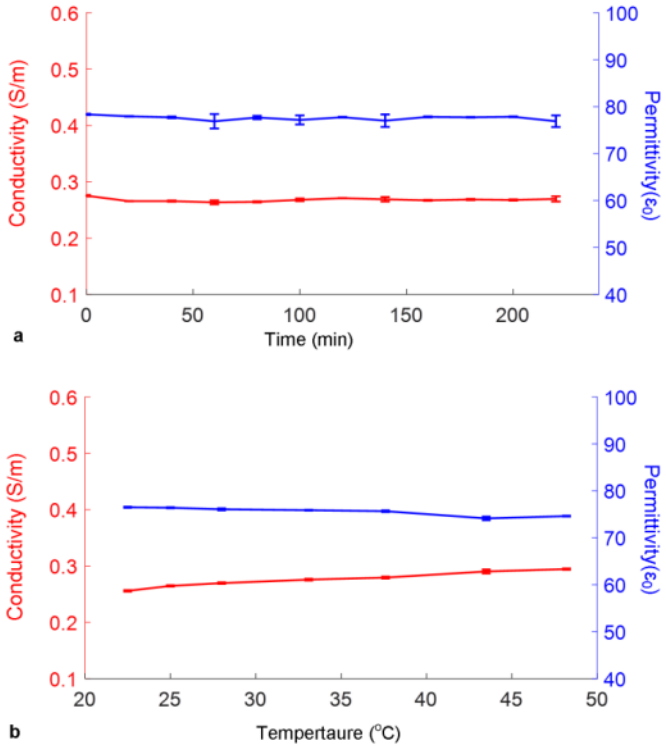

Figure 5.2 Probed conductivity (in red) and permittivity (in blue) of the ultrasound gel in a 4-hour time window at room temperature (22 °C) (a) and across a temperature range of 22-58 °C (b). Data are shown as mean ± standard deviation of three measurements at different locations. (a) Measurement was performed every 20 minutes. Neither conductivity nor permittivity changes significantly in the 4-hour time window. (b) The gel was heated to 50 °C and slowly cooled down in water bath. EPs and the corresponding temperature were measured simultaneously. Neither conductivity nor permittivity changes significantly from room temperature to 48 °C.

5.3 Methods

5.3.1 Numerical Simulation

Radiofrequency electromagnetic simulation was performed in SEMCAD (Schmid & Partner Engineering AG, Zurich, Switzerland) based on the finite-difference-time-domain (FDTD) method. The 8-channel microstrip coil array used in the experiment was numerically replicated in terms of geometrical structure and electrical circuitry. The coil was loaded with a realistic rat model (275 g female rat model, IT'IS Foundation, Zurich, Switzerland) in a similar positioning as in a real experiment. The EP values assigned to the normal composite tissues were extracted from a widely used database (S. Gabriel et al., 1996). A 20-mm-diameter sphere was placed on the left flank of the rat mimicking a tumor xenograft (σ = 1.0 S/m, ε_r = $65\varepsilon_0$). Inside the tumor was a necrotic core with a diameter of 8 mm (σ = 1.3 S/m, ε_r = $76\varepsilon_0$). The discretization grid with spatially variable density was generated by software based on the material and geometry of the model. Grid density was specified to be finer than 2 mm isotropic to ensure precision. The simulation was executed eight times with one channel transmitting at a time, and the input RF power was normalized to 1 Watt. The simulations were carried out on a Linux server equipped with dual high-performance GPUs (Tesla C2070, NVIDIA).

The simulated B_1 field at 298 MHz from each transmit RF channel was exported to MATLAB and re-gridded using cubic splines onto an isotropic 1 mm grid. Relative B_1 was calculated by combining the B_1 magnitude of each channel and the relative phase with respect to the reference channel. Complex white Gaussian noise was added to the

relative B_1 maps to simulate various SNR levels. 100 sets of noisy data were obtained for a Monte-Carlo test.

5.3.2 Phantom Preparation

Agar solution containing deionized water, agar, NaCl, and $NiCl_2 \cdot 6H_2O$ with mass ratio of 1000:9.0:1.12:0.5 was boiled, naturally cooled down to 45 ℃ while remaining in liquid state, and poured into a 125-mm-high and 65-mm-wide cylindrical container. The EPs were measured as σ = 0.30 S/m, ε_r = 79ε_0 using a dielectric probe described in a later section. Anomaly solutions with various EPs were prepared by doping deionized water with NaCl and polyvinylpyrrolidone (PVP). Glass capillary tubes and plastic straws with various diameters (from 1.5 mm to 11 mm) were filled with solutions of various EPs and inserted into the agar gel. The whole phantom was left to solidify in room temperature (22 ℃) for 24 hours. Samples from all solutions were taken and their EPs measured using the dielectric probe.

5.3.3 MRI Methods

The experiments were conducted in a human whole-body 7 Tesla MRI system (Siemens, Erlangen, Germany) equipped with 16 × 1 kW RF amplifiers (Communication Power Corporation, Hauppauge, NY, USA). The amplifiers were driven by a phase/gain controller remotely operated by a software toolbox developed in-house based on MATLAB (Van de Moortele et al., 2005; Metzger et al., 2008). The sample under test was positioned in the center of a dedicated 8-channel RF transceiver coil array,

comprised of eight 100-mm-long and 12-mm-wide striplines azimuthally distributed on a 100-mm-diameter cylindrical surface (Liu et al., 2017a). Each coil element was connected to a power source via a two-parameter tuning/matching capacitors network, which was adjusted before each experiment to minimized power reflection at the proton resonance frequency (297.2 MHz). Adjacent coil elements were de-coupled by a tunable capacitor so as to provide distinct B_1 distributions. The coil was then connected to the MRI system via a custom transmit/receive switch box.

A hybrid B_1 mapping method was used to retrieve the relative B_1, which combines (i) a reference scan based on 3D actual flip-angle imaging (AFI) (Yarnykh, 2007) with all channels transmitting together in large-flip-angle regime, and (ii) a series of multi-slice gradient echo (GRE) images in small-flip-angle regime pulsing through each channel sequentially. AFI parameters are FA = 60 °, TR = 120/20 ms, TE = 3.23 ms, voxel size 1.0 × 1.0 × 2.0 mm^3, spatial coverage 256 × 168 × 96 mm^3, duration 12.4 min; GRE parameters are FA = 15 °, TR = 126 ms, TE = 3.3 ms, in-plane resolution 1.0 × 1.0 mm^2, FOV 256 × 168 mm^2, 12 slices, 2 mm slice thickness, 8 averages, total duration 28.3 min.

T1w images in resolution of 0.5 × 0.5 × 1.0 mm^3 were obtained by taking the ratio of images from a 3D magnetization prepared rapid acquisition gradient echo (3D-MPRAGE) sequence and a 3D small-flip angle gradient echo (GRE) sequence, so as to cancel out undesirable weightings such as transmit and receive B_1, T2*, and proton density (Van de Moortele et al., 2009). T2w images were based on a turbo spin echo (TSE) sequence in 0.25 × 0.25 × 0.5 mm^3 resolution, with shimmed B_1 in the tumor to maximize excitation homogeneity.

5.3.4 Animal Tumor Model

All animal procedures and care were approved by the University of Minnesota Institutional Animal Care and Use Committee (IACUC) in accordance with federally approved guidelines.

Metastatic human breast carcinoma cell line MDA-MB-435A used in this study is an ascites model of MDA-MB-435, which was derived at M.D. Anderson Cancer Center, Houston, TX, USA in 1976 from the pleural effusion of a 31-year-old female with metastatic, ductal adenocarcinoma of the breast (Cailleau et al., 1978). The cells were cultured in DMEM (Dulbecco's Modified Eagle Medium, with 584 ml/L L-Glutamine, 4500 mg/L D-Glucose and 110 mg/L sodium pyruvate), supplemented with 10% FBS (Fetal Bovine Serum), Pen Strep (100 U/ml penicillin and 100 μg/ml streptomycin) and 0.0675 μg/ml human insulin. MAT-B-III cell line was obtained from American Type Culture Collection (ATCC), where it was established from a transplantable rat ascites tumor derived from a solid mammary adenocarcinoma (Sherblom et al., 1980). The cells were cultured in McCoy's 5A Medium (ATCC), supplemented with 10% FBS and Pen Strep.

Both MDA-MB-435A and MAT-B-III cells were maintained in 37 ℃ and 5% CO_2, and were subcultured by applying 0.05% trypsin - 0.53 mM EDTA (Invitrogen) for 5 minutes to detach the cells when reaching 70% in flasks. Cells in log phase of growth (50%~60% confluent) were harvested for tumor inoculation. Cells were rinsed, centrifuged, and resuspended by PBS (phosphate-buffered saline) twice, into 2×10^7 cells/ml cell suspension.

Female nude rats (4~6 months, 200~250 g, NIH-Foxn1rnu, Charles River) were injected with 2~4 $\times 10^6$ MDA-MB-435A cells subcutaneously over the dorsal flanks near the hind limbs under general anaesthesia. Experiments were performed 4~8 weeks after tumor seeding when a tumor diameter of 10~25 mm was obtained. Female Fischer 344 rats (2~4 months, 180~250 g, SAS FISCH, Charles River) were injected with 3~6 $\times 10^6$ MAT B III cells in a similar position under general anaesthesia. Experiments were performed 10~20 days after tumor seeding when a tumor diameter of 10~25 mm was obtained.

5.3.5 Necrosis Introduction by Topical TNF-α Injection.

A total of 200 μL of TNF-bound colloidal gold (CYT-6091 from CytImmune, 100 μg TNF/ml) was injected at 4 locations spatially evenly distributed near the core of tumor. Compared to TNF-α solution, the nanoparticle-based CYT-6091 has the advantage of better tumor targeting and less systemic toxicity (Tamarkin et al., 2006). The control group received the same amount of injection, but with inactivated drug. Drug inactivation was achieved by exposing the CTY-6091 from the same batch to heat (60 °C for 10 minutes) at which TNF-α is irreversibly denatured (Narhi et al., 1996). Imaging was taken before the injection, and 24 hours after the injections.

5.3.6 In Vivo Experiments

Animal was initially anesthetized in an induction chamber with 5% isoflurane mixed with 70% medical air and 30% oxygen, then maintained during imaging via a nose cone

(Kent Scientific) at 1%~2% isoflurane. Animal heating was achieved by a heating pad during preparation and hot water surrounding the animal holder during MR imaging. The temperature of water flowing through tubing around the animal was controlled by a thermostat integrated with water bath circulator (NESLAB RTE 7, Thermo Scientific). The respiratory rate and body temperature were monitored by an MR-compatible small animal monitoring and gating system (SA Instruments) during the procedures. The animal was positioned to lie on its side with the implanted tumor facing upwards. The orientation and the central axial slices of the tumor were labeled using an extra-fine felt-tip marker. The skin area around the tumor was shaved, and ultrasound transmission gel (Aquasonic 100, Parker Lab. Inc.) was applied to form a layer of approximately 10 mm on top of the tumor. For terminal studies, the animal was euthanized by carbon dioxide inhalation after the scan.

5.3.7 EPs Reconstruction

Noisy simulation data and experimental data were smoothed using a low-pass Gaussian filter with a kernel size of $5 \times 5 \times 3$ pixels and standard deviation of $1.2 \times 1.2 \times 0.8$ pixels. The spatial Laplacian and gradient of relative B_1 were taken using a Savitzky-Golay filter with a kernel size of $5 \times 5 \times 3$. The pixel-wise inverse problem (Equ. 3.9) was solved in the least-squares sense in MATLAB using backslash operation.

For phantoms, target maps were generated from manual segmentation of pilot images followed by assignment to each patch the measured EP values obtained from the probe. During BIEPT reconstruction, EPs on the phantom boundary were given as prior

information based on probe measurement of the agar background (σ = 0.30 S/m, ε_r = $79\varepsilon_0$). For simulation and in vivo experiments, the "gel region" was contoured and assigned EP values based on probe measurement (σ = 0.28 S/m, ε_r = $77\varepsilon_0$). Then a connected ROI was contoured that contains the whole tumor, part of the gel region and muscle tissue. For *in vivo* data, bone and tendon pixels were carefully excluded due to unreliable B_1 measurement subsequent to inherently very weak MR signal.

The central optimization problem (Equ. 5.1) was generated for each 2-dimensional (2D) ROI and solved using CVX, a MATLAB compatible package for specifying and solving convex programs (Grant and Boyd, 2008). It takes approximately 3 seconds to solve for each axial slice on a desktop with 3.4 GHz GPU and 32 GB RAM. Conductivity and relative permittivity were then computed from θ as

$$\varepsilon_r = real(e^{\theta})/\varepsilon_0$$

$$\sigma = -imag(e^{\theta}) \cdot \omega$$

Single slice EP results were interpolated using cubic splines to yield an in-plane resolution of 0.5 × 0.5 mm^2. The reconstructed EPs inside ROI are shown in color maps overlapped onto structural MRI.

5.3.8 Dielectric Probe Measurement

Measurement was performed using Keysight 85070E dielectric probe kit connected to an E4991A network analyzer. The probe, shaped like a planar disk, has a diameter of 18 mm. Measurement of samples smaller than 20 mm is not recommended by the manufacturer due to compromised accuracy. Prior to measurement, the system was

calibrated with air, shorting block, and deionized water each time it was set up. Immediately after euthanasia of the animal, a central cut was performed to expose the maximum cross-section of the tumor, where the open-ended coaxial probe was positioned and held still for 5 seconds during one trial. Measurement was repeated 3~5 times for each sample.

5.3.9 Histology

Tumor samples were fixed in 10% buffered formalin (Sigma-Aldrich) for 48~72 hours, transferred into 70% Ethanol (Decon Labs). The samples were then embedded in paraffin, sectioned at 5 μm and stained with hematoxylin–eosin (H&E). 40× magnification images were obtained by a digital microscope (ScanScope XT digital slide scanner, Aperio). Histologic images were processed by Aperio ImageScope (Leica Biosystems).

5.4 Results

5.4.1 Phantom Validation Results

Reconstruction results of the resolution phantom are shown in Fig. 5.3. Compared to the target maps, the locations and shapes of the tube anomalies are faithfully reflected by the reconstructed EP images. The central profiles of the reconstructed tubes show successful preservation of the conductivity and permittivity contrasts in structures ≥ 3 mm. Stable plateaus can be observed for structures ≥ 7 mm.

Reconstructed EPs from the contrast phantom are shown and fitted to the target values in Fig. 5.4. A good correlation between the reconstructed and target EP values is observed from the imaging results as well as linear fitting results, with ≤ 5% conductivity error and ≤ 12% permittivity error across the physiologically relevant EP ranges (0.3 S/m $\leq \sigma \leq$ 1.6 S/m, $50\varepsilon_0 \leq \varepsilon_r \leq 80\varepsilon_0$). Conductivity imaging exhibits superior robustness to permittivity imaging, in the sense of image distortion and fitting accuracy. This phenomenon is consistent with previous studies (Voigt et al., 2011; Marques et al., 2014; Liu et al., 2015), and can be attributed to the relatively narrower dynamic range of permittivity compared to that of conductivity (Marques et al., 2014).

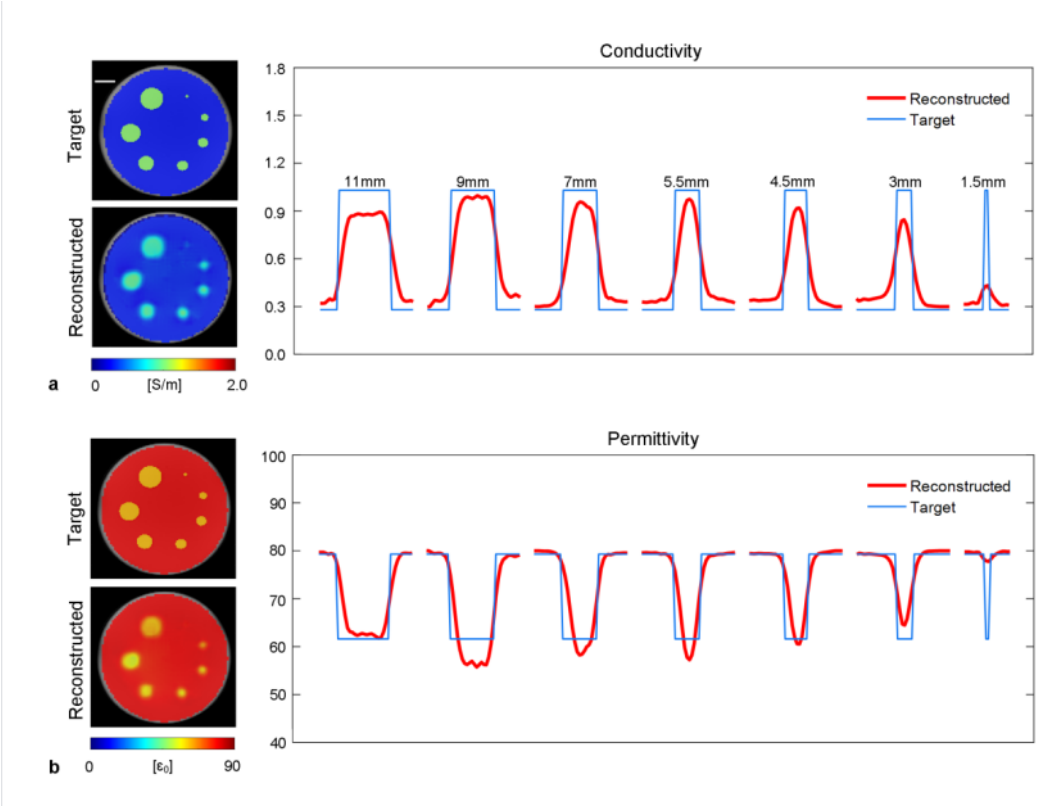

Figure 5.3 Reconstructed conductivity (a) and permittivity (b) from the resolution phantom containing 7 sample tubes of diameters from 1.5 mm to 11 mm filled with the

same liquid solution (σ = 1.02 S/m, ε_r = 61.6ε_0). The targeted and reconstructed EP images are shown to the left of the plots. The central profile of each tube is plotted (red) against the targeted ones (blue). Scale bar: 10 mm.

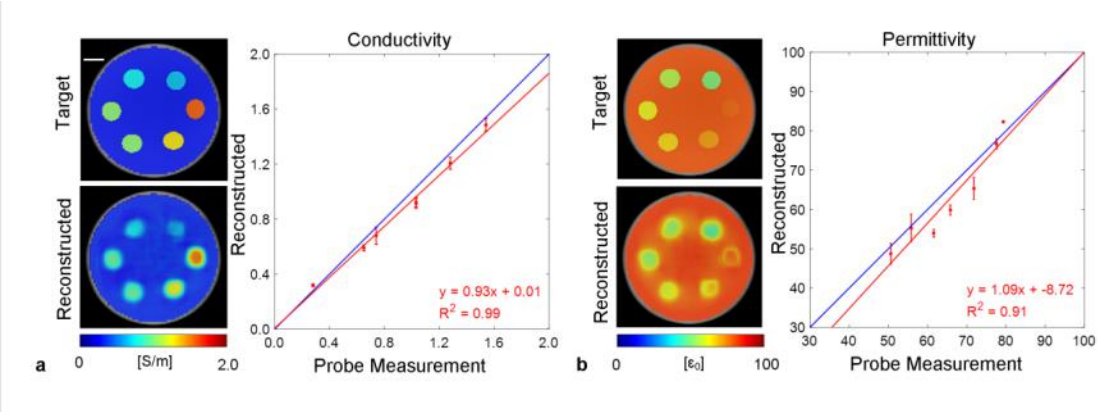

Figure 5.4 Reconstructed conductivity (a) and permittivity (b) from the contrast phantom containing 6 sample tubes of 9-mm diameter filled with different solutions spanning the EP ranges of interest. The targeted and reconstructed cross-section EP images are shown to the left of the plots. The reconstructed EPs inside each tube are shown as mean ± standard deviation, plotted and fitted against the dielectric probe measurement results. Scale bar: 10 mm.

5.4.2 Numerical Simulation Results

The simulation setup and single-channel absolute B_1 maps are shown in Fig. 5.5a. Relative B_1 maps were measured and used to calculate EPs. Reconstruction results from two SNR levels, 150 and 50, are shown in Fig. 5.5b. At both SNR levels, the simulated necrotic core with higher conductivity and permittivity can be clearly identified. The Monte-Carlo simulation of 100 trials demonstrates successful differentiation of EP differences among the three compartments on both noise levels, with less than 10% reconstruction error for both conductivity and permittivity. Nevertheless, contrast

differences among the three compartments are smaller, due to the smoothing effects of the de-noise filter, as well as contrast leakage effects from the spatial integration process.

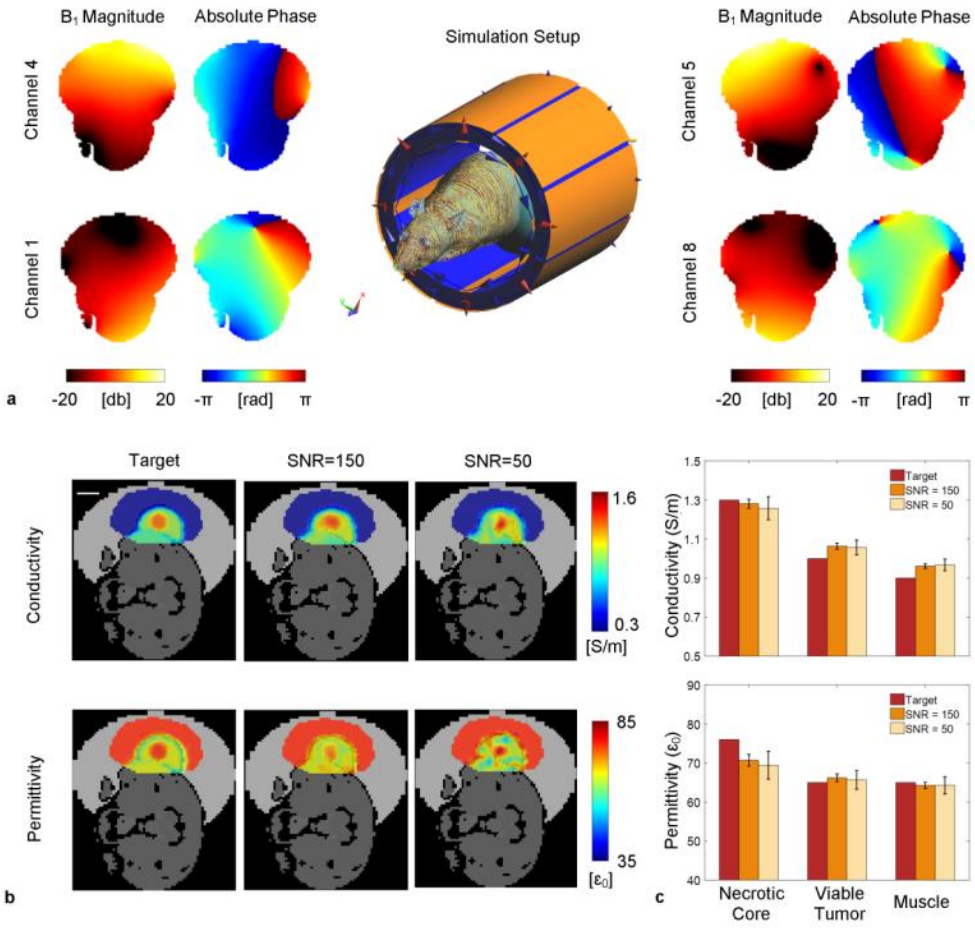

Figure 5.5 Numerical simulation of a realistic rat model. (a) Simulation setup and single channel B_1 distributions. (b) Comparison of the reconstructed EPs to the target maps using simulated relative B_1. Electrical conductivity and permittivity distributions are shown in color maps overlaid onto the grayscale sketch of the rat model. From left to right are the target maps and reconstruction results inside a manually drawn ROI with additive white Gaussian noise to adjust the SNR of the relative B_1 maps to 150 and 50, respectively. Scale bar: 10 mm. (c) The three bar groups correspond to the tumor necrotic core, viable tumor, and muscle, respectively. In each group, from left to right

shows the target EPs value and Monte Carlo simulation results from 100 trials at the corresponding SNR levels. The error bars show the standard deviation of the 100 mean values inside the corresponding region.

5.4.3 Animal Experiment Results

Bulk EP values obtained from BIEPT and the dielectric probe are plotted with respect to tumor volume in Fig. 5.6 for two xenograft models, MDA-MB-435 human breast cancer on athymic nude rats and MAT B III rat breast cancer on Fischer rats. BIEPT reports accurate average EP values within the size range of interest for both tumor models. The two tumor models give similar bulk EP values to each other; this is expected since both are derived from high-grade malignant cancer cell lines. Both the imaging and probe results show that bulk EPs are not significantly dependent on tumor size, which is consistent with previous finding in conductivity imaging of breast cancer patients (Shin et al., 2015). However, it can be observed that considerable EP variation resides in each imaging case, with standard deviation as large as 20% of the average values. These variations are less prominent in the values obtained from the physical probe measurements, which is expected since the latter report the bulk average of the entire tumor sample without spatial information, considering that the size of the physical probe is about the size of the tumor.

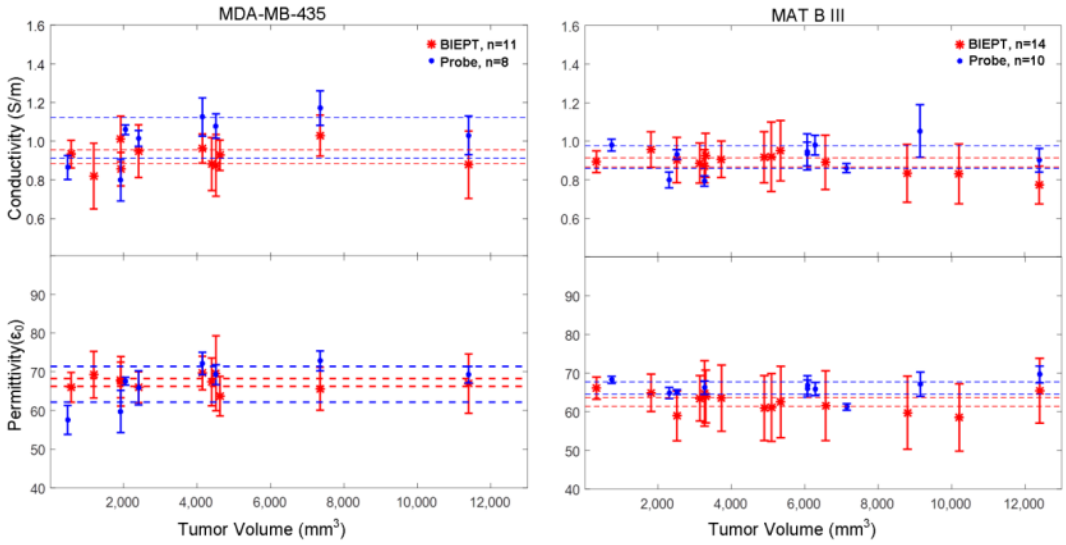

Figure 5.6 Comparison of *in vivo* imaging results and probe measurement results from the two rat models. Imaged (red) and probe measured (blue) EPs are plotted against tumor volume. For nude rats bearing an MDA-MB-435 tumor, the sample numbers are n = 11 and n = 8 for imaging and probe measurement, respectively. For Fischer rats bearing an MAT B III tumor, n = 14 and n = 10, respectively. Each data point represents one animal. For imaging, data are shown as mean ± standard deviation of tumor pixels in the central three axial slices. For probe, data are shown as mean ± standard deviation of four measurement trials on the central cut of tumor. The 95% confidence intervals of EPs are labelled by dashed lines regardless of tumor volume.

To demonstrate the capability of BIEPT to image tumor heterogeneity, we compare the reconstructed EP images with corresponding T1w, T2w images and whole-mount histopathology slides. Two representative cases from MDA-MB-435 human breast cancer are shown in Figs. 5.7 and 5.8, respectively.

In the first case, the necrotic cores indicated by purple and red arrows show opposite signal change on T1w and T2w images compared to solid tumor (Fig. 5.7a). It is known

that opposite T1w and T2w contrast variations can be observed within regions that are identified as necrotic in nature, due to two competing factors, paramagnetic ions and water content, with the former decreasing T1 and T2 and the latter increasing them (Jakobsen et al., 1995). Yet both factors synergistically contribute to locally increased conductivity, as shown as distinguished tumor sub-regions on the conductivity map. On the other hand, water content contributes to permittivity elevation while ion concentration has minimal effect on the latter, leading to the contrast between these sub-regions on the reconstructed permittivity map. The low-permittivity sub-regions may also be caused by accumulation of proteins in cell debris and formation of blood clots. Hematoxylin and eosin (H&E) stain confirms the presence of three coagulative necrotic areas (Fig. 5.7b). Tumor necrosis is defined as irreversible cell and nuclear changes such as karyolysis, vacuolization of the nucleus and/or cytoplasm, and dissolution of the membrane integrity. As a result of these morphologic changes, necrotic areas will appear as "pink" areas on H&E stain within the tissue that are readily conspicuous at lower magnification. A central cut was made through the tumor along the green dashed line, allowing for dielectric probe measurement of the bulk tumor EPs, found as 1.01 ± 0.04 S/m and $65.8\varepsilon_0 \pm 4.4\varepsilon_0$, comparable to the BIEPT reported EP values of 0.95 ± 0.14 S/m and $66.0\varepsilon_0 \pm 4.0\varepsilon_0$.

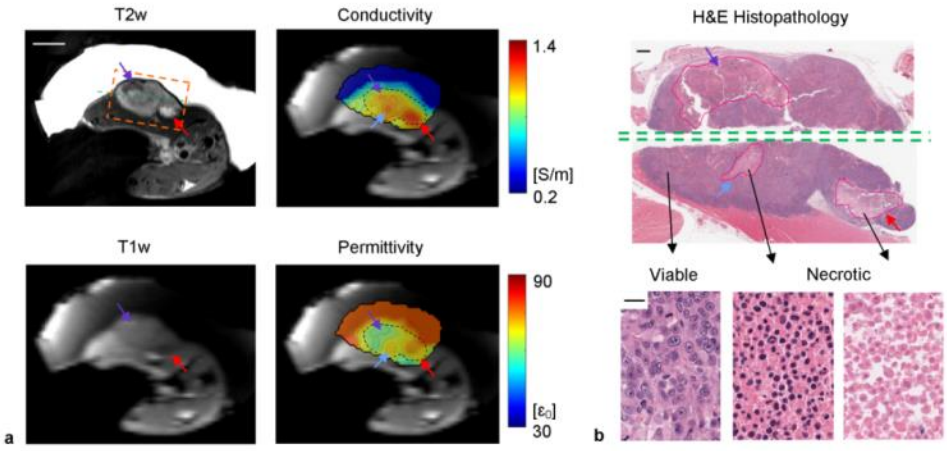

Figure 5.7 In vivo EP imaging of rat #1. (a) T1w, T2w, conductivity and permittivity maps. The black dashed contours on EP maps contour the tumor based on the T2w image. The orange dashed box shows the field of view of the histological slide in (b). The green dashed line shows the position where the tumor was cut through for probe measurement. Scale bar: 10 mm. (b) H&E histopathology of the same imaging slice in the orange dashed box as in (a). The necrotic cores were contoured by an experienced pathologist (E.R.). Examples of viable, necrotic, and highly necrotic tumor tissues are shown with distinct nuclear and cellular shape and density. Scale bars: 1 mm on whole-mount pathology and 20 μm on zoomed pathology.

In the second case, a large necrotic core appears in the second quartile of the tumor with two distinct areas showing clear contrast on T2w image (Fig. 5.8a, red and purple arrows). On T1w image, one area exhibits significant hypointensity (red arrow), while the other shows marginal hyperintensity (purple arrow). Nevertheless, both of these two areas show conductivity increase while discrepancy in permittivity is preserved. The H&E slide shows more than 80% necrosis with massive karyolysis and cell membrane loss in the left sub-region (Fig. 5.8b, purple arrow). Neutrophil and fibroblast infiltration

is observed that removes water from tissue, in keeping with the underlying process of healing and scar formation, which may contribute to relatively low free water content. Fig. 5.8a also shows successful detection of two 2-mm necrotic cores with elevated EPs, labeled by blue arrows, while their contrast on T1w and T2w images are less discernable. These two necrotic cores merge as a single hot spot on EP images due to the inherent smoothing properties of the reconstruction process. Probe measurement of the tumor reported 1.12 ± 0.10 S/m and $72.1\varepsilon_0 \pm 2.9\varepsilon_0$, comparable to the BIEPT measured EP values as 0.96 ± 0.08 S/m and $71.0\varepsilon_0 \pm 4.3\varepsilon_0$.

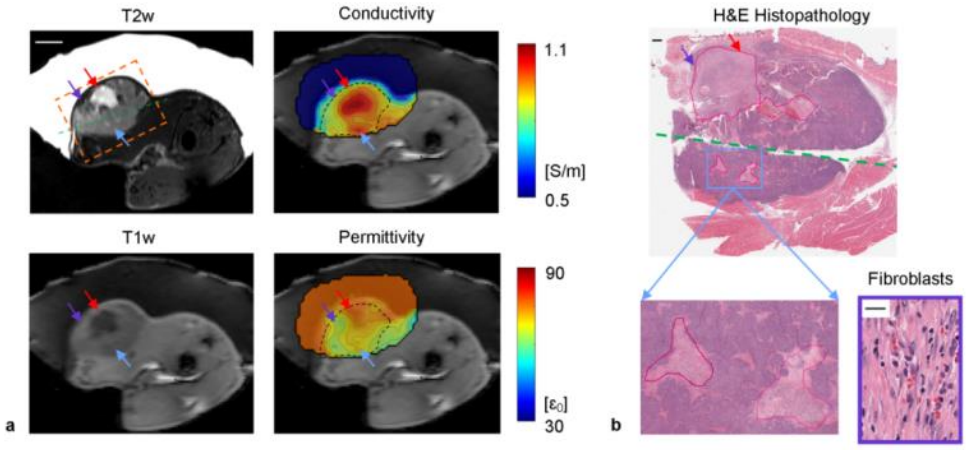

Figure 5.8 In vivo EP imaging of rat #2. Figure layout and annotations are same as in Fig. 5.7. The fibroblasts shown are taken from the necrotic core labeled by the purple arrow. Scale bars: 10 mm on MRI, 1 mm on whole-mount pathology and 20 μm on zoomed pathology.

To evaluate the dynamics of EPs during tumor development, a longitudinal study was performed to monitor tumor growth in a 1.5-month time window (Fig. 5.9). The

tumor initially appears homogeneous on both structural MR images and EPs. Local features started to emerge after one month, with a notable sub-region in the third quadrant of the tumor showing hypointensity on T1w and hyperintensity on T2w. This sub-region could be clearly identified with high conductivity compared to the other part of the tumor from day 30 to day 44, while its permittivity was higher on day 30 and fell to a lower level on day 37. This trend of EP changes can potentially be explained by edema formation shortly after the development of necrosis, which gradually subsides with the space occupied by cell debris, while electrolyte concentration monotonically increases throughout the time window (Jakobsen et al., 1995; Belfi et al., 1991).

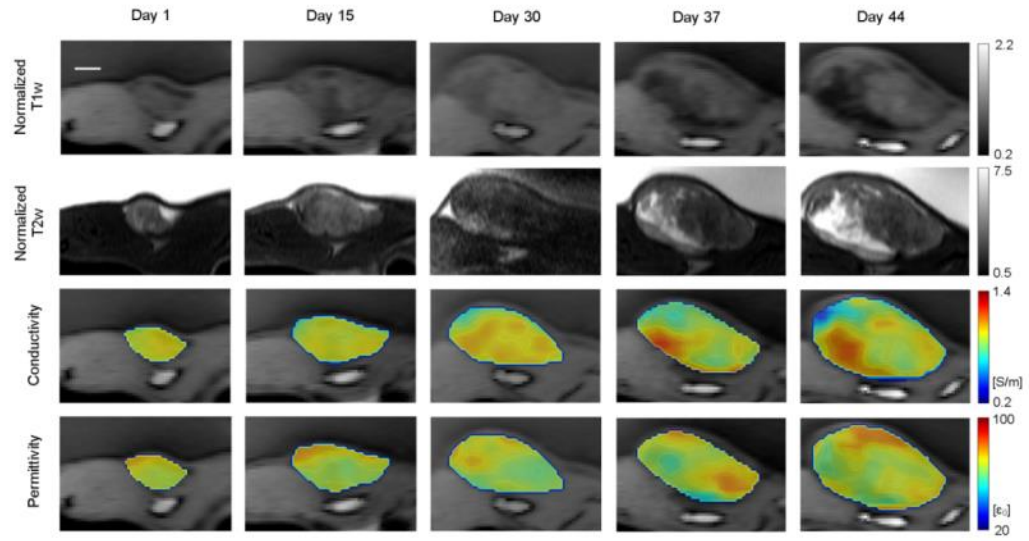

Figure 5.9 Longitudinal monitoring of a malignant human breast tumor in rat. MRI performed at five checkpoints as labeled on top of the images. From top to bottom: Normalized (to muscle) T1w images, normalized T2w images, quantitative conductivity and permittivity of tumor in color map overlaid on the T1w image. The animal was positioned similarly for all scans, and the axial slice with the largest tumor cross-section

is shown in this figure. Images of the same contrast share the same colorbar. All images share the same scale bar shown on the top left, which is 5 mm.

After showing that spontaneous tumor necrosis correlates with changes of local EPs while their bulk averages stay relatively stable, we further explore how EPs are altered by *induced* necrosis, in order to mimic conditions of effective chemical or radiation therapy. The experiment was designed based on loco-regional administration of Tumor Necrosis Factor-alpha (TNF-α) into the core of MAT B III tumors on Fischer rats. TNF-α has a well-documented anti-tumor effect (Horssen et al., 2006), causing evident hemorrhagic necrosis within 24 hours (Manusama et al., 1996).

In a representative case shown in Fig. 5.10a, spontaneous tumor heterogeneity has already taken shape by the time of treatment initiation, with contrast between a central necrosis and solid tumor clearly seen on the T2w and the EP images. At 24 hours after the treatment, the tumor shows hypointensity on the T1w image and hyperintensity on the T2w image in the central spontaneous necrosis (orange arrow), but no significant change is observed in the solid part of the tumor (green arrow). In contrast, significant focal conductivity increase is observed in both the spontaneous necrosis and the solid tumor. Focal permittivity elevation is less apparent and confined to a smaller region, indicating a minimal change of the underlying molecular compositions. Despite the differential intra-tumor EP patterns before and after the local treatment, changes of the bulk mean conductivity and permittivity are small (Fig. 5.10b), which are arguably much more challenging to capture considering the sensitivity of current EPT approaches, and do not

provide localized information. Therefore, local EP values, especially conductivity, are sensitive biomarkers for the early detection of partial treatment response.

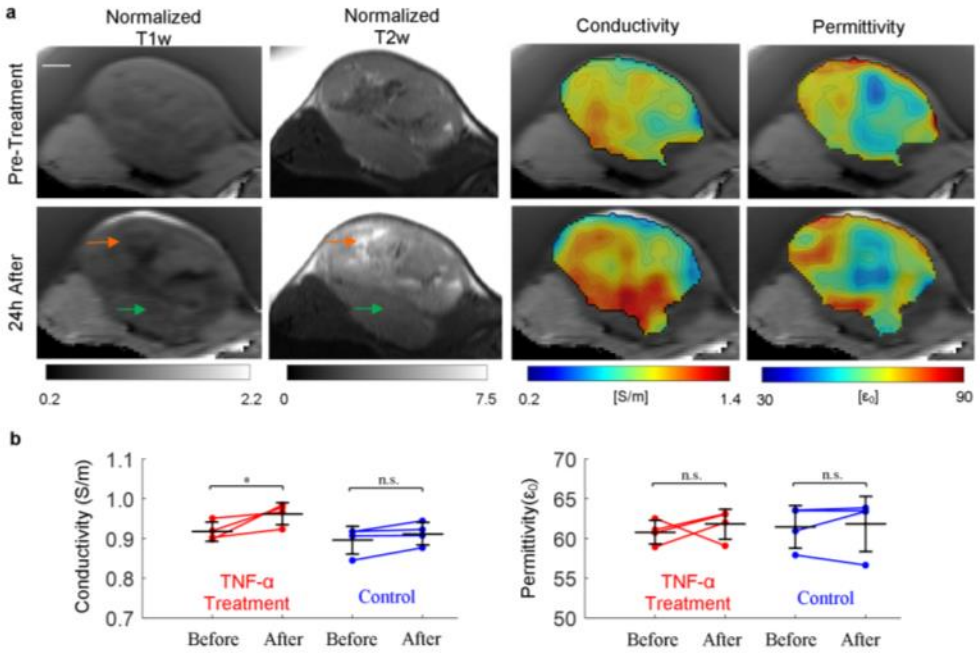

Figure 5.10 Tumor EPs response to topical TNF-α intervention. MRI scans were performed on tumor-bearing rats, and the same rats 24 hours after the drug injection. (a) Representative T1w, T2w, conductivity and permittivity images before and 24 hours after an effective treatment. The orange and green arrows show signal changes in the spontaneous tumor necrosis and the viable tumor after the treatment, respectively. (b) Changes in the bulk averages of conductivity and permittivity before and 24 hours after the treatment. n = 4 for the effective TNF-α intervention group and n = 4 for the control group. The 95% confidence interval of conductivity change is 0 to 0.09 S/m with P = 0.048, and that of permittivity is -1.98ε_0 to 3.96ε_0 with P = 0.44 . *P < 0.05; n.s. not significant. Scale bar: 5 mm.

5.5 Discussions

In this chapter, we propose a Boundary Informed Electrical Properties Tomography (BIEPT) technique for high-resolution electrical conductivity and permittivity mapping from a boundary reference area and EPs' Wirtinger derivative computed using a plural of relative transmit B_1 measurements from a 7 Tesla MRI system, with enhanced numerical stability from edge sparsity regularization. This method does not require physical flipping of the imaging setup or image registration of multiple datasets, thus representing a more general methodology compared to gEPT in the context of multi-transmission. Simulation and phantom results demonstrated its high accuracy across physiologically relevant EP ranges and sensitivity to anomalies as small as 3 mm, under varied noisy conditions. In vivo tumor imaging experiments were performed on eleven rats with human breast cancer xenograft, referenced to externally applied ultrasound gel. We observed association of local conductivity elevation with tumor necrosis. We also noticed potential correlation of permittivity with additional tumor pathological characteristics such as healing and scar formation, yet the confidence level of permittivity is lower due to its susceptibility to image distortions and noise. Nevertheless, combination of the spatial distributions of both may give rise to a useful biomarker in clinical settings, such as tumor staging and treatment evaluation.

Previous human cancer studies based on either an invasive probe or non-invasive MREPT approaches have reported differences in mean EP values between benign and malignant tissues (Joines et al., 1994; Kim et al., 2016; Balidemaj et al., 2016), tumors of low and high grades (Tha et al., 2018), as well as tumors in early and late stages (Swarup

et al., 1991). Despite the established correlation between EPs and those clinically meaningful tumor classifications, the underlying contrast mechanism and tumor biology remain unclear, partially due to the limited spatial resolution of the previous approaches and the practice of evaluating bulk EPs across large tumors (> 20 mm). To address this pivotal question, we developed BIEPT to retrieve high-resolution EP images from an animal tumor model in vivo. The observed association of EP changes with tumor necrosis may provide an explanation for the previously reported EP deviations in late-stage, high-grade, malignant tumors. Moreover, local feature identification and heterogeneity quantification of EPs derived from high-resolution image modality are potentially more sensitive biomarkers than bulk mean EPs in terms of tumor characterization (O'Connor et al., 2015; Swanton, 2012).

Successful detection of both spontaneous and induced tumor necrosis is expected to have impacts on clinical practice. Spontaneous necrosis is often observed in highly invasive tumors with aggressive proliferation, due to multiple factors including deficiency of local blood perfusion that disrupts pH equilibrium, oxygen and nutrient supply, as well as removal of metabolic wastes (Weinberg, 2013). Necrotic tumors secrete stimulatory chemokines and cytokines which in turn facilitate tumor growth and infiltration (Vakkila and Lotze, 2004; Proskuryakov and Gabai, 2010). In practice, excessive necrosis is a feature of aggressive tumors with unfavorable prognosis in terms of early recurrence and mortality (Barker et al., 1996; Gilchrist et al., 1993), and necrotic tumors are found to be more resistant to many types of chemotherapy as well as radiation therapy (Sutherland et al., 1988). Therefore, mapping the geometry and EPs of tumor

necrosis can potentially provide valuable information to help guide clinical decisions and optimize individualized treatment plan. On the other hand, many successful cancer therapies, including chemo- and radiation-therapy approaches, induce intra-tumor necrosis when they are effective, and this typically takes place well before substantial changes in tumor volumetric numbers. Therefore, imaging tumor necrosis may provide not only early feedback on the effectiveness of the administered therapy but also partial response alerts. The proposed EPs based necrosis imaging technique is based on endogenous tissue contrast, representing a new avenue to be explored for monitoring early therapeutic response as well as a suboptimal therapy.

Based on our current findings about tumor necrosis, more investigations are warranted to explore the association of EP changes with other tumor signatures, such as angiogenesis and hypoxia, as well as tumor response to treatment. These biological effects typically happen on a much smaller spatial scale compared to necrosis, and they are expected to have more subtle impacts on EPs. Therefore, detection of these effects may have a better chance on dedicated animal scanners with higher gradient power for spatial encoding and higher magnetic field for improved SNR (Budinger et al., 2016; Lee et al., 2015). In addition, animal tumor imaging in situ, i.e. in its original site, should be explored for an improved modeling of tumor behavior, as well as patient studies to evaluate EPs as clinically meaningful biomarkers.

In this initial study, the implementation of BIEPT still presents some limitations that can be addressed in future work. First of all, the current multi-channel B_1 mapping technique requires about one hour of acquisition time to produce $1.0 \times 1.0 \times 2.0$ mm^3

maps in 8 channels with satisfactory SNR. While providing high quality B_1 maps in multi-channel arrays, the hybrid B_1 mapping method utilized in this work has not been specifically optimized for time efficiency; alternative B_1 mapping methods recently proposed, such as Bloch-Siegert method (Sacolick et al., 2011), DREAM (Nehrke and Börnert, 2012), Large Dynamic Range B_1 mapping (Padormo et al., 2016), could be implemented for comparison. Furthermore, high count of receive channels positioned close to the imaged body could also be employed additionally to a transmit array to improve SNR, instead of a transceiver array which has inherently compromised receive performance compared with receive-only arrays. Another limitation in the current study stems from the fact that BIEPT is tested in a regularly shaped, simply-connected ROI, which serves our purpose well to image a tumor xenograft surrounded by water-based gel. In cases where the ROI is irregularly shaped or has cavities, e.g. imaging near the bone or in the bowel, the robustness of BIEPT needs to be addressed. It is expected that prior knowledge about the average EPs of the imaging area and regularization methods will be helpful in those situations. BIEPT also requires an external reference area to infer the underlying EPs of a tumor, which would not be practical in most clinical settings. Nevertheless, EPs of normal body tissues have been well characterized, including some that have relatively large area of reasonable homogeneity (e.g. muscle, liver, etc), and may be used as reference to BIEPT when a target tumor is contiguous to them. EP values of these normal tissues can be either extracted from the widely used literature by Gabriel et al. based on *ex vivo* measurements (S. Gabriel et al., 1996), or calculated *in vivo* using B_1 based on the Helmholtz equation.

5.6 Conclusion

We conclude that tumor EPs heterogeneity can be inferred by the proposed boundary informed electrical properties tomography (BIEPT) technique based on unique transmit B_1 images measured from a multi-channel RF coil, using an external reference region and image edge sparsity constraint. Similar spatial patters amongst tumor EP distributions, anatomical T1w and T2w images and pathology have been observed in animal experiments. Association of altered local EP values with tumor necrosis has been reported. Further investigations will be dedicated to improving and generalizing BIEPT for identification of EPs-related pathological features, as well as their evaluation as biomarkers in cancer patient care.

Chapter 6 - Summary and Future Directions

Electrical properties (EPs) of biological tissues have various applications such as diagnosis of diseases as unique biomarkers, and construction of numerical models for electromagnetic simulations to predict distribution and effects of EM field. Electrical Properties Tomography (EPT) is a technology that utilizes Magnetic Resonance Imaging (MRI) to noninvasively retrieve tissue conductivity and permittivity by fitting the radiofrequency magnetic field (B_1 field) to Maxwell's equations. A plurality of B_1 field measurements helps to alleviate the severe under-determined-ness faced by conventional single-channel EPT approaches.

This thesis aims to retrieve objective and accurate tissue EPs *in vivo* with multiple transmit B_1 maps, incorporating image sparsity and a priori information such as external boundary information. The targeted applications are human brain imaging and cancer animal model imaging. The key contributions of this dissertation are:

- Extension of the current state-of-the-art gradient based EPT (gEPT) using multi-channel transceiver arrays to automatically select integration seeds based on the Helmholtz equation. Consistent *in vivo* imaging results have been obtained in a cohort of 12 subjects, which are close but not equal to previous literature values based on *ex vivo* measurements.
- Development of CONtrast Conformed EPT (CONCEPT) technology that employs only transmit B_1 maps to retrieve EPs of the brain. Intermediate quantitative EP gradient is used to inform EP reconstruction using discriminated L_1 and L_2 norm regularization. The central optimization problem is efficiently solved using Alternating Direction Method of Multipliers (ADMM) developed in

house. Numerical simulations and phantom experiment at 7 T are performed to quantify its performance.

- Development of Boundary Informed EPT (BIEPT) technology that employs only transmit B_1 maps from one experimental setup to retrieve EPs of tumor xenograft on rat *in vivo*. BIEPT takes advantage of external references and image sparsity to achieve enhanced stability and accuracy. It is validated through numerical simulations and phantom experiments at 7 T.
- *In vivo* imaging of 25 tumor xenografts on rat using BIEPT. The results show severe heterogeneity inside a tumor, demonstrate strong association of elevated conductivity with tumor necrosis, and indicate potential capability of permittivity to provide secondary information about tumor pathological features. Longitudinal monitoring of tumor growth and detection of treatment response using EPs have also been explored.

Future directions for the development of multi-transmission-based MREPT are suggested as follows. This list is far from exhaustive, given the highly interdisciplinary nature of the technology and the complex science behind it.

- Innovation in reconstruction theory, potentially using scattering field. The B_1 field of the empty loaded RF coil obtained from numerical simulation, or the B_1 field measured when using a phantom with known EPs, can be used to infer the unknown EPs of the object under detection by comparing the resultant change in B_1. Extraction of EPs can be done by either solving the physical equations or using machine learning methods.
- Advances of B_1 mapping methods to achieve fast, 3D, accurate and high-resolution B_1 maps from multiple RF channels. Nevertheless, it is expected that compromises need to be made to achieve a balance among these key performance indices. It would also be desirable to integrate B_1 reconstruction with EP reconstruction to be able to retrieve EPs from MR signals directly,

resulting in “EPT sequences”. Sensitivity of EPs to motion and physiological effects during the MRI scan should also be addressed during data acquisition.

- Incorporation of nonlinear de-noising strategy based on singular value decomposition (SVD) or Total Generalized Variation (TGV). EPT aims to retrieve high-spatial-frequency EP distribution from B_1 maps that are rich in low-spatial-frequency components. This process amplifies noise significantly. Therefore, novel strategies to suppress noise propagation are critical to accurate and robust EPT results.
- Automated selection of the regularization parameters. The regularization parameters can substantially affect reconstruction results if they are far away from the optimal values. Automation of parameter selection can eliminate the tedious process of fine-tuning, and further reduce subjectivity in the reconstructed results.
- Applications using RF coils with high-count receive channels. Since the reconstruction is no longer dependent on the symmetry between transmit and receive B_1, generic coils with high-count receive elements should be used to gain higher SNR in the raw MR data.

References

Adriany, G., Van de Moortele, P.-F., Ritter, J., Moeller, S., Auerbach, E.J., Akgün, C., Snyder, C.J., Vaughan, T., Uğurbil, K., 2008. A geometrically adjustable 16-channel transmit/receive transmission line array for improved RF efficiency and parallel imaging performance at 7 Tesla. Magn. Reson. Med. 59, 590–597. https://doi.org/10.1002/mrm.21488

Aerts, H.J.W.L., Velazquez, E.R., Leijenaar, R.T.H., Parmar, C., Grossmann, P., Carvalho, S., Bussink, J., Monshouwer, R., Haibe-Kains, B., Rietveld, D., Hoebers, F., Rietbergen, M.M., Leemans, C.R., Dekker, A., Quackenbush, J., Gillies, R.J., Lambin, P., 2014. Decoding tumour phenotype by noninvasive imaging using a quantitative radiomics approach. Nat. Commun. 5, 5006. https://doi.org/10.1038/ncomms5006

Akçakaya, M., Nam, S., Basha, T.A., Kawaji, K., Tarokh, V., Nezafat, R., 2014. An Augmented Lagrangian Based Compressed Sensing Reconstruction for Non-Cartesian Magnetic Resonance Imaging without Gridding and Regridding at Every Iteration. PLoS ONE 9, e107107. https://doi.org/10.1371/journal.pone.0107107

Asslander, J., Cloos, M.A., Knoll, F., Sodickson, D.K., Hennig, J., Lattanzi, R., 2018. Low rank alternating direction method of multipliers reconstruction for MR fingerprinting. Magn. Reson. Med. 79, 83–96. https://doi.org/10.1002/mrm.26639

Balidemaj, E., Boer, P. de, Lier, A.L.H.M.W. van, Remis, R.F., Stalpers, L.J.A., Westerveld, G.H., Nederveen, A.J., Berg, C.A.T. van den, Crezee, J., 2016. In vivo electric conductivity of cervical cancer patients based on B1+ maps at 3T MRI. Phys. Med. Biol. 61, 1596. https://doi.org/10.1088/0031-9155/61/4/1596

Balidemaj, E., van den Berg, C., Trinks, J., Lier, A., Nederveen, A., Stalpers, L., Crezee, H., Remis, R., 2015a. CSI-EPT: A Contrast Source Inversion Approach for Improved MRI-Based Electric Properties Tomography. IEEE Trans. Med. Imaging 34, 1788–1796. https://doi.org/10.1109/TMI.2015.2404944

Balidemaj, E., van Lier, A.L.H.M.W., Crezee, H., Nederveen, A.J., Stalpers, L.J.A., van den Berg, C.A.T., 2015b. Feasibility of Electric Property Tomography of pelvic tumors at 3T. Magn. Reson. Med. 73, 1505–1513. https://doi.org/10.1002/mrm.25276

Barker, F.G., Davis, R.L., Chang, S.M., Prados, M.D., 1996. Necrosis as a prognostic factor in glioblastoma multiforme. Cancer 77, 1161–1166. https://doi.org/10.1002/(SICI)1097-0142(19960315)77:6<1161::AID-CNCR24>3.0.CO;2-Z

Belfi, C.A., Medendorp, S.V., Ngo, F.Q.H., 1991. The response of the KHT sarcoma to radiotherapy as measured by water proton NMR relaxation times: relationships with

tumor volume and water content. Int. J. Radiat. Oncol. 20, 497–507. https://doi.org/10.1016/0360-3016(91)90062-9

Boyd, S., Parikh, N., Chu, E., Peleato, B., Eckstein, J., 2011. Distributed Optimization and Statistical Learning via the Alternating Direction Method of Multipliers. Found Trends Mach Learn 3, 1–122. https://doi.org/10.1561/2200000016

Brink, W.M., Börnert, P., Nehrke, K., Webb, A.G., 2014. Ventricular B1+ perturbation at 7 T – real effect or measurement artifact? NMR Biomed. 27, 617–620. https://doi.org/10.1002/nbm.3112

Buchenau, S., Haas, M., Splitthoff, D.N., Hennig, J., Zaitsev, M., 2013. Iterative separation of transmit and receive phase contributions and B 1 + -based estimation of the specific absorption rate for transmit arrays. Magn. Reson. Mater. Phys. Biol. Med. 1–14. https://doi.org/10.1007/s10334-013-0367-6

Budinger, T.F., Bird, M.D., Frydman, L., Long, J.R., Mareci, T.H., Rooney, W.D., Rosen, B., Schenck, J.F., Schepkin, V.D., Sherry, A.D., Sodickson, D.K., Springer, C.S., Thulborn, K.R., Uğurbil, K., Wald, L.L., 2016. Toward 20 T magnetic resonance for human brain studies: opportunities for discovery and neuroscience rationale. Magn. Reson. Mater. Phys. Biol. Med. 29, 617–639. https://doi.org/10.1007/s10334-016-0561-4

Bulumulla, S., Roberts, J., Lee, S.-K., Lamb, P., Hancu, I., 2014. Reference aided imaging of rat tumor dielectric properties at 3.0T. Milan, Italy, p. 3193.

Cailleau, R., Olivé, M., Cruciger, Q.V.J., 1978. Long-term human breast carcinoma cell lines of metastatic origin: Preliminary characterization. In Vitro 14, 911–915. https://doi.org/10.1007/BF02616120

CDC - Cancer Among Women [WWW Document], 2017. URL http://www.cdc.gov/cancer/dcpc/data/women.htm.

Christ, A., Kainz, W., Hahn, E.G., Honegger, K., Zefferer, M., Neufeld, E., Rascher, W., Janka, R., Bautz, W., Chen, J., Kiefer, B., Schmitt, P., Hollenbach, H.-P., Shen, J., Oberle, M., Szczerba, D., Kam, A., Guag, J.W., Kuster, N., 2010. The Virtual Family--development of surface-based anatomical models of two adults and two children for dosimetric simulations. Phys. Med. Biol. 55, N23-38. https://doi.org/10.1088/0031-9155/55/2/N01

Collins, C.M., Li, S., Smith, M.B., 1998. SAR and B1 field distributions in a heterogeneous human head model within a birdcage coil. Magn. Reson. Med. 40, 847–856. https://doi.org/10.1002/mrm.1910400610

Collins, C.M., Liu, W., Wang, J., Gruetter, R., Vaughan, J.T., Ugurbil, K., Smith, M.B., 2004. Temperature and SAR calculations for a human head within volume and surface coils at 64 and 300 MHz. J. Magn. Reson. Imaging 19, 650–656. https://doi.org/10.1002/jmri.20041

Corthout, E., Barker, A., Cowey, A., 2001. Transcranial magnetic stimulation. Exp. Brain Res. 141, 128–132. https://doi.org/10.1007/s002210100860

Cunningham, C.H., Pauly, J.M., Nayak, K.S., 2006. Saturated double-angle method for rapid B1+ mapping. Magn. Reson. Med. 55, 1326–1333. https://doi.org/10.1002/mrm.20896

Duan, Q., van Gelderen, P., Duyn, J., 2013. Improved Bloch-Siegert based B1 mapping by reducing off-resonance shift. NMR Biomed. 26, 1070–1078. https://doi.org/10.1002/nbm.2920

Duan, S., Xu, C., Deng, G., Wang, J., Liu, F., Xin, S.X., 2016. Quantitative analysis of the reconstruction errors of the currently popular algorithm of magnetic resonance electrical property tomography at the interfaces of adjacent tissues. NMR Biomed. 29, 744–750. https://doi.org/10.1002/nbm.3522

Fass, L., 2008. Imaging and cancer: A review. Mol. Oncol. 2, 115–152. https://doi.org/10.1016/j.molonc.2008.04.001

Fear, E.C., Li, X., Hagness, S.C., Stuchly, M.A., 2002. Confocal microwave imaging for breast cancer detection: localization of tumors in three dimensions. IEEE Trans. Biomed. Eng. 49, 812–822. https://doi.org/10.1109/TBME.2002.800759

Freitag, E., Busam, R., 2006. Complex Analysis. Springer Science & Business Media.

Gabriel, C., Gabriel, S., Corthout, E., 1996. The dielectric properties of biological tissues: I. Literature survey. Phys. Med. Biol. 41, 2231–2249. https://doi.org/10.1088/0031-9155/41/11/001

Gabriel, S, Lau, R.W., Gabriel, C., 1996. The dielectric properties of biological tissues: II. Measurements in the frequency range 10 Hz to 20 GHz. Phys. Med. Biol. 41, 2251–2269. https://doi.org/10.1088/0031-9155/41/11/002

Gabriel, S., Lau, R.W., Gabriel, C., 1996. The dielectric properties of biological tissues: III. Parametric models for the dielectric spectrum of tissues. Phys. Med. Biol. 41, 2271–2293. https://doi.org/10.1088/0031-9155/41/11/003

Gatenby, R.A., Grove, O., Gillies, R.J., 2013. Quantitative imaging in cancer evolution and ecology. Radiology 269, 8–14. https://doi.org/10.1148/radiol.13122697

Gilchrist, K.W., Gray, R., Fowble, B., Tormey, D.C., Taylor, S.G., 1993. Tumor necrosis is a prognostic predictor for early recurrence and death in lymph node-positive breast cancer: a 10-year follow-up study of 728 eastern cooperative oncology group patients. J. Clin. Oncol. 11, 1929–1935.

Gillies, R.J., Kinahan, P.E., Hricak, H., 2015. Radiomics: images are more than pictures, they are data. Radiology 278, 563–577. https://doi.org/10.1148/radiol.2015151169

Grant, M.C., Boyd, S.P., 2008. Graph implementations for nonsmooth convex programs, in: Recent Advances in Learning and Control. Springer, London, pp. 95–110.

Griswold, M.A., Jakob, P.M., Heidemann, R.M., Nittka, M., Jellus, V., Wang, J., Kiefer, B., Haase, A., 2002. Generalized autocalibrating partially parallel acquisitions (GRAPPA). Magn. Reson. Med. 47, 1202–1210. https://doi.org/10.1002/mrm.10171

Gurler, N., Ider, Y.Z., 2017. Gradient-based electrical conductivity imaging using MR phase. Magn. Reson. Med. 77, 137–150. https://doi.org/10.1002/mrm.26097

Gurler, N., Oran, O.F., Keklikoglu, H.D., Ider, Y.Z., 2016. Application of Generalized Phase based Electrical Conductivity Imaging in the Subacute Stage of Hemorrhagic and Ischemic Strokes, in: Proceedings of the 25th Annual Meeting of ISMRM. Singapore, p. 2994.

Haacke, E.M., Petropoulos, L.S., Nilges, E.W., Wu, D.H., 1991. Extraction of conductivity and permittivity using magnetic resonance imaging. Phys. Med. Biol. 36, 723–734. https://doi.org/10.1088/0031-9155/36/6/002

Hafalir, F.S., Oran, O.F., Gurler, N., Ider, Y.Z., 2014. Convection-Reaction Equation Based Magnetic Resonance Electrical Properties Tomography (cr-MREPT). IEEE Trans. Med. Imaging 33, 777–793. https://doi.org/10.1109/TMI.2013.2296715

Hansen, P.C., Danmarks Tekniske Universitet, Institut for Matematisk Modellering, 1999. The L-curve and its use in the numerical treatment of inverse problems. IMM, Department of Mathematical Modelling, Technical Universityof Denmark, Lyngby.

He, B., Sohrabpour, A., Brown, E., Liu, Z., 2018. Electrophysiological Source Imaging: A Noninvasive Window to Brain Dynamics. Annu. Rev. Biomed. Eng. https://doi.org/10.1146/annurev-bioeng-062117-120853

Horssen, R. van, Hagen, T.L.M. ten, Eggermont, A.M.M., 2006. TNF-α in cancer treatment: molecular insights, antitumor effects, and clinical utility. The Oncologist 11, 397–408. https://doi.org/10.1634/theoncologist.11-4-397

Hoult, D.I., 2000. The principle of reciprocity in signal strength calculations—A mathematical guide. Concepts Magn. Reson. 12, 173–187. https://doi.org/10.1002/1099-0534(2000)12:4<173::AID-CMR1>3.0.CO;2-Q

Ianniello, C., de Zwart, J.A., Duan, Q., Deniz, C.M., Alon, L., Lee, J.-S., Lattanzi, R., Brown, R., 2018. Synthesized tissue-equivalent dielectric phantoms using salt and polyvinylpyrrolidone solutions. Magn. Reson. Med. https://doi.org/10.1002/mrm.27005

Insko, E.K., Bolinger, L., 1993. Mapping of the Radiofrequency Field. J. Magn. Reson. A 103, 82–85. https://doi.org/10.1006/jmra.1993.1133

Jakobsen, I., Kaalhus, O., Lyng, H., Rofstad, E.K., 1995. Detection of necrosis in human tumour xenografts by proton magnetic resonance imaging. Br. J. Cancer 71, 456–461. https://doi.org/10.1038/bjc.1995.93

Joines, W.T., Zhang, Y., Li, C., Jirtle, R.L., 1994. The measured electrical properties of normal and malignant human tissues from 50 to 900 MHz. Med. Phys. 21, 547–550. https://doi.org/10.1118/1.597312

Karellas, A., Vedantham, S., 2008. Breast cancer imaging: A perspective for the next decade. Med. Phys. 35, 4878–4897. https://doi.org/10.1118/1.2986144

Katscher, U., Abe, H., Ivancevic, M., Djamshidi, K., Karkowski, P., Newstead, G., 2013. Towards the investigation of breast tumor malignancy via electric conductivity measurement, in: Proceedings of the 21th Annual Meeting of ISMRM. Salt Lake City, USA, p. 3372.

Katscher, U., Bornert, P., 2016. Imaging of Lung Conductivity Using Ultrashort Echo-Time Imaging, in: Proceedings of the 25th Annual Meeting of ISMRM. Singapore, p. 2923.

Katscher, U., Börnert, P., Leussler, C., van den Brink, J.S., 2003. Transmit SENSE. Magn. Reson. Med. 49, 144–150. https://doi.org/10.1002/mrm.10353

Katscher, U., Djamshidi, K., Voigt, T., Ivancevic, M., Abe, H., Newstead, G., Keupp, J., Philips Research, 2012a. Estimation of Breast Tumor Conductivity using Parabolic Phase Fitting. Presented at the ISMRM, Melbourne, Australia, p. 3482.

Katscher, U., Findeklee, C., Voigt, T., 2012b. B1-based specific energy absorption rate determination for nonquadrature radiofrequency excitation. Magn. Reson. Med. 68, 1911–1918. https://doi.org/10.1002/mrm.24215

Katscher, U., Gagiyev, M., Meineke, J., 2016. Conductivity Determination of Deep Gray Matter Nuclei Utilizing Susceptibility-Based Delineation, in: Proceedings of the 25th Annual Meeting of ISMRM. Singapore, p. 3336.

Katscher, U., van den Berg, C.A.T., 2017. Electric properties tomography: biochemical, physical and technical background, evaluation and clinical applications. NMR Biomed. 30, e3729. https://doi.org/10.1002/nbm.3729

Katscher, U., Voigt, T., Findeklee, C., Vernickel, P., Nehrke, K., Dossel, O., 2009. Determination of electric conductivity and local SAR via B1 mapping. IEEE Trans. Med. Imaging 28, 1365–1374. https://doi.org/10.1109/TMI.2009.2015757

Kim, S.-Y., Shin, J., Kim, D.-H., Kim, M.J., Kim, E.-K., Moon, H.J., Yoon, J.H., 2016. Correlation between conductivity and prognostic factors in invasive breast cancer using magnetic resonance electric properties tomography (MREPT). Eur. Radiol. 26, 2317–2326. https://doi.org/10.1007/s00330-015-4067-7

Knoll, F., Bredies, K., Pock, T., Stollberger, R., 2011. Second order total generalized variation (TGV) for MRI. Magn. Reson. Med. 65, 480–491. https://doi.org/10.1002/mrm.22595

Lazebnik, M., Popovic, D., McCartney, L., Watkins, C.B., Lindstrom, M.J., Harter, J., Sewall, S., Ogilvie, T., Magliocco, A., Breslin, T.M., Temple, W., Mew, D., Booske, J.H., Okoniewski, M., Hagness, S.C., 2007. A large-scale study of the ultrawideband microwave dielectric properties of normal, benign and malignant breast tissues obtained from cancer surgeries. Phys. Med. Biol. 52, 6093. https://doi.org/10.1088/0031-9155/52/20/002

Lee, S.-K., Bulumulla, S., Hancu, I., 2015. Theoretical investigation of random noise-limited signal-to-noise ratio in MR-based electrical properties tomography. IEEE Trans. Med. Imaging 34, 2220–32. https://doi.org/10.1109/TMI.2015.2427236

Liao, Y., Romanzetti, S., Gras, V., Huang, D., Shah, N.J., 2015. The dielectric properties of brain tissues: variation in electrical conductivity with tissue sodium concentration and tissue water content at 3T/4T, in: Proc. Intl. Soc. Mag. Reson. Med. 23. Toronto, Canada, p. 3302.

Liu, J., Moortele, P.F.V. de, Zhang, X., Wang, Y., He, B., 2016. Simultaneous Quantitative Imaging of Electrical Properties and Proton Density From Maps Using MRI. IEEE Trans. Med. Imaging 35, 2064–2073. https://doi.org/10.1109/TMI.2016.2547988

Liu, J., Shao, Q., Wang, Y., Adriany, G., Bischof, J., Van de Moortele, P.-F., He, B., 2017a. In vivo imaging of electrical properties of an animal tumor model with an 8-channel transceiver array at 7 T using electrical properties tomography. Magn. Reson. Med. 78, 2157–2169. https://doi.org/10.1002/mrm.26609

Liu, J., Wang, Y., Katscher, U., He, B., 2017b. Electrical properties tomography based on B1 maps in MRI: principles, applications, and challenges. IEEE Trans. Biomed. Eng. 64, 2515–2530. https://doi.org/10.1109/TBME.2017.2725140

Liu, J., Zhang, X., Moortele, P.-F.V. de, Schmitter, S., He, B., 2013. Determining electrical properties based on B1 fields measured in an MR scanner using a multi-channel transmit/receive coil: a general approach. Phys. Med. Biol. 58, 4395. https://doi.org/10.1088/0031-9155/58/13/4395

Liu, J., Zhang, X., Schmitter, S., Van de Moortele, P.-F., He, B., 2015. Gradient-based electrical properties tomography (gEPT): A robust method for mapping electrical properties of biological tissues in vivo using magnetic resonance imaging. Magn. Reson. Med. 74, 634–646. https://doi.org/10.1002/mrm.25434

Mandija, S., Bruin, P. de, Webb, A., Luijten, P., Berg, C. van den, 2017. Investigating the relation between electrical conduction and tissue composition with proton and sodium MRI, in: Proc. Intl. Soc. Mag. Reson. Med. 25. Honolulu, USA, p. 3639.

Manusama, E.R., Stavast, J., Durante, N.M., Marquet, R.L., Eggermont, A.M., 1996. Isolated limb perfusion with TNF alpha and melphalan in a rat osteosarcoma model: a new anti-tumour approach. Eur. J. Surg. Oncol. 22, 152–157.

Marques, J.P., Sodickson, D.K., Ipek, O., Collins, C.M., Gruetter, R., 2014. Single acquisition electrical property mapping based on relative coil sensitivities: A proof-of-concept demonstration. Magn. Reson. Med. 74, 185–195. https://doi.org/10.1002/mrm.25399

Meacham, C.E., Morrison, S.J., 2013. Tumour heterogeneity and cancer cell plasticity. Nature 501, 328–337. https://doi.org/10.1038/nature12624

Metherall, P., Barber, D.C., Smallwood, R.H., Brown, B.H., 1996. Three-dimensional electrical impedance tomography. Nature 380, 509–512. https://doi.org/10.1038/380509a0

Metzger, G.J., Snyder, C., Akgun, C., Vaughan, T., Ugurbil, K., Van de Moortele, P.-F., 2008. Local B1+ shimming for prostate imaging with transceiver arrays at 7T based on subject-dependent transmit phase measurements. Magn. Reson. Med. 59, 396–409. https://doi.org/10.1002/mrm.21476

Narhi, L.O., Philo, J.S., Li, T., Zhang, M., Samal, B., Arakawa, T., 1996. Induction of alpha-helix in the beta-sheet protein tumor necrosis factor-alpha: acid-induced denaturation. Biochemistry (Mosc.) 35, 11454–11460. https://doi.org/10.1021/bi952767n

Nehrke, K., Börnert, P., 2012. DREAM—a novel approach for robust, ultrafast, multislice B1 mapping. Magn. Reson. Med. 68, 1517–1526. https://doi.org/10.1002/mrm.24158

O'Connor, J.P.B., Aboagye, E.O., Adams, J.E., Aerts, H.J.W.L., Barrington, S.F., Beer, A.J., Boellaard, R., Bohndiek, S.E., Brady, M., Brown, G., Buckley, D.L., Chenevert, T.L., Clarke, L.P., Collette, S., Cook, G.J., deSouza, N.M., Dickson, J.C., Dive, C., Evelhoch, J.L., Faivre-Finn, C., Gallagher, F.A., Gilbert, F.J., Gillies, R.J., Goh, V., Griffiths, J.R., Groves, A.M., Halligan, S., Harris, A.L., Hawkes, D.J., Hoekstra, O.S., Huang, E.P., Hutton, B.F., Jackson, E.F., Jayson, G.C., Jones, A., Koh, D.-M., Lacombe, D., Lambin, P., Lassau, N., Leach, M.O., Lee, T.-Y., Leen, E.L., Lewis, J.S., Liu, Y., Lythgoe, M.F., Manoharan, P., Maxwell, R.J., Miles, K.A., Morgan, B., Morris, S., Ng, T., Padhani, A.R., Parker, G.J.M., Partridge, M., Pathak, A.P., Peet, A.C., Punwani, S., Reynolds, A.R., Robinson, S.P., Shankar, L.K., Sharma, R.A., Soloviev, D., Stroobants, S., Sullivan, D.C., Taylor, S.A., Tofts, P.S., Tozer, G.M., van Herk, M., Walker-Samuel, S., Wason, J., Williams, K.J., Workman, P., Yankeelov, T.E., Brindle, K.M., McShane, L.M., Jackson, A., Waterton, J.C., 2017. Imaging biomarker roadmap for cancer studies. Nat. Rev. Clin. Oncol. 14, 169–186. https://doi.org/10.1038/nrclinonc.2016.162

O'Connor, J.P.B., Rose, C.J., Waterton, J.C., Carano, R.A.D., Parker, G.J.M., Jackson, A., 2015. Imaging intratumor heterogeneity: role in therapy response, resistance, and clinical

outcome. Clin. Cancer Res. 21, 249–257. https://doi.org/10.1158/1078-0432.CCR-14-0990

Padormo, F., Hess, A.T., Aljabar, P., Malik, S.J., Jezzard, P., Robson, M.D., Hajnal, J.V., Koopmans, P.J., 2016. Large dynamic range relative B1+ mapping. Magn. Reson. Med. 76, 490–499. https://doi.org/10.1002/mrm.25884

Perlmutter, J.S., Mink, J.W., 2006. Deep Brain Stimulation. Annu. Rev. Neurosci. 29, 229–257. https://doi.org/10.1146/annurev.neuro.29.051605.112824

Peyman, A., Gabriel, C., Grant, E.H., Vermeeren, G., Martens, L., 2009. Variation of the dielectric properties of tissues with age: the effect on the values of SAR in children when exposed to walkie–talkie devices. Phys. Med. Biol. 54, 227. https://doi.org/10.1088/0031-9155/54/2/004

Peyman, A., Holden, S.J., Watts, S., Perrott, R., Gabriel, C., 2007. Dielectric properties of porcine cerebrospinal tissues at microwave frequencies: in vivo , in vitro and systematic variation with age. Phys. Med. Biol. 52, 2229. https://doi.org/10.1088/0031-9155/52/8/013

Peyman, A., Rezazadeh, A.A., Gabriel, C., 2001. Changes in the dielectric properties of rat tissue as a function of age at microwave frequencies. Phys. Med. Biol. 46, 1617–1629. https://doi.org/10.1088/0031-9155/46/6/303

Proskuryakov, S.Y., Gabai, V.L., 2010. Mechanisms of tumor cell necrosis. Curr. Pharm. Des. 16, 56–68.

Pruessmann, K.P., Weiger, M., Scheidegger, M.B., Boesiger, P., 1999. SENSE: Sensitivity encoding for fast MRI. Magn. Reson. Med. 42, 952–962. https://doi.org/10.1002/(SICI)1522-2594(199911)42:5<952::AID-MRM16>3.0.CO;2-S

Ropella, K.M., Noll, D.C., 2016. A regularized, model-based approach to phase-based conductivity mapping using MRI. Magn. Reson. Med. 78, 2011–2021. https://doi.org/10.1002/mrm.26590

Sacolick, L.I., Sun, L., Vogel, M.W., Dixon, W.T., Hancu, I., 2011. Fast radiofrequency flip angle calibration by Bloch–Siegert shift. Magn. Reson. Med. 66, 1333–1338. https://doi.org/10.1002/mrm.22902

Sacolick, L.I., Wiesinger, F., Hancu, I., Vogel, M.W., 2010. B1 mapping by Bloch-Siegert shift. Magn. Reson. Med. 63, 1315–1322. https://doi.org/10.1002/mrm.22357

Schmidt, R., Webb, A., 2016. A new approach for electrical properties estimation using a global integral equation and improvements using high permittivity materials. J. Magn. Reson. 262, 8–14. https://doi.org/10.1016/j.jmr.2015.11.002

Schwan, H.P., Foster, K.R., 1980. RF-field interactions with biological systems: electrical properties and biophysical mechanisms. Proc. IEEE 68, 104–113. https://doi.org/10.1109/PROC.1980.11589

Semenov, S., Huynh, T., Williams, T., Nicholson, B., Vasilenko, A., 2017. Dielectric properties of brain tissue at 1 GHz in acute ischemic stroke: Experimental study on swine. Bioelectromagnetics 38, 158–163. https://doi.org/10.1002/bem.22024

Serralles, J., Polimeridis, A., Vaidya, M., Haemer, G., White, J., Sodickson, D., Daniel, L., Lattanzi, R., 2016. Global Maxwell Tomography: a novel technique for electrical properties mapping without symmetry assumptions or edge artifacts, in: Proc. Intl. Soc. Mag. Reson. Med. 24. Singapore, p. 2993.

Sha, L., Ward, E.R., Stroy, B., 2002. A review of dielectric properties of normal and malignant breast tissue, in: Proceedings IEEE SoutheastCon, 2002. Presented at the Proceedings IEEE SoutheastCon, 2002, pp. 457–462. https://doi.org/10.1109/.2002.995639

Sherblom, A.P., Buck, R.L., Carraway, K.L., 1980. Purification of the major sialoglycoproteins of 13762 MAT-B1 and MAT-C1 rat ascites mammary adenocarcinoma cells by density gradient centrifugation in cesium chloride and guanidine hydrochloride. J. Biol. Chem. 255, 783–790.

Shin, J., Kim, M.J., Lee, J., Nam, Y., Kim, M., Choi, N., Kim, S., Kim, D.-H., 2015. Initial study on in vivo conductivity mapping of breast cancer using MRI. J. Magn. Reson. Imaging 42, 371–378. https://doi.org/10.1002/jmri.24803

Sodickson, D., Alon, L., Deniz, C., Ben-Eliezer, N., Cloos, M., Sodickson, L., Collins, C., Wiggins, G., Novikov, D., 2013. Generalized Local Maxwell Tomography for Mapping of Electrical Property Gradients and Tensors, in: Proc. Intl. Soc. Mag. Reson. Med. 21. Salt Lake City, USA, p. 3372.

Sodickson, D., Alon, L., Deniz, C., Brown, R., Zhang, B., Wiggins, G., Cho, G., Eliezer, N., Novikov, D., Lattanzi, R., others, 2012. Local Maxwell tomography using transmit-receive coil arrays for contact-free mapping of tissue electrical properties and determination of absolute RF phase. Proc Intl Soc Mag Reson Med 20 Melb. Aust. 2012 P 0387.

Stehning, C., Voigt, T., Karkowski, P., Katscher, U., Philips Research, 2012. Electric Properties Tomography (EPT) of the Liver in a Single Breathhold Using SSFP, in: Proceedings of the 20th Annual Meeting of ISMRM. Presented at the ISMRM, Melbourne, Australia, p. 386.

Sutherland, R.M., Rasey, J.S., Hill., R.P., 1988. Tumor biology. Am. J. Clin. Oncol. 11, 253–274.

Swanton, C., 2012. Intratumor heterogeneity: evolution through space and time. Cancer Res. 72, 4875–4882. https://doi.org/10.1158/0008-5472.CAN-12-2217

Swarup, A., Stuchly, S.S., Surowiec, A., 1991. Dielectric properties of mouse MCA1 fibrosarcoma at different stages of development. Bioelectromagnetics 12, 1–8. https://doi.org/10.1002/bem.2250120102

Tamarkin, L., Myer, L., Haynes, R., Paciotti, G., 2006. CYT-6091 (Aurimune): a colloidal gold-based tumor-targeted nanomedicine. Nanomedicine Nanotechnol. Biol. Med. 2, 273–274. https://doi.org/10.1016/j.nano.2006.10.020

Tha, K.K., Katscher, U., Stehning, C., Yamaguchi, S., Terasaka, S., Sugimori, H., Yamamoto, T., Fujima, N., Kudo, Y., van Cauteren, M., Shirato, H., 2015. Electrical Conductivity Characteristics of Meningiomas: Noninvasive Assessment using Electric Properties Tomography, in: Proceedings of the 23rd Annual Meeting of ISMRM. Toronto, ON, Canada, p. 4397.

Tha, K.K., Katscher, U., Yamaguchi, S., Stehning, C., Terasaka, S., Fujima, N., Kudo, K., Kazumata, K., Yamamoto, T., Cauteren, M.V., Shirato, H., 2018. Noninvasive electrical conductivity measurement by MRI: a test of its validity and the electrical conductivity characteristics of glioma. Eur. Radiol. 28, 348–355. https://doi.org/10.1007/s00330-017-4942-5

Tha, K.K., Stehning, C., suzuki, Y., Katscher, U., Keupp, J., Kazumata, K., Terasaka, S., van Cauteren, M., Kudo, K., Shirato, H., 2014. Noninvasive Evaluation of Electrical Conductivity of the Normal Brain and Brain Tumors, in: Proceedings of the 22nd Annual Meeting of ISMRM. Milan, Italy, p. 1885.

Vakkila, J., Lotze, M.T., 2004. Inflammation and necrosis promote tumour growth. Nat. Rev. Immunol. 4, 641–648. https://doi.org/10.1038/nri1415

Van de Moortele, P.-F., Akgun, C., Adriany, G., Moeller, S., Ritter, J., Collins, C.M., Smith, M.B., Vaughan, J.T., Uğurbil, K., 2005. B1 destructive interferences and spatial phase patterns at 7 T with a head transceiver array coil. Magn. Reson. Med. 54, 1503–1518. https://doi.org/10.1002/mrm.20708

Van de Moortele, P.-F., Auerbach, E.J., Olman, C., Yacoub, E., Uğurbil, K., Moeller, S., 2009. T1 weighted brain images at 7 Tesla unbiased for Proton Density, T2* contrast and RF coil receive B1 sensitivity with simultaneous vessel visualization. NeuroImage 46, 432–446. https://doi.org/10.1016/j.neuroimage.2009.02.009

Van de Moortele, P.F., Snyder, C., DelaBarre, L., Adriany, G., Vaughan, J.T., Ugurbil, K., 2007. Calibration Tools for RF Shim at Very High Field with Multiple Element RF Coils: from Ultra Fast Local Relative Phase to Absolute Magnitude B1+ Mapping, in: Proc. Intl. Soc. Mag. Reson. Med. 15. Berlin, Germany, p. 1676.

Van Lier, A.L.H.M.W., Brunner, D.O., Pruessmann, K.P., Klomp, D.W.J., Luijten, P.R., Lagendijk, J.J.W., van den Berg, C.A.T., 2012. B 1+ Phase mapping at 7 T and its application for in vivo electrical conductivity mapping. Magn. Reson. Med. 67, 552–561. https://doi.org/10.1002/mrm.22995

Van Lier, A.L.H.M.W., Raaijmakers, A., Voigt, T., Lagendijk, J.J.W., Luijten, P.R., Katscher, U., van den Berg, C.A.T., 2014. Electrical Properties Tomography in the Human Brain at 1.5, 3, and 7T: A Comparison Study. Magn. Reson. Med. 71, 354–363. https://doi.org/10.1002/mrm.24637

Van Lier, A.L.H.M.W., van der Kolk, A.G., Brundel, M., Hendrikse, J., Luijten, P.R., Lagendijk, J.J.W., van den Berg, C.A.T., 2012. Electrical conductivity in ischemic stroke at 7.0 Tesla: A Case Study, in: Proceedings of the 20th Annual Meeting of ISMRM. Presented at the ISMRM, Melbourne, Australia, p. 3484.

Vaughan, J., Garwood, M., Collins, C., Liu, W., DelaBarre, L., Adriany, G., Andersen, P., Merkle, H., Goebel, R., Smith, M. b., Ugurbil, K., 2001. 7T vs. 4T: RF power, homogeneity, and signal-to-noise comparison in head images. Magn. Reson. Med. 46, 24–30. https://doi.org/10.1002/mrm.1156

Voigt, T., Homann, H., Katscher, U., Doessel, O., 2012a. Patient-individual local SAR determination: In vivo measurements and numerical validation. Magn. Reson. Med. 68, 1117–1126. https://doi.org/10.1002/mrm.23322

Voigt, T., Katscher, U., Doessel, O., 2011. Quantitative conductivity and permittivity imaging of the human brain using electric properties tomography. Magn. Reson. Med. 66, 456–466. https://doi.org/10.1002/mrm.22832

Voigt, T., Schuster, A., Ishida, M., Stehning, C., Katscher, U., Chiribiri, A., Nagel, E., Schaeffter, T., 2012b. Conductivity Imaging of an Ischemic Pig Heart Model Using Electric Properties Tomography, in: Proceedings of the 20th Annual Meeting of ISMRM. Melbourne, Australia, p. 3483.

Wang, Y., Van de Moortele, P.-F., He, B., 2018. Automated Seed Selection for Gradient-based Electrical Properties Tomography and Its in vivo Validation in the Brain, in: Proc. Intl. Soc. Mag. Reson. Med. 26. Paris, France, p. 6670.

Wang, Y., Van de Moortele, P.-F., He, B., 2017. CONtrast Conformed Electrical Properties Tomography (CONCEPT) Based on Multi-Channel Transmission, in: Proc. Intl. Soc. Mag. Reson. Med. 25. Honolulu, USA, p. 3640.

Weinberg, R., 2013. The Biology of Cancer, Second Edition. Garland Science, New York.

Weingärtner, S., Zimmer, F., Metzger, G.J., Uğurbil, K., Van de Moortele, P.-F., Akçakaya, M., 2016. Motion-robust cardiac B1+ mapping at 3T using interleaved bloch-siegert shifts. Magn. Reson. Med. n/a-n/a. https://doi.org/10.1002/mrm.26395

Wen, H., 2003. Noninvasive quantitative mapping of conductivity and dielectric distributions using RF wave propagation effects in high-field MRI, in: Proc. SPIE. San Diego, USA, pp. 471–477. https://doi.org/10.1117/12.480000

Woo, E.J., Seo, J.K., 2008. Magnetic resonance electrical impedance tomography (MREIT) for high-resolution conductivity imaging. Physiol. Meas. 29, R1. https://doi.org/10.1088/0967-3334/29/10/R01

Xu, Y., He, B., 2005. Magnetoacoustic tomography with magnetic induction (MAT-MI). Phys. Med. Biol. 50, 5175. https://doi.org/10.1088/0031-9155/50/21/015

Yang, Q.X., Mao, W., Wang, J., Smith, M.B., Lei, H., Zhang, X., Ugurbil, K., Chen, W., 2006. Manipulation of image intensity distribution at 7.0 T: passive RF shimming and focusing with dielectric materials. J. Magn. Reson. Imaging 24, 197–202. https://doi.org/10.1002/jmri.20603

Yarnykh, V.L., 2007. Actual flip-angle imaging in the pulsed steady state: a method for rapid three-dimensional mapping of the transmitted radiofrequency field. Magn. Reson. Med. 57, 192–200. https://doi.org/10.1002/mrm.21120

Zhang, X., Liu, J., He, B., 2014a. Magnetic-resonance-based electrical properties tomography: a review. Biomed. Eng. IEEE Rev. In 7, 87–96. https://doi.org/10.1109/RBME.2013.2297206

Zhang, X., Moortele, P.-F.V. de, Schmitter, S., He, B., 2013a. Complex B1 mapping and electrical properties imaging of the human brain using a 16-channel transceiver coil at 7T. Magn. Reson. Med. 69, 1285–1296. https://doi.org/10.1002/mrm.24358

Zhang, X., Schmitter, S., Van de Moortele, P., Liu, J., He, B., 2013b. From complex mapping to local SAR estimation for human brain MR imaging using multi-channel transceiver coil at 7T. IEEE Trans. Med. Imaging 32, 1058–1067. https://doi.org/10.1109/TMI.2013.2251653

Zhang, X., Van de Moortele, P.-F., Liu, J., Schmitter, S., He, B., 2014b. Quantitative prediction of radio frequency induced local heating derived from measured magnetic field maps in magnetic resonance imaging: A phantom validation at 7 T. Appl. Phys. Lett. 105, 244101. https://doi.org/10.1063/1.4903774

Zhang, X., Zhu, S., He, B., 2010. Imaging electric properties of biological tissues by RF field mapping in MRI. IEEE Trans. Med. Imaging 29, 474–481. https://doi.org/10.1109/TMI.2009.2036843

Zhao, B., Lu, W., Hitchens, T.K., Lam, F., Ho, C., Liang, Z.-P., 2015. Accelerated MR parameter mapping with low-rank and sparsity constraints. Magn. Reson. Med. 74, 489–498. https://doi.org/10.1002/mrm.25421